

# **Material and structural modelling of corrugated paperboard packaging**

by  
Megan Marya Starke

*Thesis presented in partial fulfilment of the requirements for the degree  
of Master of Engineering (Mechanical) in the Faculty of Engineering at  
Stellenbosch University*



Supervisor: Prof. Corné Coetzee  
Co-supervisor: Prof. Umezuruike Linus Opara

March 2020

# Declaration

By submitting this thesis electronically, I declare that the entirety of the work contained therein is my own, original work, that I am the sole author thereof (save to the extent explicitly otherwise stated), that reproduction and publication thereof by Stellenbosch University will not infringe any third party rights and that I have not previously in its entirety or in part submitted it for obtaining any qualification.

Date: ..... March 2020 .....

Copyright © 2020 Stellenbosch University  
All rights reserved.

# Abstract

## **Material and structural modelling of corrugated paperboard packaging**

M.M. Starke

*Department of Mechanical and Mechatronic Engineering,  
University of Stellenbosch,  
Private Bag XI, Matieland 7602, South Africa.*

Thesis: MEng (Mech)

March 2020

Corrugated paperboard is the primary packaging material for fresh horticultural produce and plays an integral part in protecting the produce from mechanical damage throughout the cold chain journey. Bruising is the most common form of mechanical damage to fresh produce and is responsible for increased food waste and the associated financial losses. Due to the difficulties in predicting the strength of corrugated paperboard packaging, cartons are often over-designed to withstand the high relative humidity (RH) conditions and large stacking loads during cold storage, and the impact and vibrational loads during transport operations. This thesis further investigates the finite element method (FEM) as a design tool for corrugated paperboard packaging. A simplified material model of the corrugated sandwich structure, in which the corrugated core was reduced to an equivalent homogeneous core, was developed and validated. The material model is based on experimentally obtained material properties for the corrugated board constituents. An experimental study was conducted to investigate the mechanical behaviour of the Mk 4 carton during box compression testing. The Mk 4 carton is one of the primary packaging designs for exporting pome fruit in South Africa. Three different FEM boundary conditions were replicated to investigate their effects on the load-displacement response of the carton. Digital image correlation (DIC) was used to measure the out-of-plane displacement field, and a Tekscan pressure mapping sensor was used to characterize the load distribution between the base of the carton and the platen of the compression tester. A nonlinear finite element (FE) model of the Mk 4 telescopic carton was developed (using the simplified material model) and validated with experimental results. Eight-node solid-shell elements were used in the model, and the touch-

ing contact between the inner- and the outer carton was considered in the analyses. The model predicts a collapse load within 3% of the measured value, and there is good agreement between the buckled shape of the model and that of the physical cartons. The model predicts a maximum out-of-plane displacement within 35% of the measured value from the DIC results. The FE model can be used as a design tool if the objective is to design based on compression strength and material requirements. Further work is required to improve the model's load-deformation response.

# Uittreksel

## **Materiaal en strukturele modellering van geriffelde kartonverpakking**

*("Material and structural modelling of corrugated paperboard packaging")*

M.M. Starke

*Departement Meganiese en Megatroniese Ingenieurswese,  
Universiteit van Stellenbosch,  
Privaatsak XI, Matieland 7602, Suid Afrika.*

Tesis: MIng (Meg)

Maart 2020

Geriffelde karton is die primêre verpakkingsmateriaal vir vars groente en vrugte en is belangrik vir die beskerming van die produkte teen meganiese skade gedurende die kouekettingreis. Meganiese skade is die mees algemene oorsaak van kneusing in vars groente en vrugte, en is verantwoordelik vir verhoogde voedsel vermorsing en die geassosieerde finansiële verliese. Kartonne word dikwels ontwerp om die hoë humiditeit kondisies, groot stapelbelasting tydens koud opberging, en die impak- en vibrasie laste tydens vervoer te weerstaan. Hierdie tesis ondersoek die eindige elementmetode as 'n ontwerpinstrument vir geriffelde kartonverpakking. 'n Vereenvoudigde materiaalmodel van die gelamineerde geriffelde struktuur, waarin die geriffelde kern vereenvoudig word as 'n ekwivalente homogene kern, was ontwikkel en gevalideer. Die materiaal model is gebaseer op eksperimenteel verkreë materiaal-eienskappe vir die golfkartonbestanddele. 'n Eksperimentele studie was uitgevoer om die meganiese gedrag van die Mk 4-karton onder drukbelasting te karakteriseer. Die Mk 4-karton is een van die vernaaamste verpakkingsontwerpe vir die uitvoer van kernvrugte in Suid-Afrika. Die effek van drie verskillende grensvoorwaardes op die las-verplasings gedrag van die karton is ondersoek. Digitale beeldkorrelasie is gebruik om die verplasingsveld te meet, en 'n "Tekscan"-druksensor is gebruik om die lasverspreiding tussen die basis van die karton en die onderste plaat van die karton-druktoets te karakteriseer. 'n Nie-lineêre eindige element model van die Mk 4 teleskopiese karton-ontwerp is ontwikkel en gevalideer met eksperimentele resultate. Agt-knooppunt soliede-dopelemente is in die model gebruik, en die kontak tussen

die binne- en buitenste bokse is in ag geneem in die analise. Die model voor-  
spel 'n ineenstortingslas binne 3% van die gemete waarde, en daar is 'n goeie  
ooreenkoms tussen die gedeformeerde vorm van die model en dié van die fisiese  
kartonne. Die model se maksimum buite-vlaks verplasing is binne 35% van die  
gemete waarde. Die model kan as 'n ontwerpinstrument gebruik word indien  
die ontwerp gebaseer is op die ineenstortingslas en materiaal vereistes. Verdere  
navorsing is nodig om die las-verplasings gedrag van die model te verbeter.

# Acknowledgements

I would like to thank the following people for their contribution to the completion of this project:

Calvin, Magda, Fanie and Lizzie for their love and support, always

Paul and Elize for their unending love and prayers over the years

Professor Corné Coetzee for his knowledge and guidance and for always being available to share ideas

Dr Tobi Fadiji for his time and advice during the last few years

Professor Umezuruike Linus Opara for his guidance and support

Mr Gerrit Visser from SIMTEQ for his valuable FEM advice

Mr Dewald Grobbelaar from APL Cartons, who provided the experimental samples

Mr Kiril Dimitrov and Mr Bongani Xaba from Mpact for facilitating the materials testing

This work is based on the research supported wholly by the National Research Foundation of South Africa (Grant Numbers: 64813). The opinions, findings and conclusions or recommendations expressed are those of the author(s) alone, and the NRF accepts no liability whatsoever in this regard.

# Contents

<b>Declaration</b>	<b>i</b>
<b>Abstract</b>	<b>ii</b>
<b>Uittreksel</b>	<b>iv</b>
<b>Acknowledgements</b>	<b>vi</b>
<b>Contents</b>	<b>vii</b>
<b>List of Figures</b>	<b>ix</b>
<b>List of Tables</b>	<b>xii</b>
<b>1 Introduction</b>	<b>1</b>
1.1 Project background . . . . .	1
1.2 Research objectives . . . . .	2
1.3 Motivation . . . . .	3
<b>2 Literature study</b>	<b>4</b>
2.1 Corrugated paperboard . . . . .	4
2.2 Performance testing of paper, board and packaging . . . . .	10
2.3 The finite element method . . . . .	13
<b>3 Materials testing and modelling</b>	<b>22</b>
3.1 Required material properties . . . . .	22
3.2 Materials testing and results . . . . .	24
3.3 Homogenisation of the corrugated core . . . . .	30
3.4 Finite element modelling . . . . .	33
3.5 Summary . . . . .	43
<b>4 Box compression test experimental study</b>	<b>44</b>
4.1 Friction coefficients . . . . .	44
4.2 Boundary conditions experiment . . . . .	47
4.3 Tekscan pressure mapping . . . . .	52



<i>CONTENTS</i>	<b>viii</b>
4.4 3D digital image correlation . . . . .	54
<b>5 Structural modelling</b>	<b>58</b>
5.1 Mk 4 inner . . . . .	58
5.2 Mk 4 telescopic . . . . .	69
5.3 Summary . . . . .	79
<b>6 Concluding remarks and recommendations</b>	<b>80</b>
<b>Appendices</b>	<b>82</b>
<b>A MATLAB script: Corrugated core homogenisation</b>	<b>83</b>
<b>B Experiments: Additional information and results</b>	<b>86</b>
<b>C Mk 4 carton flat pattern</b>	<b>91</b>
<b>References</b>	<b>93</b>

# List of Figures

1.1	Mk 4 telescopic carton (Fadiji, 2015) . . . . .	3
2.1	Corrugated paperboard geometry and reference directions (Nordstrand, 2004) . . . . .	5
2.2	Typical corrugated paperboard configurations (Twede and Selke, 2005)	5
2.3	Corrugation process of single-wall board (Emblem and Emblem, 2012)	7
2.4	Stress-strain response of paper under uniaxial tension (adapted from Phongphinitana and Jearanaisilawong (2012)) . . . . .	8
2.5	Stress-strain response of paper in the MD, CD and 45° to the MD (adapted from Phongphinitana and Jearanaisilawong (2012)) . . . . .	8
2.6	Creep behaviour of a viscoelastic material (Arvidsson and Grönvall, 2004) . . . . .	9
2.7	Accelerated creep of paper under cyclic humidity (Haslach, 1994) . . .	10
2.8	Transition of the corrugated core to an equivalent homogeneous core (Nordstrand, 1995) . . . . .	16
2.9	Static condensation of a corrugated paperboard panel (Biancolini, 2005)	18
2.10	A paperboard package divided into three segments (Beldie <i>et al.</i> , 2001)	19
3.1	Tensile specimen speckle pattern and subset size . . . . .	26
3.2	DIC displacement and strain fields of a 250KL tensile specimen . . . .	27
3.3	Poisson's ratio vs. axial strain of a 250KL specimen . . . . .	28
3.4	Corrugated core profile . . . . .	30
3.5	Geometry of the C-flute corrugated board (in mm) . . . . .	34
3.6	Symmetry conditions for the ECT model . . . . .	35
3.7	First buckling mode of the detailed ECT model . . . . .	37
3.8	Symmetry conditions for the model of a 400 mm × 400 mm corrugated paperboard panel . . . . .	37
3.9	First buckling mode of the 400 mm × 400 mm detailed model and out-of-plane displacement response at 1395 N . . . . .	38
3.10	Composite laminate profile for the simplified material model . . . . .	39
3.11	First buckling mode of the simplified shell model and out-of-plane displacement response at 1346 N . . . . .	40
3.12	First buckling mode of the simplified solid-shell model and out-of-plane displacement response at 1426 N . . . . .	40

3.13	Global out-of-plane displacement at the collapse load of the geometrically imperfect thick-shell model . . . . .	41
3.14	Global out-of-plane displacement at the collapse load of the geometrically imperfect solid-shell model . . . . .	42
3.15	In-plane shear strain at the collapse load of (a) the quarter-symmetry detailed model, (b) the geometrically imperfect thick-shell model, and (c) the geometrically imperfect solid-shell model . . . . .	42
4.1	Friction coefficient experimental setup . . . . .	45
4.2	Shear force vs. time for a B-flute sample (MD textured side) at the 15 kg weight increment . . . . .	46
4.3	Linear curve fit applied to shear force vs. normal force data . . . . .	47
4.4	Clamping fixture for the BCT boundary condition experiments . . . . .	48
4.5	BCT results for ten Mk 4 cartons . . . . .	49
4.6	BCT load-displacement response of the Mk 4 inner, outer, assembly and glued assembly . . . . .	50
4.7	BCT load-displacement response of the Mk 4 telescopic carton and three boundary condition test cases . . . . .	51
4.8	Delamination damage of the Mk 4 telescopic carton observed in boundary condition test case (3) . . . . .	51
4.9	BCT load-displacement response of the Mk 4 inner and two boundary condition test cases . . . . .	52
4.10	BCT pressure distribution across half the base of the Mk 4 telescopic carton . . . . .	54
4.11	DIC horizontal displacement field of the Mk 4 front panel . . . . .	56
4.12	DIC vertical displacement field of the Mk 4 front panel . . . . .	56
4.13	DIC out-of-plane displacement field of the Mk 4 front panel . . . . .	57
5.1	Full MK 4 inner and modelled section . . . . .	59
5.2	FE model of the Mk 4 inner with quarter-symmetry conditions . . . . .	60
5.3	Mesh convergence study for the thick-shell Mk 4 inner . . . . .	61
5.4	Mesh convergence study for the solid-shell Mk 4 inner . . . . .	62
5.5	First buckling mode shape of the Mk 4 inner (a) thick-shell model and (b) solid-shell model . . . . .	63
5.6	Load-displacement response of the Mk 4 inner thick-shell model . . . . .	64
5.7	Load-displacement response of the Mk 4 inner solid-shell model . . . . .	64
5.8	X- and Z-displacement plots (top and bottom) of the thick-shell model (Mk 4 inner) for a simulated BCT . . . . .	66
5.9	X- and Z-displacement plots (top and bottom) of the solid-shell model (Mk 4 inner) for a simulated BCT . . . . .	67
5.10	Tsai-Wu failure index propagation (left to right) of the outer liner (Mk 4 inner thick-shell model) during the simulated BCT . . . . .	68
5.11	Shear strain distribution of the Mk 4 inner (thick-shell model) during the simulated BCT . . . . .	68

5.12	Crease lines in the corners of the Mk 4 inner after compression . . . . .	68
5.13	FE model of the Mk 4 telescopic carton with quarter-symmetry conditions . . . . .	71
5.14	Mesh convergence study for the Mk 4 telescopic carton FE model . . . . .	71
5.15	First buckling mode shape of the Mk 4 telescopic carton FE model . . . . .	72
5.16	Mk 4 telescopic FE model load-displacement response . . . . .	73
5.17	X-displacement plots of the telescopic FE model components (outer and inner) at the collapse load of a simulated BCT . . . . .	74
5.18	Z-displacement plots of the telescopic FE model components (outer and inner) at the collapse load of a simulated BCT . . . . .	75
5.19	Tsai-Wu failure index propagation (left to right) of the outer liner (Mk 4 telescopic model, outer carton) during the simulated BCT . . . . .	76
5.20	Evolution of the highest shear strain regions (left to right) during the simulated BCT of the Mk 4 telescopic model . . . . .	76
5.21	Touching contact (red on the colour map) between the base of the carton and the bottom platen just after the start of the BCT simulation (left) and at the collapse load (right) . . . . .	77
5.22	Touching contact (red on the colour map) between the inner and outer of the Mk 4 telescopic carton at the collapse load of the BCT simulation . . . . .	78
B.1	BCT setup . . . . .	87
B.2	DIC X, Y and Z (top to bottom) displacement fields of the Mk 4 telescopic carton . . . . .	88
B.3	DIC X, Y and Z (top to bottom) displacement fields of the Mk 4 inner . . . . .	89
B.4	Tensile test and DIC setup . . . . .	90
C.1	Flat pattern of the Mk 4 outer carton . . . . .	92

# List of Tables

2.1	Standard flute profiles (Nordstrand, 2003) . . . . .	6
3.1	DIC displacement errors of the paper tensile specimen . . . . .	26
3.2	Summary of the measured elastic properties and standard deviations	29
3.3	Material properties of the linerboard and fluting medium . . . . .	33
3.4	Equivalent elastic properties of the B-flute and C-flute cores . . . . .	34
4.1	Measured static and dynamic friction coefficients . . . . .	46
4.2	DIC displacement errors of the two subset sizes considered for the Mk 4 carton . . . . .	55
5.1	Buckling results of the Mk 4 inner FE models . . . . .	63
5.2	Collapse load of the Mk 4 telescopic FE model for two boundary con- dition cases . . . . .	79
B.1	BCT boundary condition experiment results . . . . .	86

# Chapter 1

## Introduction

### 1.1 Project background

The agricultural industry represents more than 2% of the South African GDP, with over 287 million cartons of horticultural produce exported in the 2018/19 financial year (PPECB, 2018, 2019). Oelofse and Nahman (2013), however, estimated that food waste in South Africa amounts to more than 30% of the average annual agricultural production. The authors further reported that more than 95% of annual food waste is generated in pre-consumer stages, where post-harvest handling and storage is responsible for 26%. A worldwide study by the Food and Agriculture Organisation of the United Nations (FAO) reports that 13.8% of the global food production in 2016 was lost post-harvest and up to the retail stage (FAO, 2019). The study also shows a correlation between global food loss and the world GDP. The growing global population and the decrease in arable land due to erosion, desertification and unsustainable use highlights an urgent need to reduce post-harvest losses as a method to improve food and nutritional security (Opara and Mditshwa, 2013; WWF, 2017; FAO, 2019).

Factors that contribute to food waste during post-harvest handling include inadequate cooling and ventilation management and mechanical damage to fresh produce (Pathare and Opara, 2014; Berry, 2017). Bruising is the most common form of mechanical damage to fruit and vegetables and often occurs as a result of large stacking loads during storage and impact loads during transport and distribution operations (Opara and Pathare, 2014). Bruise damage accelerates decay, reduces consumer satisfaction, and increases food waste and financial losses (Opara and Pathare, 2014).

Packaging plays an integral role in protecting fresh produce from mechanical damage across the cold chain journey (Pathare and Opara, 2014). Corrugated paperboard has become the primary packaging material for the post-harvest handling of horticultural produce (Opara and Mditshwa, 2013). It is affordable, available in abundance, strong in comparison to its mass and entirely recyclable (Gilchrist *et al.*, 1999; Nordstrand, 2003). High moisture conditions are detrimental to the

stiffness and strength of paperboard (Haslach, 1994). Packaging for fresh produce should, therefore, be designed to facilitate efficient airflow and cooling while maintaining its structural integrity at the high relative humidity (RH) conditions during cold storage and refrigerated transport (Pathare and Opara, 2014; Berry, 2017).

Several studies have been published on the structural design of corrugated paperboard packaging (Beldie *et al.*, 2001; Biancolini *et al.*, 2010; Zhang *et al.*, 2011; Fadji *et al.*, 2016; Berry *et al.*, 2017). Many of these studies used the finite element method (FEM) as a design tool. Corrugated paperboard is challenging to model since its material behaviour is a function of the quality of the raw materials (cellulose fibres), the mechanical properties of the paper sheets, and the combined properties of the corrugated board (Gilchrist *et al.*, 1999). Additionally, the material is geometrically complex, inherently nonlinear, and sensitive to moisture (Urbanik, 1997; Gilchrist *et al.*, 1999). Due to the complex material behaviour of corrugated paperboard and the difficulties in modelling structures made thereof, there is scope in the research field to improve current modelling techniques for fresh produce packaging.

## 1.2 Research objectives

The aim of this thesis was to develop and validate a finite element (FE) model of the Mark 4 telescopic carton that can be used as a design tool to improve future packaging performance in terms of strength and material requirements. The Mk 4 carton in Figure 1.1 is one of the primary packaging designs for exporting pome fruit in South Africa and plays an essential role in preserving the quality of the fruit during the cold chain journey. The specific objectives of this thesis are listed and explained below:

1. Materials testing and modelling: Determine and validate the material properties that are required for the structural FE model of the Mk 4 telescopic carton.
2. Mechanical testing of corrugated paperboard cartons: Characterize the mechanical response of the Mk 4 carton during box compression testing and, investigate the effects of different boundary conditions on the load versus displacement response of the carton.
3. Finite element model development and validation: Develop an FE model of the complete Mk 4 carton and validate the model with experimental results.

The following assumptions and limitations are adopted in this thesis:

- Paper and corrugated paperboard are assumed orthotropic.

- A linear material model is employed.
- Manufacturing variabilities in the paper, corrugated paperboard and packaging are not considered in the analyses.
- The influence of moisture, fatigue and creep are not analysed.



Figure 1.1: Mk 4 telescopic carton (Fadiji, 2015)

### 1.3 Motivation

Packaging plays a vital role in protecting fresh horticultural produce from mechanical damage during storage, transport and distribution processes. Corrugated paperboard has become the industry-standard packaging material for fresh produce. Due to the difficulties in predicting the strength of corrugated paperboard packaging, cartons are often over-designed. Packaging strength is a function of many variables including geometry, changes in temperature and RH, inconsistencies in the manufacturing processes, storage time, and loading conditions such as cyclic loading or misalignments in the stacking pattern.

The objective of this thesis is to develop and validate an FE model of a corrugated paperboard carton and to provide reliable FEM suggestions that can be applied to cartons of different geometries and board compositions. The thesis outcomes will contribute to improving current design methods for optimal carton strength and minimal raw materials required. Improving packaging design methods contributes towards the need to urgently reduce post-harvest losses to increase food security while minimising the negative impacts on the environment. Reducing food losses will also have a positive effect on the agricultural industry's contribution to the national GDP.



# Chapter 2

## Literature study

### 2.1 Corrugated paperboard

Corrugated paperboard is used extensively as a packaging material for fresh horticultural produce (Pathare and Opara, 2014). This section discusses the standardisation, manufacturing processes, and material behaviour of corrugated paperboard.

#### 2.1.1 Board standardisation

Corrugated paperboard is an orthotropic sandwich structure that consists of a corrugated core, called the fluting, glued between two flat paper sheets (or liners) (Emblem and Emblem, 2012; Pathare and Opara, 2014). Twede and Selke (2005) describe the structure of corrugated paperboard as an adaption of classical beam theory where the liners act as two flat load-bearing panels (or flanges) and the fluting acts as a web that separates the panels. Linerboard is made from Kraft paper: a product of the chemical pulping of virgin softwood and sometimes a small percentage of recycled fibres. Kraft paper has long fibres which provide high strength (Twede and Selke, 2005; Emblem and Emblem, 2012). The fluting medium is typically made from a combination of hardwood fibres and a larger percentage of recycled paperboard. It has short fibres to facilitate the forming of the corrugated shape without breaking the paper (Twede and Selke, 2005). The liners provide most of the bending stiffness and compressive strength, and the fluting provides resistance against local buckling (Biancolini *et al.*, 2005). The air gaps in the fluting also act as a thermal insulator to protect produce from fluctuating atmospheric temperatures (Twede and Selke, 2005; Fadiji *et al.*, 2018a).

Figure 2.1 shows the principal material directions of a panel of corrugated paperboard. The machine direction (MD) corresponds to the production direction of the paper reel. The cross direction (CD) is transverse to the MD, in the sheet plane. The local coordinate system of the paper sheet is denoted  $123$ , where  $1$  corresponds to the MD,  $2$  to the CD and  $3$  to the thickness direction. The global

coordinate system of the panel of corrugated paperboard is the Cartesian coordinate system  $xyz$ , where  $x$  corresponds to the MD of the liners.

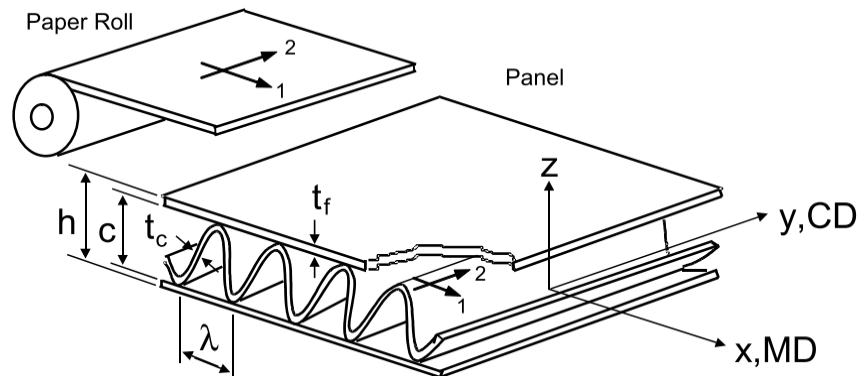


Figure 2.1: Corrugated paperboard geometry and reference directions (Nordstrand, 2004)

The number of flute layers and the flute size can be varied to reduce the mass or increase the strength of the corrugated board (Pathare and Opara, 2014). Figure 2.2 shows the typical board configurations. Single-face board has one liner and one corrugated layer. The result is a flexible material that is typically used for wrapping purposes (Twede and Selke, 2005; Emblem and Emblem, 2012). Single-wall board has three layers, a corrugated layer between two liners. This is the most used board configuration. Double- and triple-wall board are used for heavy-duty applications (Twede and Selke, 2005).

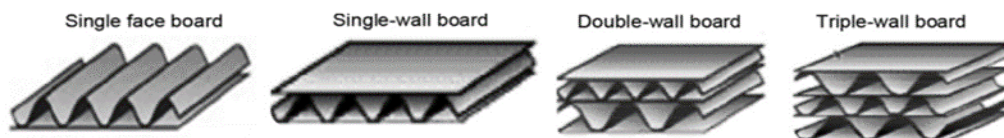


Figure 2.2: Typical corrugated paperboard configurations (Twede and Selke, 2005)

Table 2.1 shows the flute height, wavelength and take-up factors of the standard flute profiles. The take-up factor is the length ratio of un-corrugated fluting medium per unit length of corrugated board (Nordstrand, 2003). Flute profiles are named alphabetically based on the order in which they were invented (Twede and Selke, 2005). A-flute is the thickest of the flute profiles in Table 2.1. Its thickness provides high flexural stiffness and good top-to-bottom compression strength, which is useful in heavy-duty applications (Twede and Selke, 2005; Emblem and Emblem, 2012). B-flute is thinner than A-flute but has more corrugations per metre. The result is a board with better flat crush resistance but a

lower top-to-bottom compression strength. C-flute is a compromise between the advantages and disadvantages of A- and B-flute. It has better printability than A-flute and a greater stacking strength than B-flute. E- and F-flute are the smallest of the flute profiles in Table 2.1 and are typically used for lightweight applications (Twede and Selke, 2005).

Table 2.1: Standard flute profiles (Nordstrand, 2003)

Flute profile	Flute height (mm)	Wavelength (mm)	Take-up factor
A	4.67	8.3–10	1.54
B	2.46	6.1–6.9	1.32
C	3.61	7.1–8.3	1.43
E	1.15	3.2–3.6	1.27
F	0.76	2.3–2.5	1.25

### 2.1.2 The pulping process

The purpose of wood pulping is to separate cellulose fibres from lignin and other impurities (Emblem and Emblem, 2012). Lignin interferes with hydrogen bonding during the papermaking process and, therefore, reduces the strength of the paper (Biermann, 1996). During chemical pulping the chemical structure of lignin is broken down and it is left soluble in water (Biermann, 1996). Mechanical pulping relies on a grinding process to separate fibre bundles. Here the fibres are broken into shorter pieces and lignin is retained in the pulp. Higher pulp yields are obtained during mechanical pulping, but the pulp produces much weaker paper due to the retained lignin and short fibre lengths (Emblem and Emblem, 2012). Neutral sulphite semichemical (NSSC) pulping combines chemical and mechanical pulping to improve the strength and moisture resistance of the fluting medium. NSSC pulp is produced in two stages. First, hardwood chips are chemically treated to weaken interfibre bonding and to remove some of the lignin. Secondly, the pulp is mechanically refined to separate fibres. The retained lignin (15–20%) adds stiffness to the paper. The result is a paper with short fibres to facilitate the corrugation process, but with increased stiffness and strength (Malo, 1967; Biermann, 1996).

### 2.1.3 The corrugation process

The manufacturing process of corrugated paperboard involves a high-precision corrugator. The principal operations of a single-wall corrugator are preconditioning, single-facing, double-backing and heating. The corrugation process starts with the preconditioning of the fluting medium by passing it over a heated cylinder or through a steam shower (Twede and Selke, 2005). The heat and moisture soften the fibres to facilitate the corrugation process (Twede and Selke, 2005;

Fadiji *et al.*, 2018a). The preconditioned paper is then passed between two rotating cylinders with alternating ridges and grooves that form the flute profile (Twede and Selke, 2005). Adhesive is applied to the tips of the fluting as it exits the corrugating cylinders and pressure is used to glue the fluting to the liner. This process is called single-facing. Next, the double-backer applies adhesive to the exposed crests of the single-face board before it is glued to the second liner. The double-face board passes through a heating section to cure the glue and to remove any moisture from the paper (Twede and Selke, 2005; Fadiji *et al.*, 2018a). Figure 2.3 shows the manufacturing process of single-wall corrugated paperboard. Warping and washboarding are two undesired effects of moisture imbalances during the corrugation process. Warping is the deformation of the corrugated board into a buckling shape when one layer has a higher moisture content and, therefore, shrinks more than the other layers when drying (Twede and Selke, 2005; Fadiji *et al.*, 2018a). Washboarding occurs when the starch that glues the liners and flute together shrinks when it dries. It creates dips in the liners that form a ripple pattern parallel to the flutes (Fadiji *et al.*, 2018a).

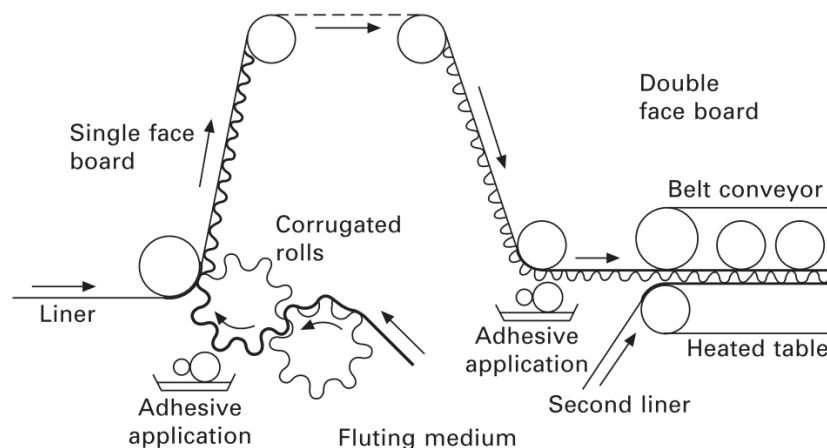


Figure 2.3: Corrugation process of single-wall board (Emblem and Emblem, 2012)

#### 2.1.4 Material behaviour

Figure 2.4 illustrates the stress-strain response of paper under a uniaxial tensile load. The linear elastic zone represents the recoverable deformation that occurs during the initial stretching of fibres. The nonlinear plastic zone is characterized by the unrecoverable deformation that results from fibre slip and fibre rupture (Phongphinitana and Jearanaisilawong, 2012). The tensile strength of paper is stronger in the MD and weaker in the CD. The lower tensile strength in the CD is a result of fibres being pulled apart (Twede and Selke, 2005). Phongphinitana and Jearanaisilawong (2012) demonstrated this by performing uniaxial tensile tests on paper in the MD, CD and  $45^\circ$  to the MD. Figure 2.5 shows that samples ex-

hibited the highest tensile strength and the smallest elongation at rupture in the MD.

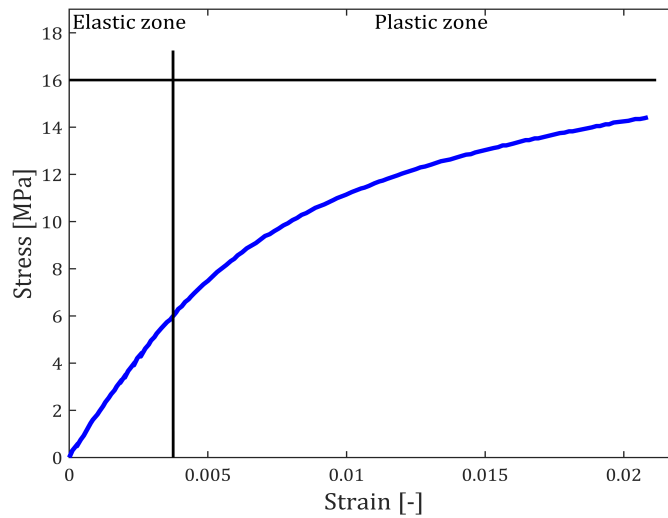


Figure 2.4: Stress-strain response of paper under uniaxial tension (adapted from Phongphinitana and Jearanaisilawong (2012))

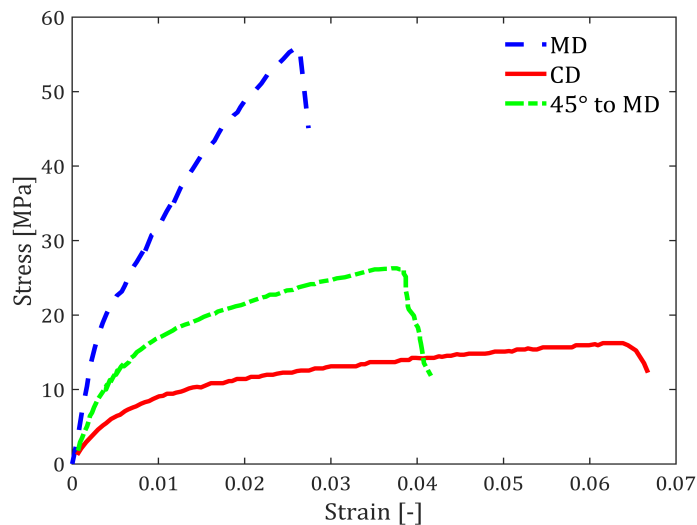


Figure 2.5: Stress-strain response of paper in the MD, CD and 45° to the MD (adapted from Phongphinitana and Jearanaisilawong (2012))

Paper is hygroscopic in nature, meaning it absorbs or releases moisture until it reaches equilibrium with its environment (Twede and Selke, 2005). Paper loses strength and stiffness when subject to high moisture conditions. A study by

Zhang *et al.* (2011) showed a 19% reduction in the edge compression strength of corrugated paperboard when the RH was increased from 30% to 90% over an 8-hour period. Pathare and Opara (2014) reported that the reduction in the compression strength results from the breaking of cellulose bonds between fibres when the moisture content of the material increases.

Corrugated paperboard exhibits fatigue and creep behaviour. Fatigue is the reduction in strength of a material when subject to cyclic loading. (Twede and Selke, 2005) reported a 40% reduction in the compression strength of corrugated paperboard after the first 90 days of storage at 23 °C and 50% RH. Creep is the time-dependent and permanent deformation of a viscoelastic material under a static load (Sorvari, 2009; Callister and Rethwisch, 2015). The typical creep behaviour of a viscoelastic material is shown in Figure 2.6. In the primary region, strain occurs instantaneously with the applied load. Deformation increases at a lower (but constant) strain rate in the secondary region. Most of the permanent deformation occurs in this region. The strain rate then increases sharply in the tertiary region until the material fails (Arvidsson and Grönvall, 2004). Haslach (1994) demonstrated the accelerated creep behaviour of paper under cyclic humidity at a constant tensile load. At 90% RH, the material exhibited a larger initial strain than at 30% RH. When the relative humidity was cycled between 30% and 90%, the material exhibited a higher initial strain as well as an accelerated creep rate, as demonstrated in Figure 2.7.

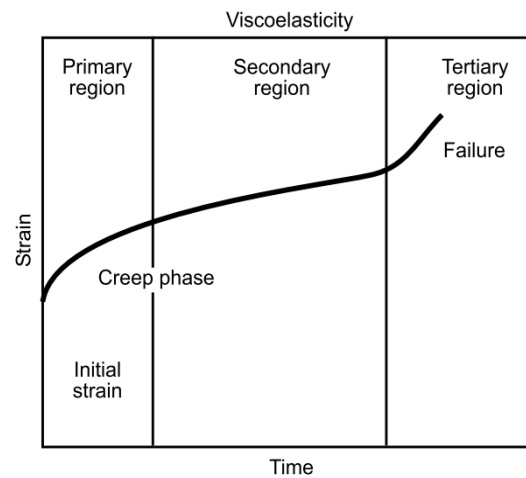


Figure 2.6: Creep behaviour of a viscoelastic material (Arvidsson and Grönvall, 2004)

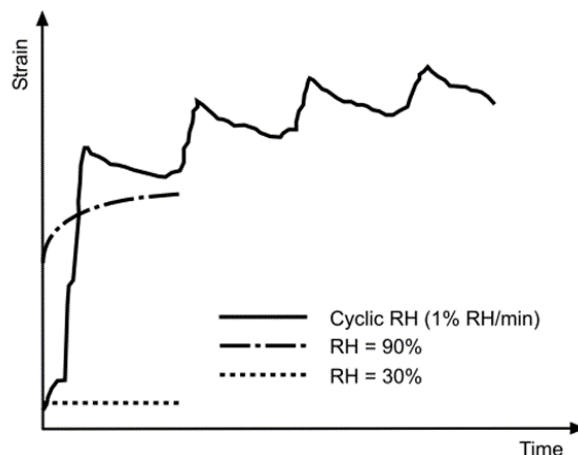


Figure 2.7: Accelerated creep of paper under cyclic humidity (Haslach, 1994)

## 2.2 Performance testing of paper, board and packaging

This section discusses some of the industry-standard test methods that are typically used to measure the mechanical performance of paper, corrugated paperboard and packaging.

### 2.2.1 Paper and paperboard

#### 2.2.1.1 Tensile test

Tensile tests are used to obtain information about the tensile strength, yield strength, ductility and elasticity of paper and paperboard (Twede and Selke, 2005; Fadiji *et al.*, 2018a). The tensile strength of paper-based materials depends on the length and surface area of fibres, fibre strength and the bonding between fibres (Twede and Selke, 2005). Due to the orthotropic nature of paper, tensile tests should be performed in the machine- and cross direction. Standards for the tensile testing of paper and board include ISO 1924-2, TAPPI T494 and ASTM D828.

The ISO 1924-2 test method prescribes the conditioning of samples according to ISO 187. Samples should be pre-conditioned for 24 hours at 10–35% RH and 20–40 °C and conditioned for 24 hours at the standard test conditions for paper and board ( $50 \pm 2\%$  RH and  $23 \pm 1$  °C). Specimens should be clean-cut and undamaged with a width of  $15 \pm 0.1$  mm and a length greater than 180 mm (the clamping length). At least 10 specimens should be tested in each in-plane direction. Tests are carried out at a rate of elongation of  $20 \pm 5$  mm/min.

It is necessary to measure the thickness of each specimen to accurately determine the modulus of elasticity. The ISO 534 practice for measuring paper thickness, however, specifies an anvil diameter of 16 mm which will result in a

larger pressure applied to a 15 mm wide paper strip than the prescribed pressure (British Standard, 2008a). An approximate modulus of elasticity can be determined by measuring the mean thickness of the paper according to ISO 534.

The maximum tensile strength,  $TS$ , expressed in kN/m, is given by

$$TS = \frac{\bar{F}_{max}}{w_i} \quad (2.1)$$

where  $\bar{F}_{max}$  is the mean maximum tensile force and  $w_i$  is the initial width of the specimen. The modulus of elasticity is calculated as follows:

$$E = \frac{\Delta F \times l_i}{\Delta l \times w_i \times t} \quad (2.2)$$

where  $\Delta F$  is the change in force and  $\Delta l$  is the corresponding elongation of the region on the force-elongation curve with the highest slope.  $l_i$  is the initial specimen length (usually 180 mm) and  $t$  is the specimen thickness.

### 2.2.1.2 Short-span compression test

The short-span compression test (SCT) is used to determine the compressive strength in the MD and CD of paper and board. Compression strength is defined as the maximum compressive force per unit width that a specimen of paper or board can support until the onset of failure (British Standard, 2008b). Standards for this test include ISO 9895 and TAPPI T826. The ISO 9895 test method prescribes pre-conditioning and conditioning of specimens according to the ISO 187 practice. A specimen of  $15 \pm 0.1$  mm in width and at least 70 mm in length is clamped with a  $0.7 \pm 0.05$  mm span between clamps. The clamps move towards each other at  $3 \pm 1$  mm/min until the specimen fails. At least 20 specimens should be tested in each in-plane direction to eliminate the influence of local variations in the paper (British Standard, 2008b). The mean sample thickness should be measured according to ISO 534 if the compression strength is required in MPa. The compression strength,  $\sigma_c$ , is determined using Equation 2.3, where  $F$  is the compressive strength in Newtons,  $w$  is the sample width in millimetres, and  $t$  is the sample thickness in millimetres.

$$\sigma_c = \frac{F}{w \times t} \quad (2.3)$$

Popil *et al.* (2004) proposed an empirical model that uses the short-span compression strength and bending stiffness of the linerboard and the fluting medium to predict the edge compression strength of corrugated paperboard. This model allows papermaking processes to be tailored in such a way that will optimise the corrugated paperboard strength and, ultimately, that of the complete carton (Popil *et al.*, 2004; Fadji *et al.*, 2018a).



### 2.2.1.3 Edge compression test

The edge compression test (ECT) measures the force required to edge-crush a sample of corrugated paperboard with its flutes facing upright. There are various industry-standard test methods available. The TAPPI T811 method requires reinforcement of the specimen's loaded edge by dipping it into molten paraffin wax. The ISO 3037 standard is an unwaxed edge method where the sample is held perpendicular to the platens of a compression tester by two metal guide blocks. ISO 3037 uses short rectangular specimens of  $25 \pm 0.5$  mm in height and  $100 \pm 0.5$  mm in width. The edge-crush resistance is reported in force per unit width according to Equation 2.4, where  $\bar{F}_{max}$  is the mean maximum force and  $w$  is the width of the specimen.

$$ECT = \frac{\bar{F}_{max}}{w} \quad (2.4)$$

McKee *et al.* (1963) developed a formula that predicts the top-to-bottom compression strength (BCT) of single-wall corrugated boxes using the edge crush resistance of the corrugated board. This formula is widely used in industry as a quality control method (Fadiji *et al.*, 2018a). McKee's simplified formula is given as

$$BCT = 5.87(ECT)\sqrt{h \times Z} \quad (2.5)$$

where  $h$  is the board thickness and  $Z$  is the box perimeter.

## 2.2.2 Packaging

### 2.2.2.1 Box compression test

Box compression tests (BCT) are used to measure the top-to-bottom compressive resistance of shipping cartons. Standard test methods include ASTM D642 and TAPPI T804. The procedure starts with placing a carton between the platens of a compression tester, centred on the bottom platen. A preload is then applied to ensure that both of the platens are in contact with the carton. ASTM recommends a preload of 222 N for single-wall cartons and 445 N for double-wall cartons. The carton is compressed until failure by lowering the top platen at a rate of  $12.7 \pm 2.5$  mm/min. The point of failure may be specified as a percentage reduction in the load supported by the carton or as an amount of vertical displacement (TAPPI, 2012). It is recommended to test at least five undamaged cartons.

Compression strength may be determined with fixed- or swivel platen compression testers. Fixed platens initiate contact with the highest point of the carton and generally cause specimens to fail at their strongest point, while swivel platens initiate contact with the weakest point of the carton and cause specimens to fail at their weakest point (ASTM International, 2010). Swivel platens provide a more real-world scenario but are likely to result in larger variations in

the test results. It is recommended to use a fixed platen set-up when gathering comparative data (TAPPI, 2012).

Tests are usually performed under ideal laboratory conditions. The BCT, therefore, overestimates the true stacking strength of a carton but provides a good starting point for evaluating overall carton performance (Twede and Selke, 2005; Fadiji *et al.*, 2018a). Fadiji *et al.* (2018a) reported that although the BCT provides valuable information about the failure mode of a carton, it does not consider the decrease in stacking strength that results from storage condition effects such as variations in atmospheric conditions and misalignments in the stacking pattern.

#### 2.2.2.2 Creep test

Creep tests are used to investigate the resistance of paperboard packaging to a constant compressive load for an extended time (ASTM International, 2009). Palletized packages are exposed to inconsistent climatic conditions during storage and transportation. The bottom cartons of a stack are additionally subject to large compressive loads. Understanding the creep response of corrugated paperboard packaging aids in designing cartons to withstand the above-mentioned conditions for the duration of their service life (Fadiji *et al.*, 2018a). Tests can be performed according to the ASTM D7030 test method at standard conditions (23 °C and 50% RH) or any other conditions prescribed in the D4332 practice. Creep tests can be very time consuming, which is why the ASTM D7030 standard demonstrates a method to estimate the time-to-failure of a carton using 12-hour creep and BCT data.

## 2.3 The finite element method

### 2.3.1 Background information

FEM is a numerical method that originated from structural mechanics. The essence of FEM is to divide the entire domain of a structure into a collection of simple sub-domains (or finite elements) and then to find the local solutions of the sub-domains which, when assembled, approximate a global solution (Cook *et al.*, 2002; Kim, 2015).

Mathematical models of structural problems are often formulated as differential equations that are satisfied at every point in the domain. In FEM, the continuous differential equations are discretized so that the solution of each element can be approximated in a simple polynomial form (Kim, 2015). Adjacent elements are connected by sharing node points. The nodes and elements form a mesh to which material and geometric properties can be assigned.

The finite element method consists of three principal operations: pre-processing, analysis and post-processing. Pre-processing involves all the steps in building the computational model. This includes simplifying and modelling the geometry; selecting appropriate element types; defining material properties; and ap-

plying loads, boundary conditions and constraints (Cook *et al.*, 2002; Fadiji *et al.*, 2018b). The analysis step involves the use of a FEM solver to generate matrices that describe the behaviour of each element. The elementary matrices are assembled into a global matrix equation that represents the entire structure:

$$[K] \{D\} = \{F\} \quad (2.6)$$

$[K]$  is the global stiffness matrix,  $\{D\}$  is the displacement vector, and  $\{F\}$  is the external force vector (Cook *et al.*, 2002). The global matrix equation is solved to determine the field values at the nodes. During the post-processing step, the results can be viewed as raw data or displayed graphically.

In structural mechanics, linear systems are defined as systems where the relationship between the input and the output is linear. In other words, the relationship between  $\{F\}$  and  $\{D\}$  is linear (Kim, 2015). Linear systems can always be solved using the system of linear equations described by Equation 2.6. In nonlinear systems, the analysis procedure becomes much more complicated and often requires a sequence of linear analyses (Kim, 2015). Nonlinearity in structural mechanics include:

1. Material nonlinearity: the relationship between stress and strain is not linear and, therefore, the material properties depend on the current state of stress or strain. Examples include nonlinear elasticity, plasticity, creep and progressive failure (Cook *et al.*, 2002).
2. Geometric nonlinearity: the relationships among displacement, rotation and strains are nonlinear. Geometric nonlinearity often occurs when deformations are large and the equilibrium equations must be formulated for the deformed geometry (Cook *et al.*, 2002; Kim, 2015).
3. Contact nonlinearity: the gap between adjacent parts can open or close or the contact area between parts change as the force changes. In other words, the location and the value of the boundary condition on a specific boundary can be unknown (Cook *et al.*, 2002; Kim, 2015).

### 2.3.2 FEM applied to corrugated paperboard and corrugated paperboard structures

FEM has gained popularity as a design tool because its application allows users to evaluate the performance of new designs without having to rely entirely on prototyping and experimental analyses. It, therefore, optimises the 'design-prototype-test-redesign' procedure (Fadiji *et al.*, 2018b). It has featured in several studies as a method to investigate the mechanical behaviour of corrugated paperboard and related packaging.

Various types of nonlinearities are present in modelling corrugated paperboard structures, which makes it an increasingly difficult task. Nonlinearities

include the nonlinear material behaviour of paper, geometric nonlinearities that result from large displacements when cartons are compressed, and touching contact between the inner- and outer cartons of telescopic package designs. Another difficulty in modelling corrugated paperboard structures is the complex geometry of the material. A very fine mesh would be required to model an entire structure with the detailed geometry of the corrugated core, ultimately resulting in a very computationally expensive model (Marek and Garbowski, 2015). For this reason, homogenisation methods to model the material using equivalent shell elements is a topic of great interest in the research field.

Briassoulis (1986) presented a numerical method for modelling an element of the corrugated core as an equivalent plane-stress element. The author modelled a detailed section of the corrugated core to which constant states of strain were applied. The stress resultants were then extracted to determine the equivalent elastic properties using the orthotropic stress-strain relation of a plane-stress element.

Carlsson *et al.* (2001) presented an analytical approach for determining the elastic stiffnesses of a corrugated core sandwich panel. The method is based on laminated plate theory and first-order shear deformation theory. The authors approximated the corrugated core as an equivalent homogeneous core with effective properties:

$$E_1^* \approx 0 \quad (2.7a)$$

$$E_2^* = \alpha E_{2,c} t_c / h_c \quad (2.7b)$$

$$\nu_{12}^* \approx 0 \quad (2.7c)$$

$$G_{12}^* \approx 0 \quad (2.7d)$$

where  $\alpha$  is the take-up factor of the corrugated core,  $E_{2,c}$  is the modulus of elasticity of the core paper in the CD,  $t_c$  is the thickness of the core paper and  $h_c$  is the height of the core. They predicted that the panel's in-plane extensional and shear stiffnesses and bending and twisting stiffnesses are dominated by the extensional and shear stiffnesses of the liners. Predictions agreed well with measured data. The authors, however, found that measured transverse shear stiffnesses were substantially lower than analytically and numerically predicted values. They attributed the lower transverse shear stiffnesses to delamination damage of the core's web during the corrugation process and the change of the flute profile from sinusoidal to semi-circular during the lamination process. The authors also mention that transverse shear stiffnesses would further reduce if the bond between the liners and core is flexible.

Nordstrand (1995) investigated the post-buckling strength of corrugated paperboard panels using FEM. The author examined the sensitivity of the panel's buckling load to changes in the transverse shear stiffnesses of the core and the magnitude of initial out-of-plane imperfections, amongst other parameters. The author used a homogenisation method for the corrugated core similar to the method described by Carlsson *et al.* (2001). The transition of the corrugated core

to a homogeneous core is shown in Figure 2.8. Nordstrand mentions that homogenised plate analysis assumes constant shear strain and stress through the thickness and it is, therefore, common to reduce the transverse shear moduli by a shear correction factor,  $f$ , to account for the excessive amount of shear strain energy produced. The author also mentions that this is only required when the bending stiffnesses of the layer contribute significantly to the total bending stiffness of the panel. Since the corrugated core's bending stiffnesses are inherently lower than those of the liners, shear correction should not be applied to the core.

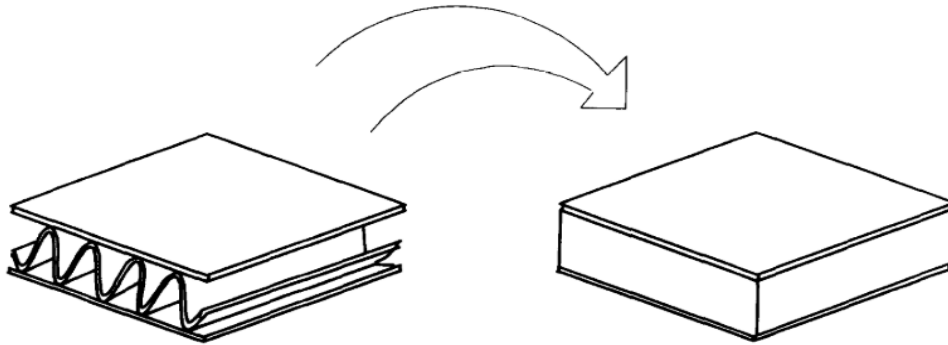


Figure 2.8: Transition of the corrugated core to an equivalent homogeneous core (Nordstrand, 1995)

The author found good agreement between the buckling load obtained by the FE model and the theoretical buckling load when adjustments to the core's transverse shear moduli were excluded, and the transverse shear moduli of the liners were reduced. Initial geometric imperfections were applied by changing the panel's shape to a slightly curved shape that is described by the product of two sine functions of amplitude  $w_0$ . Varying  $w_0$  from 0.1 mm to 1 mm had little effect on the buckling load of a 400 mm  $\times$  400 mm panel, but a large (although unlikely) imperfection of 10 mm reduced the buckling load by about 40%.

Biancolini and Brutti (2003) studied the buckling behaviour of corrugated paperboard packages using FEM. The authors modelled a rectangular section of corrugated paperboard with the detailed geometry of the core included and simulated an edge compression test. The model was verified by comparing the numerical buckling load to experimentally obtained ECT values. The authors then extracted a section of the detailed FE model and imposed in-plane tensile- and shear stresses and out-of-plane flexure and torsion. The general laminate force-deformation equation was used to extract the stiffness properties of an equivalent homogeneous element. The laminate force-deformation equation is given

by

$$\begin{Bmatrix} N_x \\ N_y \\ N_{xy} \\ M_x \\ M_y \\ M_{xy} \end{Bmatrix} = \begin{bmatrix} A & B \\ B & D \end{bmatrix} \begin{Bmatrix} \varepsilon_x \\ \varepsilon_y \\ \gamma_{xy} \\ \kappa_x \\ \kappa_y \\ \kappa_{xy} \end{Bmatrix} \quad (2.8)$$

and can be written in a condensed form as

$$\begin{Bmatrix} N \\ M \end{Bmatrix} = \begin{bmatrix} A & B \\ B & D \end{bmatrix} \begin{Bmatrix} \varepsilon \\ \kappa \end{Bmatrix} \quad (2.9)$$

The extensional stiffness matrix  $[A]$  is a  $3 \times 3$  matrix that relates the in-plane forces  $\{N\}$  to the strains  $\{\varepsilon\}$ . The bending stiffness matrix  $[D]$  relates the moments  $\{M\}$  to the curvatures  $\{\kappa\}$ . Matrix  $[B]$  couples the extensional and bending responses (Gibson, 2007). For symmetric laminates, the  $[B]$  matrix is zero (Jones, 1999). The homogenisation process was validated by comparing the results from a static- and buckling analysis of the detailed FE model and the homogenised FE model. A complete container was then modelled using the homogenised element, and a BCT was simulated. The authors concluded that, when compared to measured BCT values, the FE model predicted the load at which the structure becomes unstable (the buckling load) with reasonable accuracy.

Biancolini (2005) presented a numerical homogenisation approach that is based on energy equivalence. The first step is the static condensation of a section of corrugated paperboard modelled with the core's detailed geometry. Static condensation involves removing all internal nodes, leaving only the boundary nodes, as demonstrated in Figure 2.9. The structure can then be represented by the condensed matrix equation:

$$[\bar{K}] \{u_e\} = \{F_e\} \quad (2.10)$$

Loads and displacements at the external nodes are given by  $\{F_e\}$  and  $\{u_e\}$ , respectively, and  $[\bar{K}]$  is the condensed stiffness matrix. For a given displacement vector  $\{u_e\}$ , the total elastic energy stored in the structure is

$$E = \frac{1}{2} \{u_e\}^T \{F_e\} \quad (2.11)$$

Substituting 2.10 into 2.11 gives:

$$E = \frac{1}{2} \{u_e\}^T [\bar{K}] \{u_e\} \quad (2.12)$$

Energy equivalence between the condensed model and an equivalent homogeneous plate was established by, first, substituting strain vectors in the place of

the displacement vectors in Equation 2.12, using a displacement field transformation matrix. Then, the condensed model's energy equation was set equal to the internal strain energy of a shell subject to bending. The strain vectors cancel out, and the equivalent stiffness matrix of the shell is given by

$$[ABD] = \frac{[A_e]^T [\bar{K}] [A_e]}{\{area\}} \quad (2.13)$$

where  $[A_e]$  is the displacement field transformation matrix. The method was validated by comparing numerical results to analytical solutions.

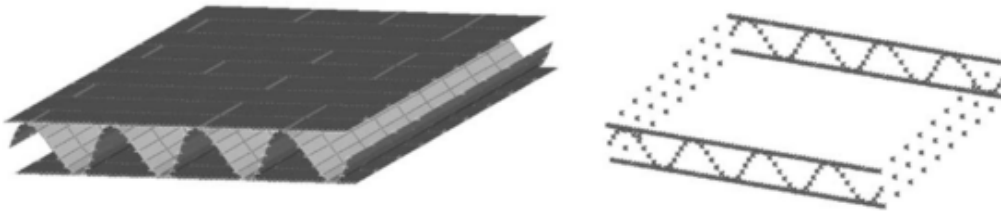


Figure 2.9: Static condensation of a corrugated paperboard panel (Biancolini, 2005)

Beldie *et al.* (2001) investigated the mechanical behaviour of corrugated paperboard packages under static compression using FEM. The authors tested and modelled a panel of corrugated paperboard subject to edge compression to check the material model. Next, they divided a full package into three segments, as shown in Figure 2.10. Each segment's response under static compression was evaluated to determine its contribution to the overall response of the package. Finally, the response of the whole package was studied. The authors modelled the material as an orthotropic, linear, elastic-plastic material and described the plasticity using Hill's orthotropic yield criterion. They selected four-node doubly curved thick-shell elements with reduced integration to model the package. The folds on the top and bottom of the package were modelled by applying triple thickness where three sheets of paperboard would overlap. Initial bulging of the panels, package segments and the whole package, were measured and imposed as geometric imperfections on the models.

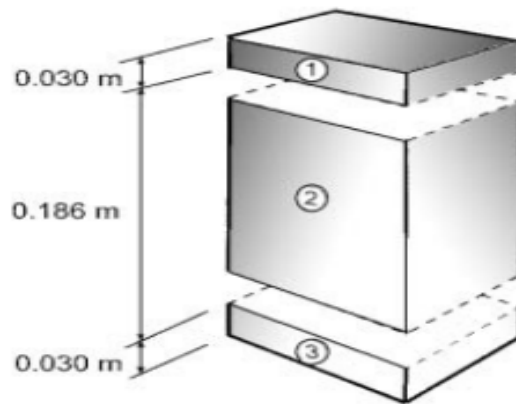


Figure 2.10: A paperboard package divided into three segments (Beldie *et al.*, 2001)

The authors compared the load-displacement path from the FEM simulation to measured data for each of the three parts: edge compression of the panels, top-to-bottom compression of the package segments, and top-to-bottom compression of the whole package. The authors found good agreement between the results from simulations and experiments for panels with a height-to-width ratio of two or more. The agreement between the simulations and the experiments deteriorated as the panel height was reduced. The simulations showed an increase in panel stiffness for shorter panels, while experimental results showed no significant change. The authors attributed the discrepancies between simulations and experiments to geometric imperfections in the panels. In the second part of their study, the authors found discrepancies between the simulated and measured results of the top and bottom segments. They attributed this to the simplification of the horizontal creases (or folds). The creased areas consist of delaminated paperboard and, therefore, no longer have the same material properties as the rest of the package. The authors concluded that more work needs to be done to understand the material behaviour at the crease lines.

Fadiji *et al.* (2016) used FEM to study the effects of vent geometry and vent orientation on the compression strength of telescopic corrugated paperboard cartons. The authors modelled the material as an orthotropic, three-ply laminate with a homogeneous core. The equivalent stiffness properties of the core were determined using the method presented by Briassoulis (1986) and extended by Biancolini (2005). A linear buckling analysis was used to determine the most likely buckling shape and the critical buckling load of the carton. The authors found that the buckling load of the carton decreases when (a) the vent area is increased, (b) the vent height is increased, and (c) the vent shape is changed from oblong to circular. This study demonstrates the use of FEM as a design tool for packaging.



### 2.3.3 Calculation of buckling loads

Buckling occurs when the equilibrium configuration of a structure becomes unstable. There are two typical ways in which a structure may buckle: bifurcation buckling or nonlinear collapse (limit-point buckling) (Sun *et al.*, 1995). Bifurcation buckling occurs when the reference (pre-buckled) configuration of a structure and an alternative buckled configuration is possible at the same load. In other words, the load-displacement path forks into two branches (Jones, 1999; Cook *et al.*, 2002). Nonlinear limit-point buckling occurs when the stiffness of a structure (or the slope of the load-displacement path) decreases under an increasing load. The limit-point is the point where the stiffness matrix of the structure becomes singular, and its load-carrying capacity decreases rapidly until failure (Sun *et al.*, 1995; Cook *et al.*, 2002). Thin-walled structures (plates and shells) typically have membrane stiffnesses that are several orders of magnitude larger than their bending stiffnesses. Under in-plane loading, plates can store large amounts of membrane strain with small deformations. When buckling occurs, large bending deformations are required to absorb the membrane strain energy released (Cook *et al.*, 2002). A geometrically perfect plate or shell may sustain further load after bifurcation (in the post-buckled state) but at decreased stiffness (Jones, 1999).

An eigenvalue buckling analysis can be used to predict the critical buckling load and the buckling mode of a structure. For a structure loaded with a reference external load  $\{R\}_{ref}$ , the resulting stress stiffness matrix  $[K_{\sigma}]_{ref}$  can be obtained from a standard linear static analysis (Cook *et al.*, 2002). When the reference load is intensified by a factor  $\lambda$ , the resulting stress field will intensify by the same factor:

$$\{R\} = \lambda \{R\}_{ref} \quad (2.14)$$

$$[K_{\sigma}] = \lambda [K_{\sigma}]_{ref} \quad (2.15)$$

Given that the conventional stiffness matrix  $[K]$  of a linear system remains unchanged by loading and that externally applied loads do not change at the bifurcation point, the system can be described by the following two matrix equations at the bifurcation point:

$$([K] + \lambda_{cr} [K_{\sigma}]_{ref}) \{D\}_{ref} = \lambda_{cr} \{R\}_{ref} \quad (2.16)$$

$$([K] + \lambda_{cr} [K_{\sigma}]_{ref}) \{D_{ref} + \delta D\} = \lambda_{cr} \{R\}_{ref} \quad (2.17)$$

where  $\{D\}_{ref}$  is the displacements prior to buckling and  $\{\delta D\}$  is the buckling displacements (Cook *et al.*, 2002). Subtracting 2.16 from 2.17 yields the eigenvalue problem:

$$([K] + \lambda_{cr} [K_{\sigma}]_{ref}) \{\delta D\} = 0 \quad (2.18)$$

The critical buckling factor  $\lambda_{cr}$  defines the smallest load for which there is bifurcation. The eigenvector  $\{\delta D\}$  is the buckling mode shape associated with

$\lambda_{cr}$ . Equation 2.18 implies that the net stiffness of the system is reduced to zero at the critical load. Mathematically, the net stiffness matrix becomes singular with a zero determinant (Cook *et al.*, 2002). Nonlinear buckling problems (post-buckling collapse or buckling of plates with initial geometric imperfections) can be solved using a sequence of eigenvalue analyses based on the incremental stiffness matrices (Jones, 1999; MSC Software Corporation, 2019).

## Chapter 3

# Materials testing and modelling

This chapter contains a discussion of the experimental, analytical and numerical methods that were used to develop a valid corrugated paperboard material model.

### 3.1 Required material properties

The components of corrugated paperboard (i.e. the linerboard and fluting medium) are approximated as orthotropic. For simplification, a linear material constitutive model is employed in this thesis. The properties of orthotropic materials differ in the three principal material directions, and the constitutive relation is given by

$$\{\varepsilon\}_{123} = [C]_{123} \{\sigma\}_{123} \quad (3.1)$$

where the compliance matrix is

$$[C]_{123} = \begin{bmatrix} \frac{1}{E_1} & -\frac{\nu_{21}}{E_2} & -\frac{\nu_{31}}{E_3} & 0 & 0 & 0 \\ -\frac{\nu_{12}}{E_1} & \frac{1}{E_2} & -\frac{\nu_{32}}{E_3} & 0 & 0 & 0 \\ -\frac{\nu_{13}}{E_1} & -\frac{\nu_{23}}{E_2} & \frac{1}{E_3} & 0 & 0 & 0 \\ 0 & 0 & 0 & \frac{1}{G_{12}} & 0 & 0 \\ 0 & 0 & 0 & 0 & \frac{1}{G_{13}} & 0 \\ 0 & 0 & 0 & 0 & 0 & \frac{1}{G_{23}} \end{bmatrix} \quad (3.2)$$

Symmetry of the compliance matrix leads to

$$\frac{\nu_{12}}{E_1} = \frac{\nu_{21}}{E_2}, \quad \frac{\nu_{13}}{E_1} = \frac{\nu_{31}}{E_3}, \quad \frac{\nu_{23}}{E_2} = \frac{\nu_{32}}{E_3} \quad (3.3)$$

The above relations show that only nine independent elastic constants are required to completely characterize the elastic behaviour of an orthotropic material (Mann *et al.*, 1979; Allansson and Svärd, 2001).

The in-plane elastic moduli,  $E_1$  and  $E_2$ , can be determined from standard tensile test data. The other elastic constants are not as straightforward to measure

due to the anisotropy of the material and the small dimension in the thickness direction. The out-of-plane elastic modulus  $E_3$  can be approximated using Mann *et al.* (1979)'s relation for machine-made paper:

$$E_3 = \frac{E_1}{190} \quad (3.4)$$

The shear moduli can be approximated using the relations presented by Baum (1981) and Baum *et al.* (1981):

$$G_{12} = 0.387\sqrt{E_1E_2} \quad (3.5)$$

$$G_{13} = \frac{E_1}{55} \quad (3.6)$$

$$G_{23} = \frac{E_2}{35} \quad (3.7)$$

There are a few different approaches that can be followed to determine the in-plane Poisson's ratio,  $\nu_{12}$ . The Poisson's ratio of paper increases with tensile strain (Jones, 1967). For a linear material model, the in-plane Poisson's ratio is, therefore, usually measured at very small loads or extrapolated back to the undeformed state on a Poisson's ratio versus tensile strain curve (Jones, 1967; Schulgasser, 1983; Miller, 2013). Traditional contact measurement devices (e.g. extensometers or strain gauges) are not suitable for determining the Poisson's ratio of paper due to the anisotropy of the material and the microscopic size of deformations in the transverse direction (Schulgasser, 1983; Cao *et al.*, 2012; Miller, 2013).

Baum (1981) used ultrasonic methods to determine the in-plane elastic constants of paper. In ultrasonic methods, wave velocities are determined by measuring the propagation time of a short burst (pulse) of sine waves through the specimen. There are direct relations between the wave velocities and the elastic constants of a material. Baum (1981) discovered a useful relationship between the in-plane Poisson's ratios:

$$\sqrt{\nu_{12}\nu_{21}} = 0.293 \quad (3.8)$$

where  $\nu_{12}$  is the ratio of lateral contraction in the CD to elongation in the MD.

Schulgasser (1981) determined a theoretical relationship between the Poisson's ratio and the ratio of the in-plane elastic moduli  $E_1/E_2$  of paper:

$$\nu_{12} = \frac{1}{6} \left[ (\xi^2 + 14\xi + 1)^{1/2} - (1 + \xi) \right] \quad (3.9)$$

where  $\xi = E_1/E_2$ . This relationship is based on Cox's classical model for paper, which assumes that the individual fibres of an ideal sheet of paper, subject to a homogeneous strain field, experience the same axial strain as the global axial strain of the paper sheet (Cox, 1952; Schulgasser, 1981).

Cao *et al.* (2012) determined the Poisson's ratio of Kraft paper using digital image correlation (DIC), a non-contact method for measuring full-field displacement and strains. DIC divides a randomly patterned surface into smaller sections (or subsets) and tracks their displacements using a series of images taken of the deforming surface, starting from its undeformed reference position (Sutton *et al.*, 2010; Pritchard *et al.*, 2013). Cao *et al.* (2012) used DIC to measure axial and transverse strains during paper tensile testing to determine the ratio

$$\nu_{12} = -\varepsilon_t / \varepsilon_a \quad (3.10)$$

where  $\varepsilon_t$  is the transverse strain, and  $\varepsilon_a$  is the axial strain associated with elongation in the MD. The authors used the strain data that corresponds to the linear-elastic region of the tensile force versus elongation curve. They reported that the deformation field is inherently inhomogeneous due to the anisotropy of the material.

The Tsai-Wu tensor polynomial is one of the most commonly used failure criteria for paper because it accounts for anisotropic strengths and different strengths in compression and tension. It has been used by several researchers for the failure prediction of the facings (liners) of corrugated paperboard based on the hypothesis that failure of the board is initiated by the material failure of the liners (Nordstrand, 1995, 2003). The Tsai-Wu failure criterion for the plane-stress condition is given by

$$F_1\sigma_x + F_2\sigma_y + F_{11}\sigma_x^2 + F_{22}\sigma_y^2 + F_{66}\tau_{xy}^2 + 2F_{12}\sigma_x\sigma_y = 1 \quad (3.11)$$

where

$$F_1 = \frac{1}{\sigma_{1,t}} + \frac{1}{\sigma_{1,c}}, \quad F_2 = \frac{1}{\sigma_{2,t}} + \frac{1}{\sigma_{2,c}}, \quad F_{11} = -\frac{1}{\sigma_{1,t}\sigma_{1,c}}, \quad F_{22} = -\frac{1}{\sigma_{2,t}\sigma_{2,c}}, \quad (3.12)$$

$$F_{66} = \frac{1}{\tau^2}$$

The tensile and compressive strengths in the MD and CD are denoted  $\sigma_{j,t(j=1,2)}$  and  $\sigma_{j,c(j=1,2)}$ , respectively. Nordstrand (1995) and Allansson and Svärd (2001) used the following approximations for the shear strength  $\tau$  and the interaction term  $F_{12}$  of paper:

$$\tau = 0.78\sqrt{\sigma_{1,c}\sigma_{2,c}} \quad (3.13)$$

$$F_{12} = -0.36\sqrt{F_{11}F_{22}} \quad (3.14)$$

## 3.2 Materials testing and results

The Mk 4 telescopic carton (see Figure 1.1) has an inner carton with a C-flute board combination of 250KL/150SC/250KL, and an outer carton with a B-flute

board combination of 175KL/150SC/175KL. The abbreviations 250KL, 175KL and 150SC indicate the paper grammages and types: 250 gsm (grams per square metre) virgin Kraft liner, 175 gsm virgin Kraft liner and 150 gsm semichemical fluting paper. This section discusses the various materials testing methods that were used to measure the elastic properties of the three paper types, and the combined properties of the board.

### 3.2.1 Industry-standard test methods

Standard tensile testing procedures were used to determine the in-plane elastic moduli and the tensile strength in the MD and CD of the paper. Tensile tests were performed according to the ISO 1924-2 practice, as described in Section 2.2.1.1, on ten specimens in each in-plane direction. A Lorentzen & Wettre tensile tester was used. Samples for the material tests were taken directly from a paper reel at random locations. All samples were preconditioned and conditioned according to ISO 187. Prior to the tensile tests, the mean paper thickness was measured using a Messmer Büchel digital micrometer. The mean paper thickness is the average value of 25 measurements (five unique measurements on each of five A4 paper sheets). Equations 2.1 and 2.2 were used to calculate the in-plane elastic moduli and tensile strengths from the tensile test data.

A Messmer Büchel short-span compression tester was used to measure the compression strength in the MD and CD of the paper. Tests were carried out according to the ISO 9895 practice, described in Section 2.2.1.2. A sample size of 40 MD specimens and 40 CD specimens was used to eliminate the effect of local variations in the paper since the clamping length is only 0.7 mm long.

ECT experiments were carried out according to the ISO 3037 standard, described in Section 2.2.1.3. Ten 100 mm × 25 mm C-flute specimens were tested. The specimens were conditioned for 24 hours at 23 °C and 50% RH. The results from the material tests are summarised in Section 3.2.3.

### 3.2.2 Digital image correlation

Digital image correlation was used to measure the in-plane Poisson's ratio. The experimental setup included the Lorentzen & Wettre tensile tester, StrainMaster Portable DIC system and StrainMaster image correlation software. A single 5-megapixel CCD camera (the Imager E-lite 5 M) was used for 2D image capturing. An LED linear light was used to eliminate any shadows on the specimen. The camera was positioned at 335 mm from the tensile specimen for it to occupy a good portion of the field of view. The aperture was set to f/1.6. The experimental setup is illustrated in Appendix B (Figure B.4). At the start of the experiment, the setup was calibrated using StrainMaster's recommended protocol.

According to Sutton *et al.* (2010), there are two rules of thumb for appropriate subset patterning: speckles should be sampled by at least 3 × 3 pixels, and each subset should contain at least 3 × 3 speckles. Ellis (2017) summarised that the

spatial resolution of the data improves when the subset size is reduced, but as a result, the uncertainty in the strain calculation increases with the reduction in the number of speckles (unique features) per subset. Figure 3.1 illustrates the chosen subset size and speckle pattern. An 81-pixel subset size was found to comply with both rules of thumb mentioned above without compromising the spatial resolution. The speckle pattern was created by applying a light coat of matt white paint to the specimen with a sponge and spraying matt black speckles of different sizes over the painted surface.

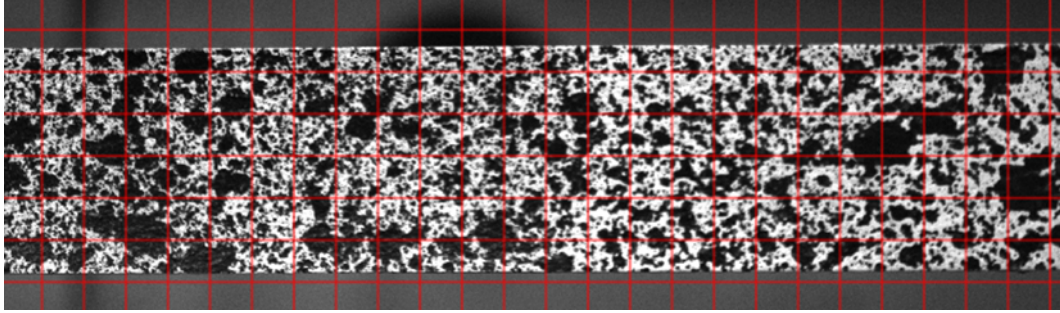


Figure 3.1: Tensile specimen speckle pattern and subset size

Two reference images were taken of the specimen before deformation. The displacements calculated by the DIC software should be zero for these images, and any nonzero values are, therefore, erroneous. The root mean square (RMS) values of the displacement errors are given in Table 3.1. The results show that displacement errors are smaller than 2  $\mu\text{m}$ .

Table 3.1: DIC displacement errors of the paper tensile specimen

Subset size (pixel)	RMS $\delta x$ ( $\mu\text{m}$ )	RMS $\delta y$ ( $\mu\text{m}$ )
81	1.911	1.680

As mentioned in Section 3.1, Poisson's ratio increases with tensile strain. In this work, a least-squares method was used to fit a second-order polynomial to the Poisson's ratio versus axial strain data obtained using DIC. Poisson's ratio was extrapolated from the polynomial at zero axial strain, according to Equation 3.15.

$$\nu_0 = \lim_{\varepsilon_a, \varepsilon_t \rightarrow 0} \nu(\varepsilon_a, \varepsilon_t) \quad (3.15)$$

The method described above is based on the work presented by Miller (2013). The author averaged the strain values over the entire region of interest to calculate a Poisson's ratio for each frame. Due to the high degree of inhomogeneity

of the paper specimen strain fields, it was chosen to approximate the Poisson's ratio for each frame using the average of the Poisson's ratios calculated for each element in the strain field (as opposed to using the average strain values). Elementary Poisson's ratios were calculated according to

$$v_{xy}(m, n) = -\frac{\varepsilon_t(m, n)}{\varepsilon_a(m, n)} \quad (3.16)$$

where  $m$  and  $n$  indicate the location of the element in the strain field and the strain values are Hencky strains given by  $\ln(1 + \varepsilon_{eng})$  (Pritchard *et al.*, 2013).

The axial and transverse strain fields of a 250KL specimen are illustrated in Figure 3.2 at an average elongation of 0.35 mm. The axial strain field is positive over the entire region of interest, and the lateral strain field is expected to be entirely negative. The DIC results, on the other hand, show positive lateral strain near the corners of the specimen, which results in negative Poisson's ratios at those locations. A mask was created for each frame to identify and ignore the data points at locations with positive lateral strain.

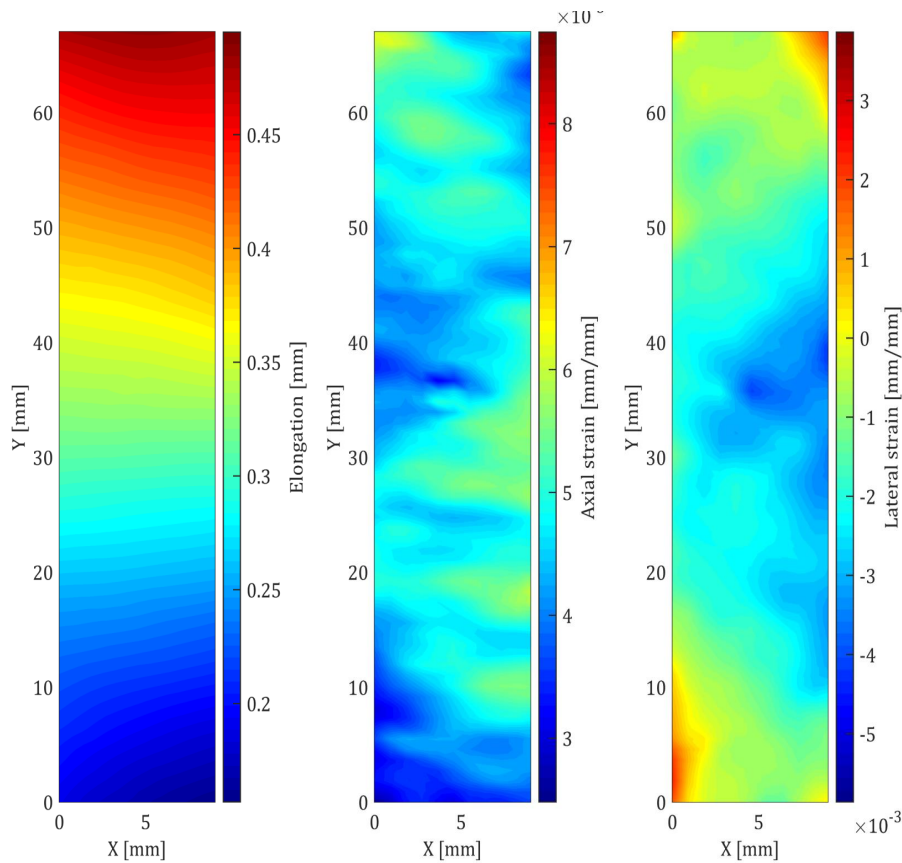


Figure 3.2: DIC displacement and strain fields of a 250KL tensile specimen

The Poisson's ratio versus axial strain curve of the same 250KL specimen is given in Figure 3.3. The curve agrees with Jones (1967)'s observation that the



Poisson's ratio of paper increases with tensile strain. Three 250KL samples were analysed and gave Poisson's ratios of 0.38, 0.37 and 0.42, respectively.

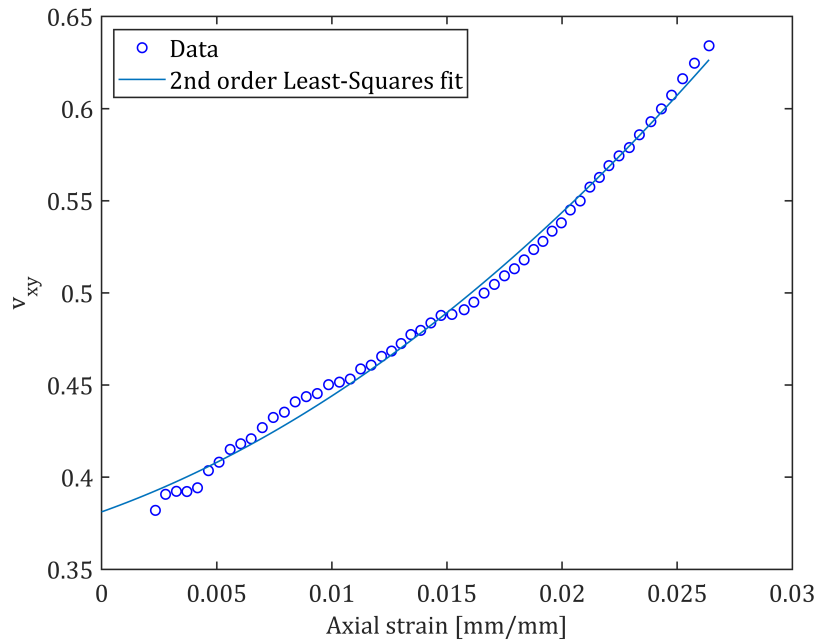


Figure 3.3: Poisson's ratio vs. axial strain of a 250KL specimen

There were several challenges in using DIC to determine the in-plane Poisson's ratio. Close observation of the DIC images showed that the free edges of the specimens seemed to curl inward at the start of the test. This effect is likely a result of how the paint dried after the speckle pattern was applied. The uncurling of the specimen edges during elongation implicates the DIC strain calculations significantly since it gives the impression that the specimen expands in the transverse- and axial directions. Therefore, the reference image for the strain calculation was chosen as the first image after the specimen has visibly straightened out. It should be noted that the displacement errors in Table 3.1 are expected to reduce once the specimen has straightened out since the 2D setup was calibrated for a flat specimen. The data used for the calculation of the values in Table 3.1, however, had to be captured at the start of the test when deformations were still zero.

DIC results of the 150SC and 175KL specimens showed significant variation, such that a second-order least-squares fit could not be applied to the data. Therefore, the data could not be used for calculating Poisson's ratio. Considering that both paper types have lower grammages than 250KL, the effect of the paint on the deformation behaviour could have been more significant for the 150SC and 175KL specimens. Further research needs to be done on application methods for speckle patterns on unbleached paper samples, which are both thin and moisture sensitive.

### 3.2.3 Results

In Sections 3.2.1 and 3.2.2, the materials testing methods that were used to determine three of the nine independent elastic constants of 250KL, 175KL and 150SC paper, were presented. The results are summarised in Table 3.2. The rest of the independent elastic constants will be approximated using well-known empirical relationships. The elastic modulus in the thickness direction and the shear moduli will be approximated using Equations 3.4–3.7. The remaining two elastic constants are the out-of-plane Poisson's ratios. These will be set to 0.01, as suggested by Nordstrand (1995). An average edge compression strength of  $7.2 \pm 0.3$  kN/m was calculated for C-flute board using Equation 2.4 and the measured ECT data. The results from the material tests are in the same range as the values reported by Nordstrand (1995), Biancolini and Brutti (2003) and Biancolini *et al.* (2010) for similar paper types.

Table 3.2: Summary of the measured elastic properties and standard deviations

	Thickness ( $\mu\text{m}$ )	$E_1$ (MPa)	$E_2$ (MPa)	$\nu_{12}$
150 SC	$251 \pm 4$	$4709 \pm 138$	$2918 \pm 147$	-
175 KL	$243 \pm 2$	$8032 \pm 669$	$2369 \pm 118$	-
250 KL	$345 \pm 4$	$6695 \pm 201$	$2310 \pm 139$	$0.39 \pm 0.03$
	$\sigma_{1,t}$ (MPa)	$\sigma_{2,t}$ (MPa)	$\sigma_{1,c}$ (MPa)	$\sigma_{2,c}$ (MPa)
150 SC	$45.3 \pm 2.4$	$30.7 \pm 1.7$	$22.1 \pm 1.4$	$17.5 \pm 1.1$
175 KL	$76.9 \pm 4.7$	$24.8 \pm 1.5$	$26.6 \pm 1.5$	$13.6 \pm 0.8$
250 KL	$68.0 \pm 2.9$	$23.3 \pm 1.4$	$24.1 \pm 1.7$	$12.9 \pm 1.2$

The measured Poisson's ratio of 250KL paper was compared to Baum's empirical relation (Equation 3.8), which can be written as

$$\nu_{12} = 0.293 \sqrt{E_1/E_2} \quad (3.17)$$

The Poisson's ratio, from Baum's relation and the measured in-plane elastic moduli, is 0.5. The error between this value and the measured value of 0.39 is 19.6%. Biancolini *et al.* (2005) reported a similar size error of 20.6% between their measured Poisson's ratio (using DIC) and the empirical value for 200 gsm Kraft liner. The sample size used for the DIC analysis in this experiment was too small to provide satisfactory confidence in the results. For this reason, the Poisson's ratios for the material model will be approximated using Baum (1981)'s relation.

### 3.3 Homogenisation of the corrugated core

This section discusses the analytical homogenisation approach that was followed to determine the equivalent elastic properties of the corrugated core. An approach based on classical laminated plate theory (CLPT), similar to the methods presented by Talbi *et al.* (2009) and Marek and Garbowski (2015), was followed. The first step is to transform the fluting medium's constitutive relation from the local coordinate system, in which the material properties were measured, to the global coordinate system of the corrugated paperboard panel. The constitutive relation is then homogenised through the thickness and along the MD. The MATLAB script that was used to calculate the equivalent elastic properties of the homogeneous core is included in Appendix A.

Figure 3.4 illustrates the corrugation profile. The distance from the centre line to the corrugated sheet is given by

$$H(x) = \frac{h_c}{2} \sin\left(2\pi \frac{x}{P}\right) \quad (3.18)$$

and the incline angle of the corrugated sheet as a function of  $x$  is

$$\theta(x) = \arctan\left(\frac{dH(x)}{dx}\right) \quad (3.19)$$

where  $h_c$  is the core height and  $P$  is the wavelength of the flute profile (Talbi *et al.*, 2009).

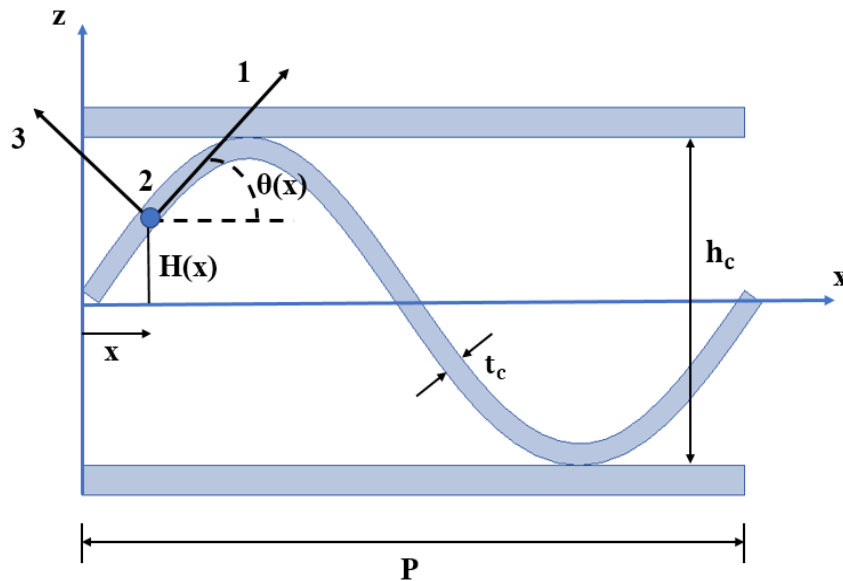


Figure 3.4: Corrugated core profile

Strains and stresses can be transformed between the two reference coordinate systems according to

$$\{\varepsilon\}_{xyz} = [T_\varepsilon] \{\varepsilon\}_{123} \quad (3.20)$$

$$\{\sigma\}_{123} = [T_\sigma] \{\sigma\}_{xyz} \quad (3.21)$$

where  $[T_\varepsilon]$  and  $[T_\sigma]$  are the strain and stress transformation matrices

$$[T_\varepsilon] = \begin{bmatrix} c^2 & 0 & s^2 & 0 & -sc & 0 \\ 0 & 1 & 0 & 0 & 0 & 0 \\ s^2 & 0 & c^2 & 0 & sc & 0 \\ 0 & 0 & 0 & c & 0 & -s \\ 2sc & 0 & -2sc & 0 & (c^2 - s^2) & 0 \\ 0 & 0 & 0 & -s & 0 & c \end{bmatrix} \quad (3.22)$$

$$[T_\sigma] = \begin{bmatrix} c^2 & 0 & s^2 & 0 & 2sc & 0 \\ 0 & 1 & 0 & 0 & 0 & 0 \\ s^2 & 0 & c^2 & 0 & -2sc & 0 \\ 0 & 0 & 0 & c & 0 & -s \\ -sc & 0 & sc & 0 & (c^2 - s^2) & 0 \\ 0 & 0 & 0 & -s & 0 & c \end{bmatrix} \quad (3.23)$$

with  $c = \cos\theta$  and  $s = \sin\theta$  (adapted from Talbi *et al.* (2009)).

The core's constitutive relation is transformed from the local coordinate system to the global coordinate system as follows:

$$\{\varepsilon\}_{xyz} = [T_\varepsilon] \{\varepsilon\}_{123} = [T_\varepsilon] [C]_{123} \{\sigma\}_{123} = [T_\varepsilon] [C]_{123} [T_\sigma] \{\sigma\}_{xyz} \quad (3.24)$$

The transformed compliance matrix is given by

$$[C]_{xyz} = [T_\varepsilon] [C]_{123} [T_\sigma] \quad (3.25)$$

The 3D material compliance matrix should first be rotated according to Equation 3.25 and then reduced and inverted to obtain the 2D stiffness matrices  $[Q]$  and  $[G]$  (Marek and Garbowski, 2015). The transformed constitutive relations are given by

$$\{\sigma\} = \begin{Bmatrix} \sigma_x \\ \sigma_y \\ \tau_{xy} \end{Bmatrix} = [Q(\theta)] \begin{Bmatrix} \varepsilon_x \\ \varepsilon_y \\ \gamma_{xy} \end{Bmatrix} = \begin{bmatrix} \frac{E_x}{1-\nu_{xy}\nu_{yx}} & \frac{\nu_{xy}E_y}{1-\nu_{xy}\nu_{yx}} & 0 \\ \frac{\nu_{yx}E_x}{1-\nu_{xy}\nu_{yx}} & \frac{E_y}{1-\nu_{xy}\nu_{yx}} & 0 \\ 0 & 0 & G_{xy} \end{bmatrix} \begin{Bmatrix} \varepsilon_x \\ \varepsilon_y \\ \gamma_{xy} \end{Bmatrix} \quad (3.26a)$$

$$\{\sigma_\gamma\} = \begin{Bmatrix} \tau_{xz} \\ \tau_{yz} \end{Bmatrix} = [G(\theta)] \begin{Bmatrix} \gamma_{xz} \\ \gamma_{yz} \end{Bmatrix} = \begin{bmatrix} G_{xz} & 0 \\ 0 & G_{yz} \end{bmatrix} \begin{Bmatrix} \gamma_{xz} \\ \gamma_{yz} \end{Bmatrix} \quad (3.26b)$$

According to Kirchhoff-Love plate theory, the in-plane strains vary linearly through the plate thickness and can be disassembled into midplane (membrane) strains and curvatures:

$$\{\varepsilon\} = \{\varepsilon^0\} + z \{\kappa\} \quad (3.27)$$

Equation 3.27 gives the strains at any distance  $z$  from the midplane (Gibson, 2007). The lamina internal stresses can be expressed using Hooke's Law:

$$\{\sigma\} = [Q(\theta)] (\{\varepsilon^0\} + z\{\kappa\}) \quad (3.28)$$

Static equilibrium is used to relate the midplane strains and curvatures to the internal forces and moments, which are expressed per unit length as

$$N = \int_{-h/2}^{h/2} \{\sigma\} dz = \int_{-h/2}^{h/2} [Q(\theta)] (\{\varepsilon^0\} + z\{\kappa\}) dz \quad (3.29a)$$

$$M = \int_{-h/2}^{h/2} \{\sigma\} z dz = \int_{-h/2}^{h/2} [Q(\theta)] (\{\varepsilon^0\} + z\{\kappa\}) z dz \quad (3.29b)$$

$$T = \int_{-h/2}^{h/2} \{\sigma_\gamma\} dz = \int_{-h/2}^{h/2} [G(\theta)] \{\varepsilon^0\} dz \quad (3.29c)$$

where  $h$  is the panel thickness. The combined system of equations gives the general laminate force-deformation equation:

$$\begin{bmatrix} N \\ M \\ T \end{bmatrix} = \begin{bmatrix} A & B & 0 \\ B & D & 0 \\ 0 & 0 & F \end{bmatrix} \begin{bmatrix} \varepsilon \\ \kappa \\ \gamma \end{bmatrix} \quad (3.30)$$

The extensional stiffness matrix  $[A]$  relates the in-plane normal and shear forces  $\{N\}$  to the midplane strains, and the bending stiffness matrix  $[D]$  relates the bending moments  $\{M\}$  to the curvatures.  $[B]$  couples the in-plane forces with the curvatures, and the moments with the midplane strains (Gibson, 2007). The shear stiffness matrix  $[F]$  relates the transverse shear forces  $\{T\}$  to the transverse shear strains. The  $[ABD]$  matrix is the laminate stiffness matrix (Gibson, 2007; Talbi *et al.*, 2009).

Homogenisation through the core's thickness ( $z$ -direction) gives

$$[A(x)] = \int_{-h/2}^{h/2} [Q] dz = [Q] t_{vc} \quad (3.31a)$$

$$[B(x)] = \int_{-h/2}^{h/2} [Q] z dz = [Q] z_c t_{vc} \quad (3.31b)$$

$$[D(x)] = \int_{-h/2}^{h/2} [Q] z^2 dz = [Q] \left( z_c^2 t_{vc} + \frac{t_{vc}^3}{12} \right) \quad (3.31c)$$

$$[F(x)] = \int_{-h/2}^{h/2} [G] dz = [G] t_{vc} \quad (3.31d)$$

where  $t_c$  is the thickness of the fluting medium (see Figure 3.4) and  $t_{vc} = t_c / \cos\theta$  is the vertical thickness of the corrugated sheet (Talbi *et al.*, 2009).

Homogenisation along the MD ( $x$ -direction) gives

$$[A] = \frac{1}{P} \int_0^P [A(x)] dx \quad (3.32a)$$

$$[B] = \frac{1}{P} \int_0^P [B(x)] dx \quad (3.32b)$$

$$[D] = \frac{1}{P} \int_0^P [D(x)] dx \quad (3.32c)$$

$$[F] = \frac{1}{P} \int_0^P [F(x)] dx \quad (3.32d)$$

### 3.4 Finite element modelling

This section discusses the modelling techniques that were used to develop an FE model of a corrugated paperboard panel and a simplified model with an equivalent homogeneous core. The purpose of materials modelling in this project is to validate the material properties of the homogenised sandwich panel before input into the structural model. MSC Software Corporation's advanced nonlinear FEM solver and pre- and post-processor, Marc and Mentat (MSC Software Corporation, 2019), were used for the finite element analyses in this thesis.

#### 3.4.1 Paperboard characterisation

The methods that were used to determine the nine independent elastic constants of 250KL, 175KL and 150SC paper, were presented in Sections 3.1 and 3.2. The results are summarised in Table 3.3. The material properties in Table 3.3 serve as the foundation of the material models.

Table 3.3: Material properties of the linerboard and fluting medium

	250 KL	175 KL	150SC
$E_1$ (MPa)	6695	8032	4709
$E_2$ (MPa)	2310	2369	2918
$E_3$ (MPa)	35	42	25
$\nu_{12}$	0.50	0.54	0.37
$\nu_{13}$	0.01	0.01	0.01
$\nu_{23}$	0.01	0.01	0.01
$G_{12}$ (MPa)	1522	1688	1435
$G_{13}$ (MPa)	122	146	86
$G_{23}$ (MPa)	66	68	83
Thickness (mm)	0.345	0.243	0.251



used to model a quarter of the simply supported specimen, as illustrated in Figure 3.6.

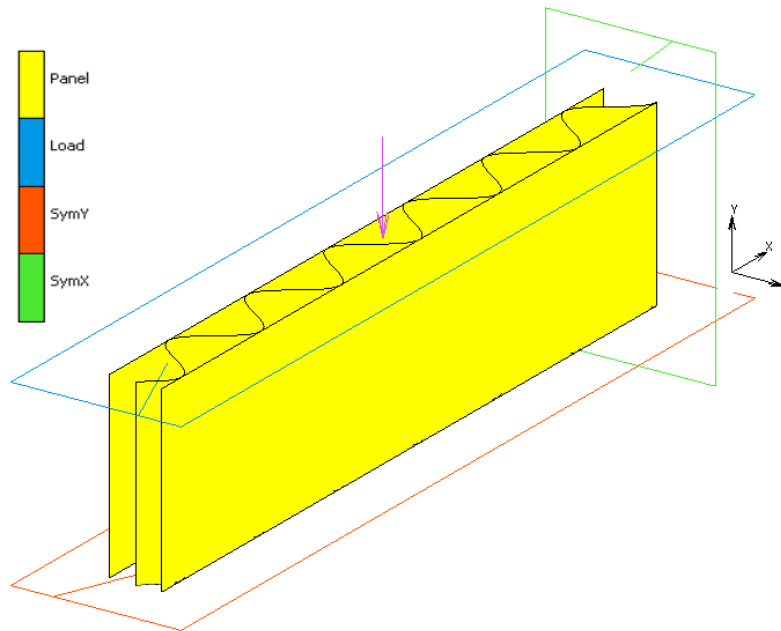


Figure 3.6: Symmetry conditions for the ECT model

The element type selected for this analysis is a four-node, thick-shell element with bilinear shape functions and transverse shear effects. Modelling the wavy shape of the fluting requires a fine mesh. A mesh convergence study was performed based on an eigenvalue buckling analysis. The eigenvalue converged for a 0.5 mm square mesh (for the liners and the fluting). During the corrugation process, a starch adhesive is used to glue the liners to the fluting. As a simplification of the glued contact, the liners and the fluting were connected by sharing the same nodes at the crests of the fluting (Allansson and Svård, 2001).

The material properties should be orientated according to the local coordinate system of the elements. In this case, the local coordinate system of the liner elements corresponds to the global coordinate system of the corrugated panel. The local coordinate system of the fluting elements varies with the wavy shape of the core. An "orientation curve" (MSC Software Corporation, 2019) was used to orientate the material properties of the fluting medium according to each element's local coordinate system.

Symmetry conditions were modelled using the built-in symmetry surfaces in Marc (see Figure 3.6) (MSC Software Corporation, 2019). Load-control of a rigid surface was used to apply a compressive load of 500 N. The elements have six degrees of freedom:  $x$ -,  $y$ - and  $z$ -translation (TX, TY and TZ) and rotation about the  $x$ -,  $y$ - and  $z$ -axes (RX, RY and RZ). Therefore, six rigid body modes of the specimen should be prevented. The symmetry conditions account for five rigid



body modes: TX, TY, RX, RY and RZ. The out-of-plane translation, TZ, was fixed at the loaded edge of the specimen, at the first node from the side that is shared by a liner element and a fluting element. In an ECT, two guide blocks are initially used to ensure that the load is applied perpendicular to the MD of the specimen. The guide blocks were omitted from the model since the symmetry conditions and the additional TZ boundary condition already prevent misalignment of the specimen.

Nonlinear static and buckling analyses were performed with the Large Strain formulation in Marc. In the static analysis, the Full Newton-Raphson iterative procedure was used, and the load was applied incrementally using a multi-criteria adaptive stepping procedure. The nonlinear buckling analysis followed, in which the incremental stiffness matrices are used to predict the collapse load of the structure. The predicted ECT value is 7.7 kN/m, which differs from the measured ECT value (7.2 kN/m) with 6.9%. The standard deviation of the measured ECT values is 4.2%. Biancolini and Brutti (2003), however, reported standard deviations of up to 6.5% for C-flute ECT specimens. Given the reported and measured standard deviations, the ECT model predicted the edge compression strength of the C-flute board with reasonable accuracy. In the experimental ECT, local buckling occurs at the loaded edge of the liners. The first buckling mode (see Figure 3.7) shows local buckling of one of the liners at the free vertical edge. Higher-order mode shapes showed local buckling of the liners at the loaded edge. Biancolini and Brutti (2003) reported a similar first buckling shape for their C-flute ECT model.

Since the first buckling mode shape is dominated by the collapse of the liner-board, the ECT model cannot be compared to a simplified model in which the liners are laminated to a homogeneous core. For this reason, a 400 mm × 400 mm simply supported panel with constrained TZ at the panel edges, as in Nordstrand (1995) and Allansson and Svård (2001), was modelled. The symmetry conditions in Figure 3.8 were used to model a quarter of the panel. A mesh convergence study, as for the ECT model, gave an acceptable mesh size of 2 mm. A compressive load of 1000 N was applied (incrementally) to the top edge of the panel through load control of a rigid surface, and nonlinear static and buckling analyses were performed.

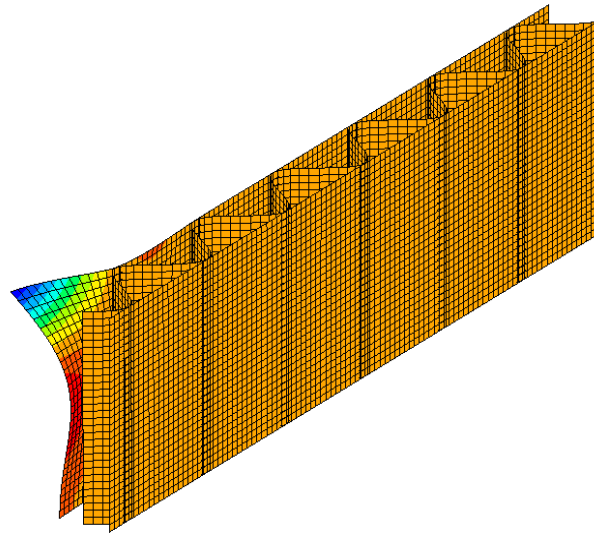


Figure 3.7: First buckling mode of the detailed ECT model

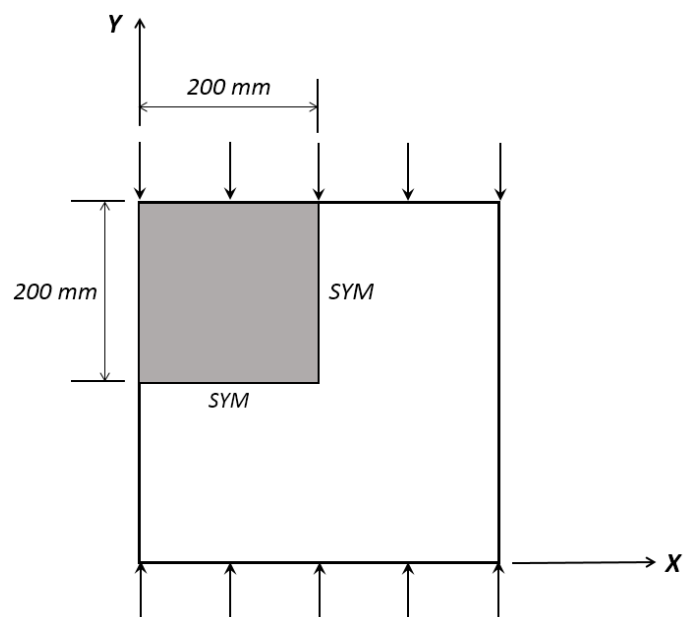


Figure 3.8: Symmetry conditions for the model of a 400 mm × 400 mm corrugated paperboard panel

The predicted collapse load of the panel is 1395 N. Figure 3.9 illustrates the most-likely buckling shape (and the global out-of-plane displacement at the collapse load). The maximum out-of-plane displacement at the collapse load is 5.93  $\mu\text{m}$ , which is less than 1% of the panel thickness.

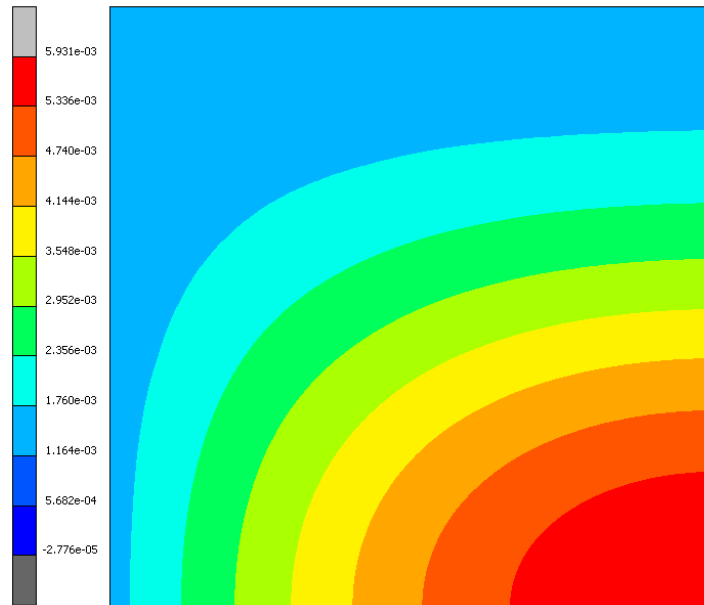


Figure 3.9: First buckling mode of the 400 mm  $\times$  400 mm detailed model and out-of-plane displacement response at 1395 N

The next section discusses the simplified model. The collapse load and the global out-of-plane displacement (at the collapse load) is compared to that of the detailed panel, and the effect of an initial imperfection on the model's out-of-plane displacement is investigated. Two element types are compared: 4-node thick-shells with transverse shear effects and 8-node solid-shells (or brick elements) with a parabolic transverse shear distribution and selective reduced integration (MSC Software Corporation, 2019). Solid-shell elements are considered for the telescopic structural model for their enhanced capabilities when modelling double-sided contact (Alves de Sousa *et al.*, 2007; MSC Software Corporation, 2019).

### 3.4.3 Simplified model

The simplified panel was modelled as a composite laminate with a homogeneous core, as illustrated in Figure 3.10. The material properties of the laminate were defined using Marc's composite formulation. The outer layers were given the orthotropic material properties of 250KL paper (from Table 3.3), and the Tsai-Wu failure criterion was activated for failure estimation of the liners. The tensile- and compression strengths in Table 3.2 and Equations 3.13 and 3.14 were used to describe the Tsai-Wu failure criterion in Marc. The material properties of the homogeneous C-flute core are given in Table 3.4. The material orientation corresponds to the global coordinate system where the MD is parallel to the  $x$ -direction.

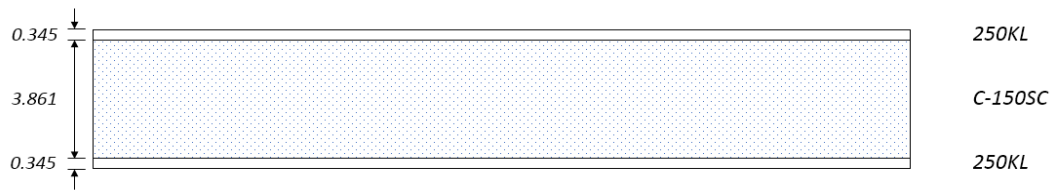


Figure 3.10: Composite laminate profile for the simplified material model

A 400 mm  $\times$  400 mm simply supported panel was modelled with the symmetry conditions in Figure 3.8 and TZ constrained at the panel edges. A compressive load of 1000 N was applied (incrementally), as in the detailed panel model. Two element types were investigated: four-node thick-shell elements with transverse shear effects and 8-node solid-shells with a parabolic transverse shear distribution. A mesh convergence study was performed for both element types, using an eigenvalue buckling analysis. For both element types, the eigenvalue converged for a 2 mm square mesh. The nonlinear static and buckling analyses were set up and executed as for the detailed models.

The collapse load of the simplified shell model is 1346 N, which is 3.5% less than the predicted collapse load of the detailed model. The maximum global out-of-plane displacement at the collapse load is 0.66  $\mu\text{m}$ , as shown in Figure 3.11.

In the solid-shell model, rotation of the rigid (load-applying) surface was allowed about the  $x$ -axis to represent the boundary conditions in the thick-shell model (where the nodes at the loaded edge are free to rotate about the  $x$ -axis). The collapse load of the solid-shell model is 1426 N, which is 2.2% larger than the predicted collapse load of the detailed panel. The first buckling mode shape and out-of-plane displacement response (Figure 3.12) corresponds to the buckling modes in Figures 3.9 and 3.11. The maximum out-of-plane displacement at the collapse load is 0.03 mm.

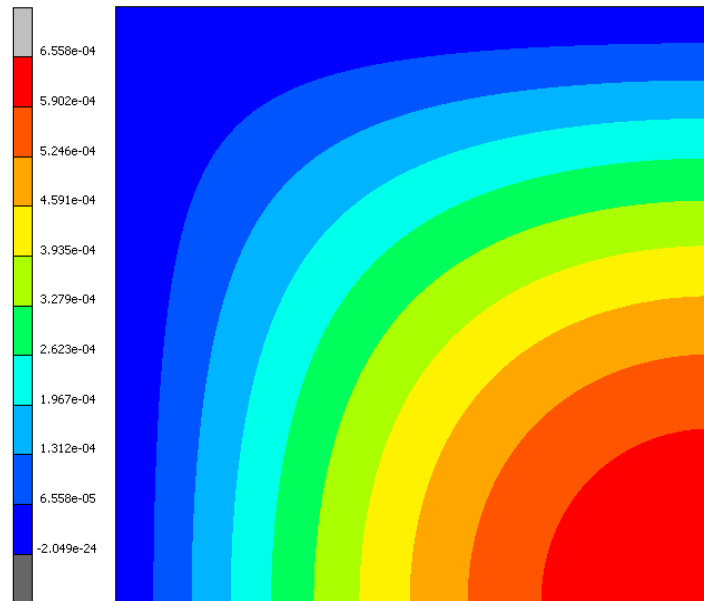


Figure 3.11: First buckling mode of the simplified shell model and out-of-plane displacement response at 1346 N

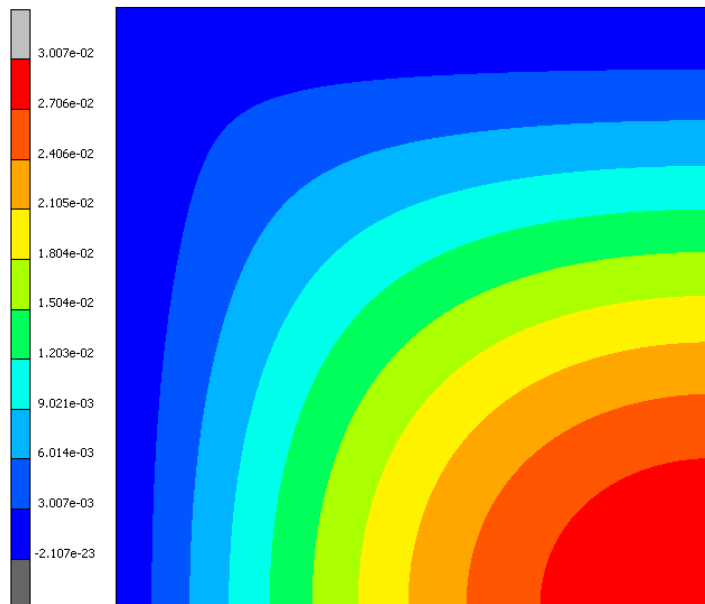


Figure 3.12: First buckling mode of the simplified solid-shell model and out-of-plane displacement response at 1426 N

The FE models predicted near-zero out-of-plane deformation at the collapse load, which is potentially a result of the absence of geometric imperfections. A

geometric imperfection was imposed in the simplified models to initiate deformation of the panels into the buckling mode of interest (Nordstrand, 1995). The imperfection was modelled as a bulge with an amplitude of 0.1 mm at the panel centre.

The buckling mode and the collapse load of the simplified models were not significantly affected by an initial geometric imperfection of 0.1 mm. The maximum out-of-plane displacement, however, increased from 0.66  $\mu\text{m}$  to 3.77 mm in the shell-model and from 0.03 mm to 3.11 mm in the solid-shell model, as illustrated in Figures 3.13 and 3.14.

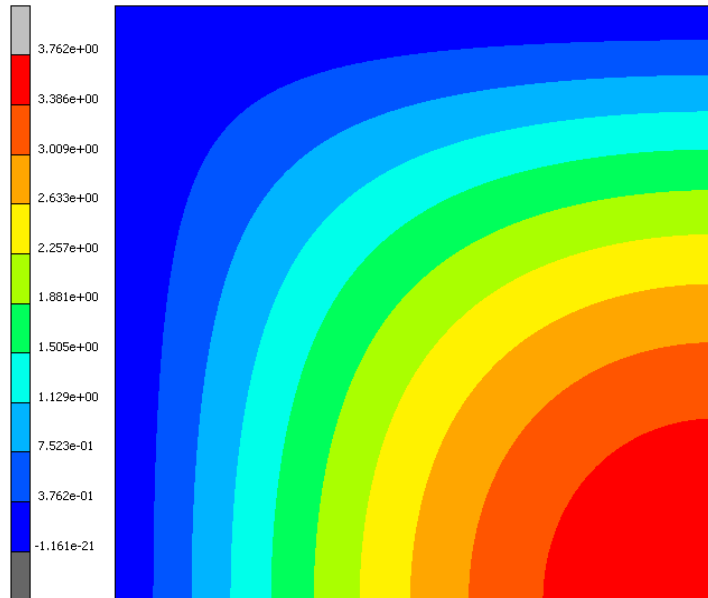


Figure 3.13: Global out-of-plane displacement at the collapse load of the geometrically imperfect thick-shell model

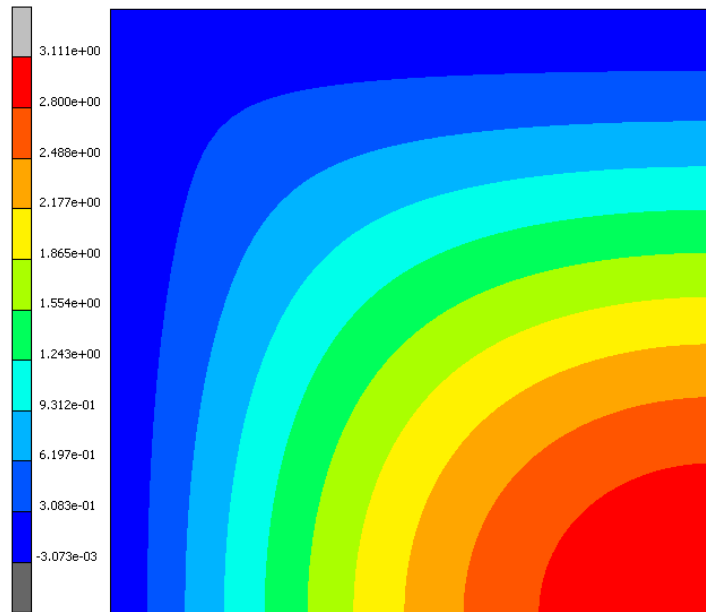


Figure 3.14: Global out-of-plane displacement at the collapse load of the geometrically imperfect solid-shell model

Nordstrand (1995) reported that high shear stress gradients exist near the corners of edge-loaded panels with large planar dimensions compared to their thickness and, therefore, failure would initiate in the corner regions. Figure 3.15 illustrates that, for the detailed model and the geometrically imperfect simplified models, the corner regions of the panels are subject to the highest shear strain. The solid-shell model has a shear strain distribution closer to that of the detailed model. The shell model has a symmetric shear strain distribution, with the highest values located at its corners.

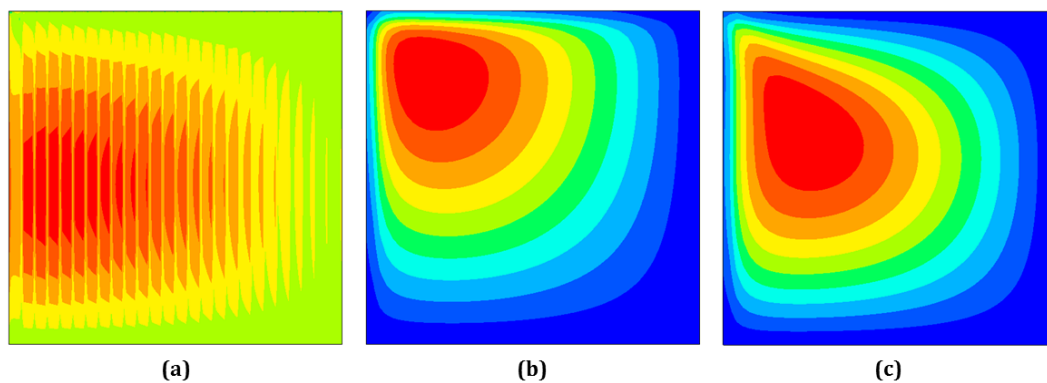


Figure 3.15: In-plane shear strain at the collapse load of (a) the quarter-symmetry detailed model, (b) the geometrically imperfect thick-shell model, and (c) the geometrically imperfect solid-shell model

### 3.5 Summary

The materials modelling section shows that: the material properties of 250KL and 150SC paper when used in an ECT model, predicts the experimental ECT value with reasonable accuracy. The simplified (homogeneous) model predicts the collapse load of the detailed model with good accuracy when 4-node thick-shell elements are used and when solid-shells are used. And, a small initial geometric imperfection is necessary for the panels to exhibit out-of-plane displacement.



## Chapter 4

# Box compression test experimental study

This chapter presents the experimental methods that were used to investigate the structural behaviour of the Mk 4 carton under a compressive load. The findings from this section of the project will be used to validate the finite element model of the carton. The most common method for measuring the compression strength of a corrugated paperboard carton is the BCT. This test method will, therefore, serve as the foundation of the structural finite element model.

### 4.1 Friction coefficients

As discussed in Section 2.2.2.1, the BCT involves the top-to-bottom compression of a carton between two flat platens. In the structural FE model, the friction coefficient between the platens and the carton is necessary when modelling the contact between the two surfaces. This section discusses the experimental procedure that was used to determine the friction coefficient between corrugated paperboard and an aluminium surface, which is the material used for the platens in the BCT.

The corrugation process causes one side of the corrugated board to have a ripple pattern on the surface. The rippled surface is usually on the inside of the carton since the smooth side is preferred for printing purposes. The friction coefficient was, however, measured for both sides of the corrugated board in the MD and CD.

In this experiment, a 100 mm × 100 mm sample of corrugated paperboard is kept stationary on top of a rotating aluminium disk. The sample is glued to a particleboard block of the same dimensions so that a load cell can be attached to the block, as shown in Figure 4.1. The load cell measures the shear force between the sample and the rotating disk, which was initiated by placing weighted plates on top of the sample and then starting the rotation of the aluminium disk. The disk rotated at an angular velocity of 0.8 rpm, and the corrugated paperboard samples

were positioned approximately 160 mm from the centre point of the disk. This resulted in a translational velocity of approximately 13.4 mm/s at the contact.

Four normal forces were applied using weight plates of 5 kg, 10 kg, 15 kg and 30 kg, respectively. The resulting shear force was measured for each weight increment to obtain four different shear force versus time graphs. The static shear force is the peak force on the shear force versus time graph, and the dynamic shear force is the average of the shear force recordings after the peak force. An example of a shear force versus time graph is given in Figure 4.2.

A sample size of 10 specimens was used for this experiment. Three groups of samples were tested for each board type (B- and C-flute) to measure the shear force in the MD and CD of the rippled side and the shear force in the MD of the smooth side. A linear curve fit was applied to the shear force versus normal force data, where the friction coefficient is defined as the slope of the curve. An example of the curve fit is illustrated in Figure 4.3. The results are summarised in Table 4.1, where  $\mu_s$  and  $\mu_k$  are the static and dynamic friction coefficients, respectively. The standard deviations are small, which indicates good repeatability in the data. The difference between the static- and dynamic friction coefficients of the MD and CD specimens and the C-flute and B-flute specimens is small. For practical purposes, a static friction coefficient of 0.19 will be used in the FE model.



Figure 4.1: Friction coefficient experimental setup

Table 4.1: Measured static and dynamic friction coefficients

Sample type	$\mu_s$	$\mu_k$
C-flute, textured, MD	$0.202 \pm 0.009$	$0.167 \pm 0.011$
B-flute, textured, MD	$0.205 \pm 0.013$	$0.167 \pm 0.008$
C-flute, textured, CD	$0.193 \pm 0.012$	$0.156 \pm 0.006$
B-flute, textured, CD	$0.196 \pm 0.013$	$0.156 \pm 0.006$
C-flute, smooth, MD	$0.189 \pm 0.010$	$0.152 \pm 0.004$
B-flute, smooth, MD	$0.197 \pm 0.009$	$0.157 \pm 0.003$

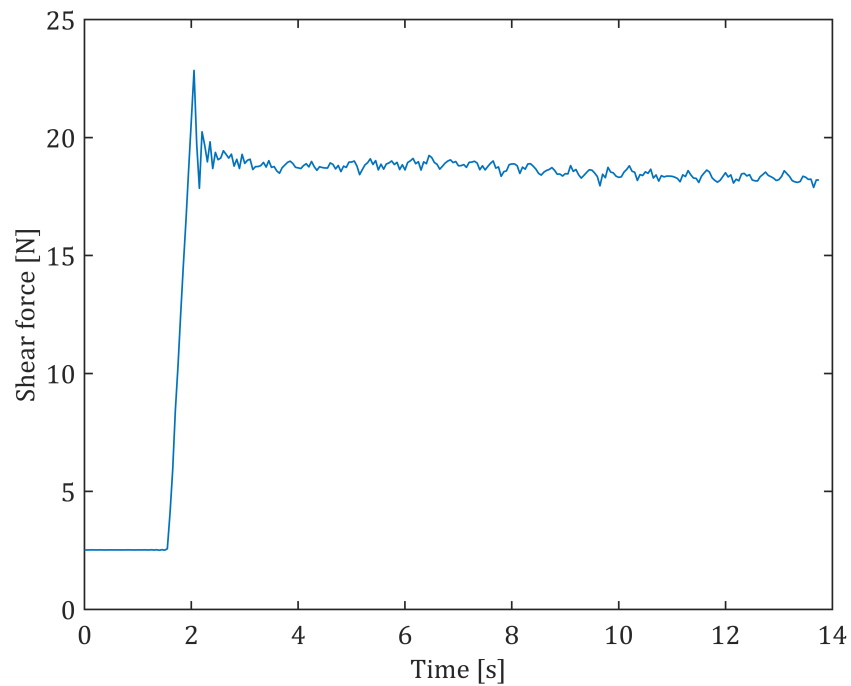


Figure 4.2: Shear force vs. time for a B-flute sample (MD textured side) at the 15 kg weight increment

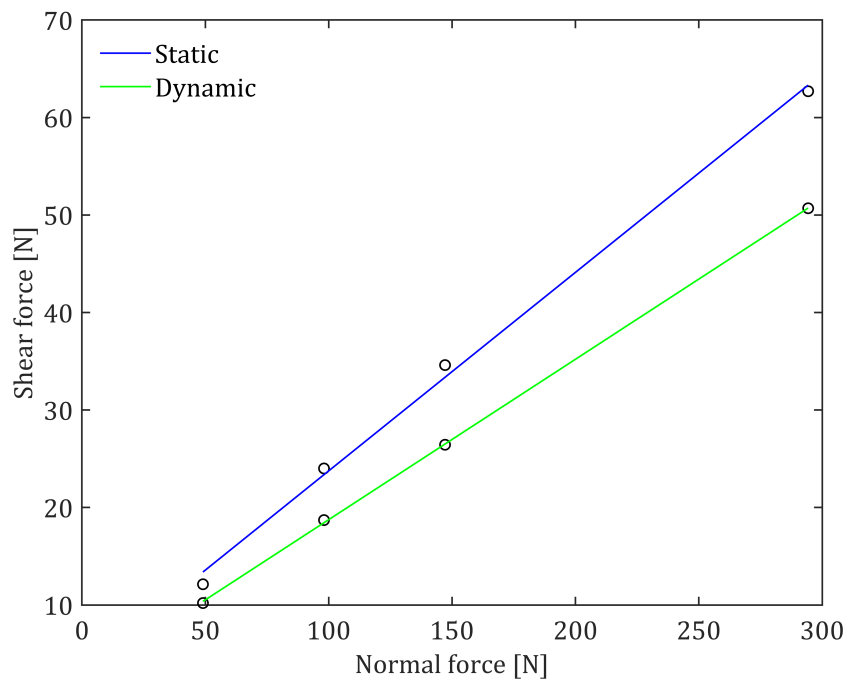


Figure 4.3: Linear curve fit applied to shear force vs. normal force data

## 4.2 Boundary conditions experiment

The misrepresentation of boundary conditions can have a major impact on the computational results of a finite element model (Cook *et al.*, 2002). Researchers have reported many different approaches for modelling the boundary conditions of a BCT. Fadiji (2019) investigated three boundary condition cases. The first case involved fixing the base of the carton in all the degrees of freedom and allowing only vertical displacement and rotation (about the parallel axis) at the top edges. The author used a surface pressure to apply a compressive load to the top of the carton. In the second case, the rotational degrees of freedom were fixed for the entire base and translations were fixed only at the centre nodes. The boundary conditions for the top of the carton were kept the same as in the first case. The third case involved the use of rigid bodies to model the platens of the compression tester. The author used glued contact between the carton and the bottom platen and displacement-control of the top platen to apply a compressive load. Nordstrand (2003) modelled a carton with quarter-symmetry conditions. The author fixed the out-of-plane translations of the horizontal edges, as well as the vertical translations of the bottom edges.

An experimental study was carried out to investigate the effect of different boundary conditions on the compression strength and displacement behaviour of the Mk 4 carton. The setup included a Lansmont compression tester and a clamping fixture that was designed to replicate boundary conditions typically

used in FE models that simulate box compression tests. The clamp uses two aluminium plates that are placed on either side of the carton's base (or top), and bolted together. The first (smaller) plate fits inside the Mk 4 carton, which is placed on top of the second plate. The outer plate has threaded holes for the bolted connections. This setup fixes the vertical and horizontal translations and the rotations of the bottom of the carton or, when fastened to the top of the carton, forces the entire top surface to displace with the same vertical displacement as the crosshead (and prevents any horizontal displacements at the top surface). The clamp has 30 mm × 15 mm angle iron fixtures that can be slotted in on either side of the carton's vertical walls to fix the out-of-plane displacements and rotations at the horizontal edges (see Figure 4.4). The clamping fixture was used to replicate three boundary condition test cases. A fourth case was investigated in which the inner and outer cartons were glued together with contact adhesive.

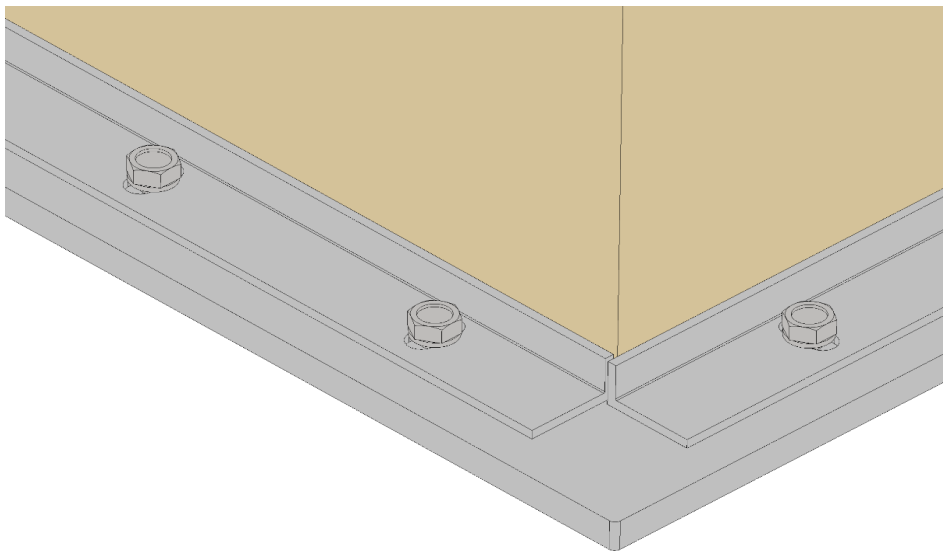


Figure 4.4: Clamping fixture for the BCT boundary condition experiments

All box compression tests were carried out according to the ASTM D642 practice (fixed platen), on standard Mk 4 cartons without vent holes. Cartons were conditioned for 48 hours at 23 °C and 50% RH before testing. A preload of 222 N was applied, and the crosshead displacement of the box compression tester was set to 12.7 mm/min. Tests were set to terminate when the load supported by the carton has reduced by 20% of the peak load. Ten Mk 4 cartons were tested to determine the repeatability of results. The results in Figure 4.5 indicate good repeatability, with a standard deviation of 3% for the peak load and 10% for the displacement at the peak load. With repeatability established, the discussion of the results that follows refers to the load-displacement response of one representative sample from each test case. The average peak load and average displacement at the peak load of the different test cases are provided in Appendix B.

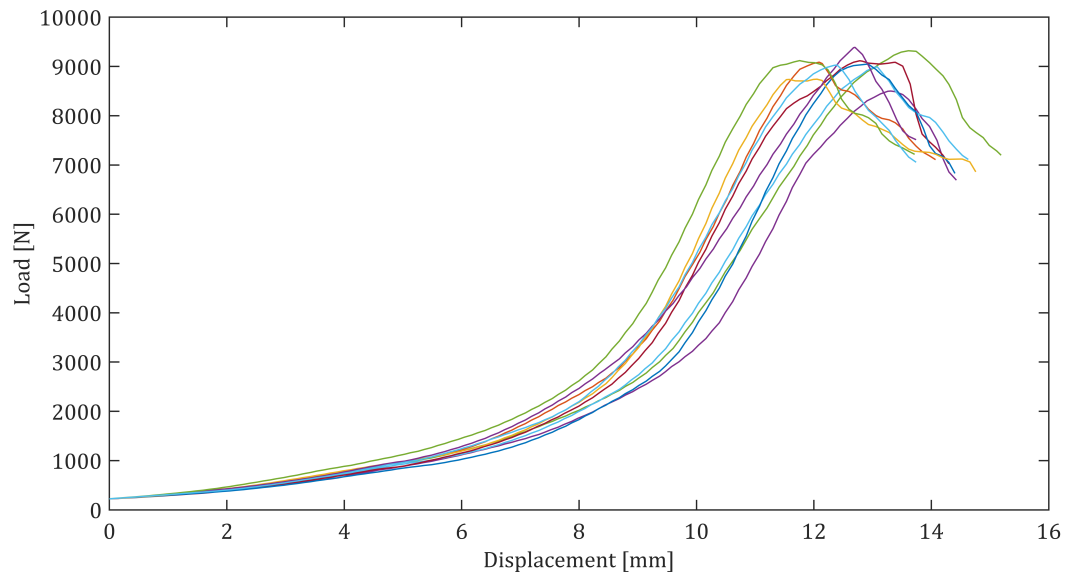


Figure 4.5: BCT results for ten Mk 4 cartons

In Figure 4.6, the load-displacement response is given for the inner, outer, assembled Mk 4, and the glued assembly. The outer carton has the lowest compression strength at 3941 N, while the inner has a compression strength of 4594 N. The lower compression strength of the outer agrees with expectations since it is made from B-flute board, which has a lower top-to-bottom compression strength than the C-flute board of the inner. The compression strength of the assembled Mk 4 (i.e. the telescopic carton) is 9049 N. The compression strength of the glued assembly is only 7% higher at 9697 N, but the vertical displacement is 33% more than the 12.9 mm vertical displacement of the standard telescopic carton. The shape of the displacement path is also quite different from that of the standard Mk 4. Perfect glued contact, as in an FE model, could have a more significant effect on the compression strength since some separation of the glue was observed during experiments.

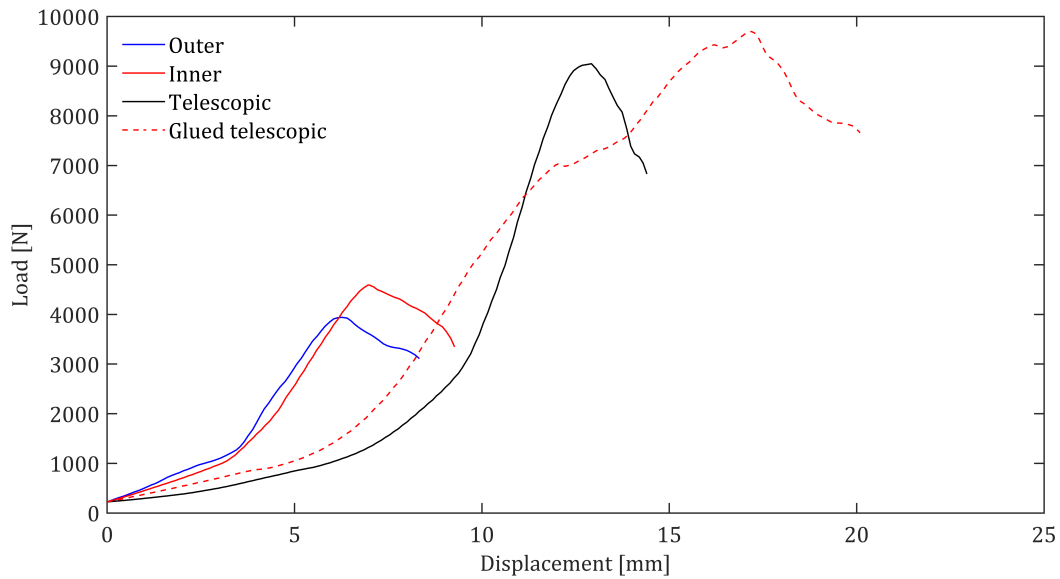


Figure 4.6: BCT load-displacement response of the Mk 4 inner, outer, assembly and glued assembly

The clamping fixture was used to test three boundary condition cases on the Mk 4 telescopic carton: (1) the vertical and horizontal displacements of the base are fixed (red), (2) the top of the carton is kept parallel to the compression platen (i.e. the load is distributed equally over the top surface, and the entire top surface displaces vertically with the crosshead) (blue), and (3) the first two cases are combined (dashed red). Rotation at the horizontal edges was allowed in all three cases. The results are given in Figure 4.7, along with the load-displacement response of a Mk 4 carton that was simply positioned on the platen without additional constraints. The compression strength decreased by 5% in case (1) and by 7% in both the second and third cases. The displacement at the peak load, however, increased by 16%, 26% and 21% for cases (1), (2) and (3), respectively. Figure 4.8 shows a noteworthy observation: delamination damage occurs at the top edges of the inner carton for cases (2) and (3), but more severely for case (3).

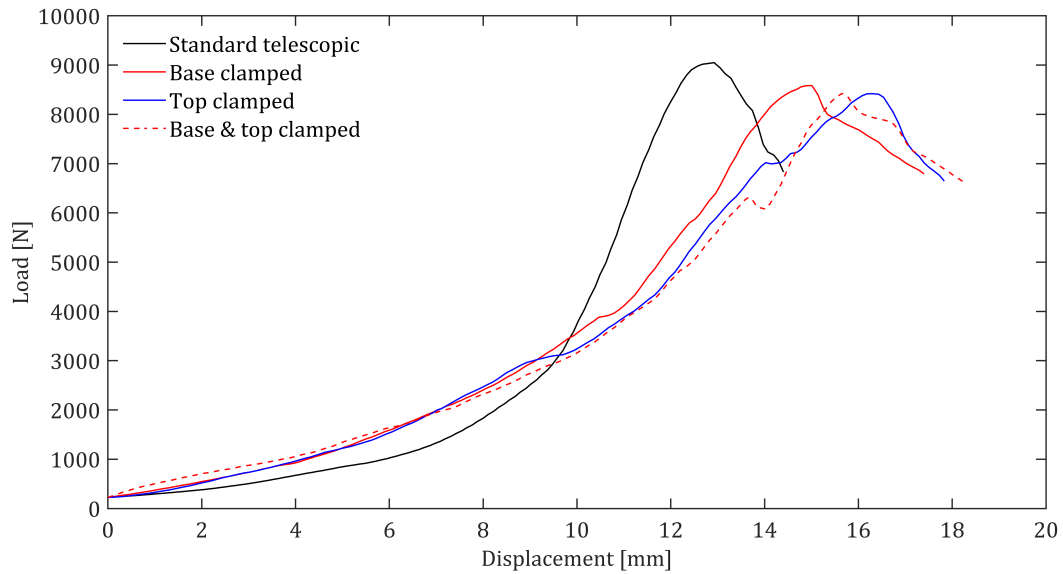


Figure 4.7: BCT load-displacement response of the Mk 4 telescopic carton and three boundary condition test cases



Figure 4.8: Delamination damage of the Mk 4 telescopic carton observed in boundary condition test case (3)

Figure 4.9 shows the load-displacement response of the Mk 4 inner for two boundary condition test cases: (1) fixed vertical and horizontal translations at the base (red), and (2) fixed vertical and horizontal translations at the base and fixed rotation at the bottom edges (blue). The initial slope of the load-displacement curve is steeper than that of the standard BCT for both cases. In case (1), the



magnitude of the peak load and the displacement at the peak load were not significantly affected. In case (2), however, the peak load increased by 15% and the vertical displacement at the peak load decreased by 12%.

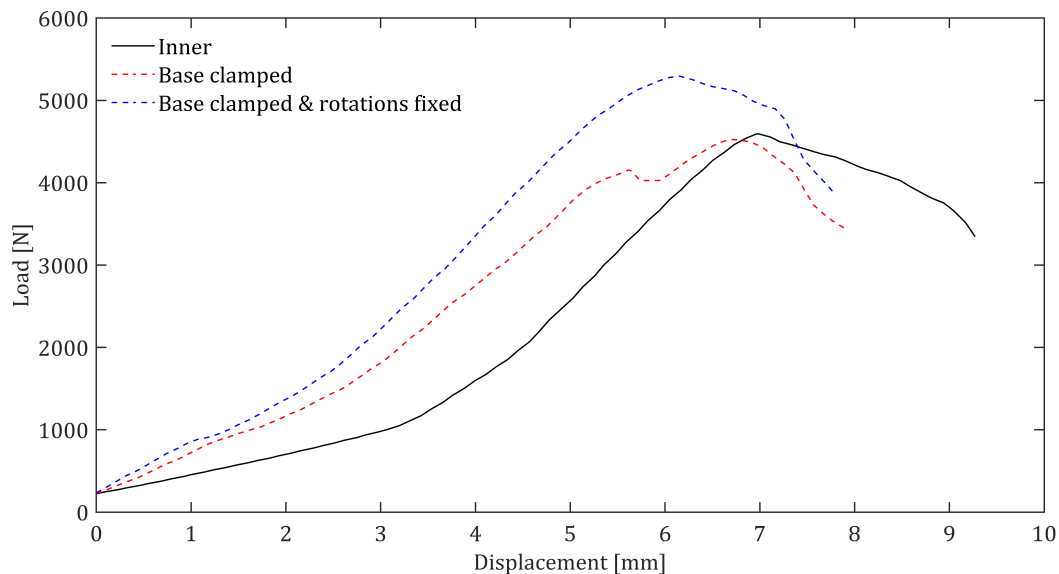


Figure 4.9: BCT load-displacement response of the Mk 4 inner and two boundary condition test cases

This experimental study demonstrates that the load-displacement response of the Mk 4 carton is significantly affected when boundary conditions constrain certain degrees of freedom that are free during standard box compression tests. Therefore, boundary conditions in the FE models should be applied realistically to obtain accurate results. The next section discusses an experiment in which the pressure distribution across the bottom of the carton is mapped using a Tekscan sensor.

### 4.3 Tekscan pressure mapping

The interface pressure distribution between the Mk 4 carton and the bottom platen of the compression tester was measured using a Tekscan pressure mapping sensor. The available sensor model is the I-Scan 5315 sensor, which has a sensing area of 487.7 mm × 426.7 mm. The bottom of the Mk 4 is slightly larger in width, at 495 mm. Therefore, the pressure distribution across one half of the carton was measured. The 5315-sensor model has a 48 × 42 sensel grid.

The first part of the experimental procedure involved equilibrating and calibrating the sensor. The purpose of equilibration is to determine the required gain factor for each sensel such that its digital output is the same as the average digital

output of all the loaded sensels. The Tekscan equilibration device uses an inflatable bladder to apply uniform pressure to the sensor, and the I-Scan software determines the gain factors (Tekscan Inc., 2009). The sensor has a pressure range of 41–207 kPa. Meng *et al.* (2007) used a Tekscan sensor to measure the pressure distribution between stacked cartons. The authors reported pressure values as high as 700 kPa, which is out of the range of the available sensor. For this reason, the sensitivity of the sensor was adjusted to the lowest setting (Low-1) to increase the measurable pressure range. The sensor was equilibrated for three pressure points, of which the highest pressure was close to the saturation pressure of the sensor. After equilibration, the sensor was calibrated using the I-Scan software's two-load power-law calibration procedure for applied loads of 4000 N and 8000 N. The equilibrated and calibrated sensor has a saturation pressure of 689 kPa.

Figure 4.10 illustrates the typical pressure distribution across the base of the Mk 4. The frame corresponds to the peak load applied during the BCT. The pressure map indicates that the applied load is concentrated around the edges of the carton, but not symmetrically. The asymmetric load distribution is likely a result of initial geometric imperfections in the carton. The highest pressure regions occurred at the corners.

As a method to check the pressure values measured by the Tekscan sensor, the average pressure of the loaded sensels can be compared to the peak load recorded by the compression tester divided by the fraction of the area under the carton that is loaded. For this specific carton, a peak load of 9090 N was recorded. From the Tekscan data, the average pressure of the 262 loaded sensels is 226 kPa. The BCT peak load divided by the fraction of the area under the carton that is loaded is 266 kPa. A possible reason for the discrepancy between the compression tester and Tekscan measurements is that some of the sensels recorded saturation pressure values (dark red on the colour scale in Figure 4.10). Since the pressure range of the sensor is lower than required, the saturation pressure values do not represent the actual pressure values.

The aim of this experiment was to characterize the pressure distribution between the base of the Mk 4 and the compression tester's platen. The Tekscan sensor was used successfully for this purpose. The experiment showed that the pressure distribution is concentrated around the edges of the carton, and that maximum pressure values were recorded at the corner regions. The results suggest that most of the applied load is carried by the vertical edges of the carton. The inner and outer of the Mk 4 showed similar results when tested individually.

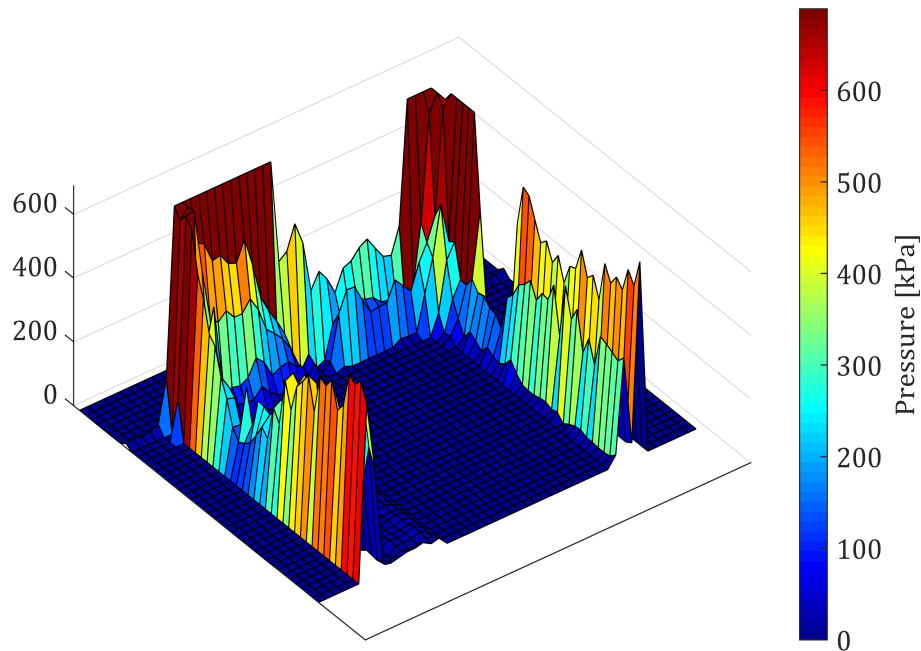


Figure 4.10: BCT pressure distribution across half the base of the Mk 4 telescopic carton

#### 4.4 3D digital image correlation

3D digital image correlation was used to analyse the displacement response of the Mk 4 carton during compression testing. The experimental setup included the Lansmont compression tester and the StrainMaster Portable DIC system with two 5-megapixel CCD cameras and two LED linear lights. The camera spacing and distance to the carton were selected such that the entire front panel of the carton was in focus and could be contained in the field of view. An aperture of  $f/1.6$  was used for both cameras. Matt black spray paint was used to apply a random speckled pattern to the cartons, which had white exterior liners. Five reference images were taken before deformation to determine the DIC displacement errors for two subset sizes. The results in Table 4.2 show similar displacement errors for a 51-pixel and 61-pixel subset size. The 61-pixel subset size was chosen based on its increased speckle density. Compression tests were carried out according to ASTM D642 with a fixed-platen compression tester, as in Section 4.2.

Table 4.2: DIC displacement errors of the two subset sizes considered for the Mk 4 carton

Subset size (pixel)	RMS $\delta x$ (mm)	RMS $\delta y$ (mm)	RMS $\delta z$ (mm)
51	0.0063	0.0047	0.0158
61	0.0063	0.0046	0.0150

The DIC displacement fields of a Mk 4 carton, compressed just past its peak load, are given in Figures 4.11 to 4.13. The edges of the carton were excluded from the DIC calculation to avoid excessive noise in the data. The compression tester did not have an analogue to digital output to which the DIC recordings could be linked. For this reason, the DIC had to be stopped manually just after the peak load was recorded and displayed by the compression tester.

The horizontal and out-of-plane displacement fields in Figure 4.11 and Figure 4.13 show that the side panels of the carton and the front panel buckled inward. The front panel exhibited the largest out-of-plane displacement, with a magnitude of 17.9 mm near the panel centre. Out-of-plane displacements near the vertical edges are small since this is the stiffest region of the carton. Kueh *et al.* (2019) reported similar findings. The authors attributed the maximum out-of-plane displacement at the centre of the panel to a small initial geometric imperfection (or bulge) that increases during the compression test.

The DIC displacement fields of a second Mk 4 specimen are given in Appendix B (Figure B.2). The out-of-plane displacement field shows that the front panel of the carton buckled outward as opposed to the inward buckling observed for the first specimen. The maximum out-of-plane displacement, again, occurred at the centre of the front panel. The displacement field plots of an Mk 4 inner specimen are given in Figure B.3. The inner carton buckled outward with a maximum out-of-plane displacement at the centre region of its front panel.

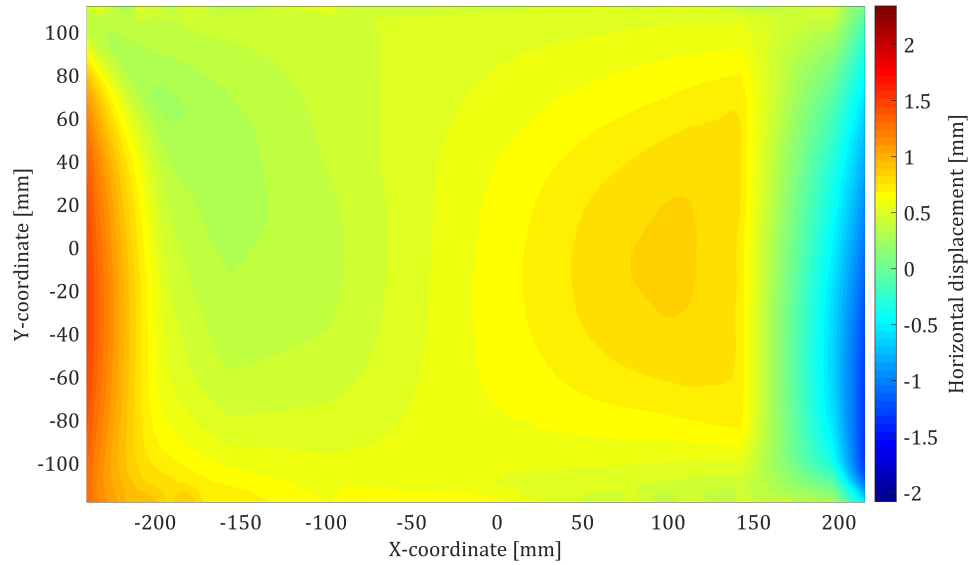


Figure 4.11: DIC horizontal displacement field of the Mk 4 front panel

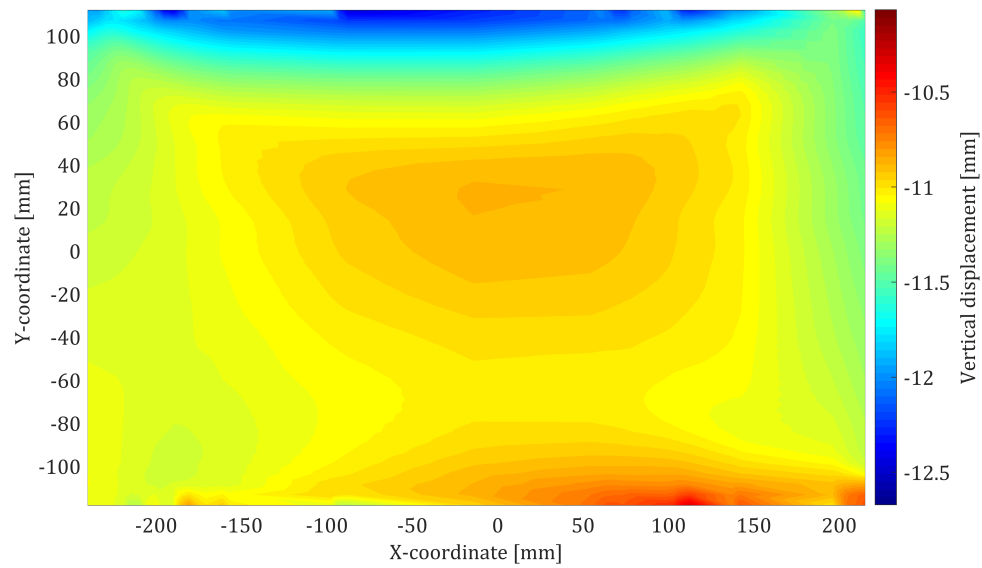


Figure 4.12: DIC vertical displacement field of the Mk 4 front panel

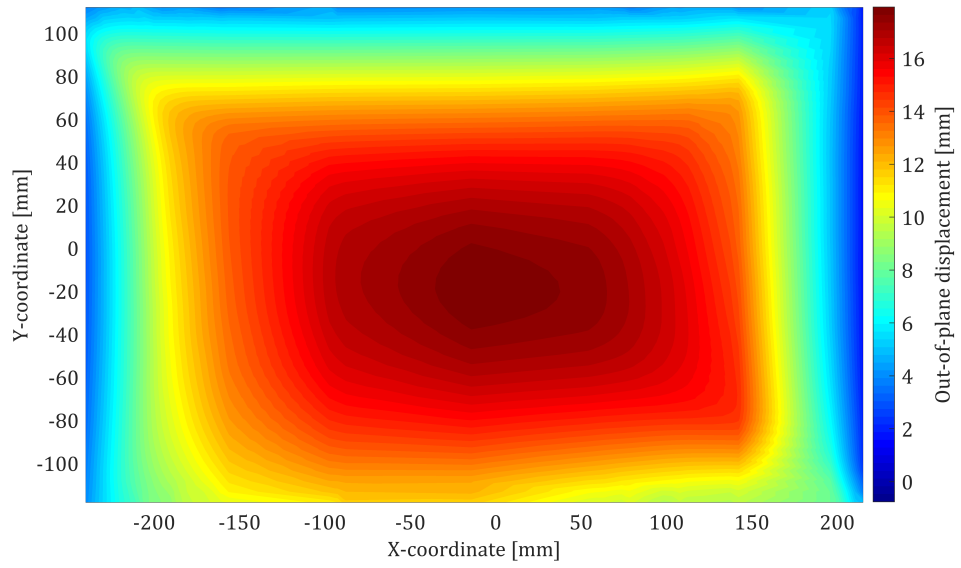


Figure 4.13: DIC out-of-plane displacement field of the Mk 4 front panel

# Chapter 5

## Structural modelling

This chapter discusses the development of the Mk 4 structural FE model. First, the Mk 4 inner was modelled and validated with experimental data. And, the use of thick-shell elements versus solid-shell elements was investigated. Finally, the telescopic Mk 4 was modelled using solid-shell elements and considering the touching contact between the inner and outer cartons. Quarter symmetry conditions were used to reduce the computational costs of the structural models.

### 5.1 Mk 4 inner

This section discusses the FEM procedures that were used to model the Mk 4 inner. The simulated BCT results are compared to experimental BCT data and DIC displacement field data (Figure B.3).

#### 5.1.1 Geometry, boundary conditions, material properties and contact definition

The first part of setting up the structural model involved simplifying and modelling the geometry. It was chosen to test and model the Mk 4 carton without vent holes or slots to reduce further variability in the measured results since additional geometric imperfections may result from the vent hole and slot cutting process. A flat pattern of the Mk 4 outer is given in Figure C.1 as reference for the geometry. The carton was modelled with the quarter-symmetry conditions in Figure 5.1 to reduce computational costs. The score lines (folds) were simplified by connecting the nodes at the panel edges, and the glue lap was omitted from the model since the edge nodes were connected. The flaps at the top and bottom of the carton were reduced to one surface. It was assumed unnecessary to model the extra layer of material where the flaps would overlap since the vertical panels carry most of the compressive load. Mid-surface dimensions were used to model the geometry of the first (4-node, thick-shell) model.

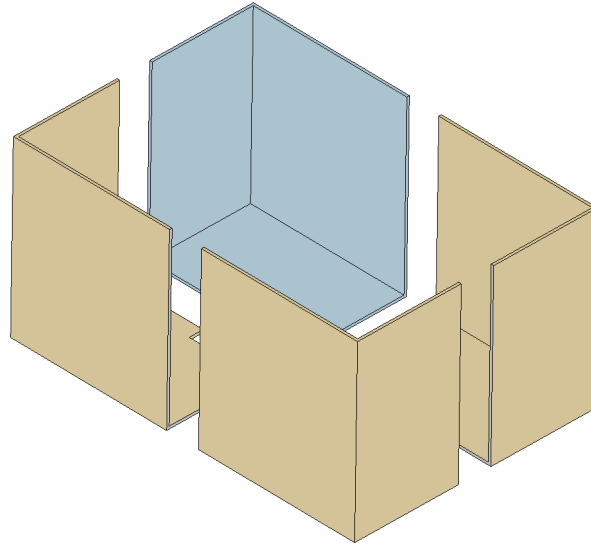


Figure 5.1: Full MK 4 inner and modelled section

Two symmetry surfaces were used to impose the symmetry conditions at the XY and ZY symmetry boundaries, as illustrated in Figure 5.2. A rigid surface was used to model the bottom platen of the compression tester, and a rigid surface with load-control (and later displacement-control) was used to model the top platen. A Coulomb bilinear (isotropic) friction model was used for the touching contact between the carton and the two rigid surfaces. Isotropic friction was selected because the smooth side of the board faces the rigid surfaces. A friction coefficient of 0.19 (as determined in Section 4.1) was specified. No additional boundary conditions are required to prevent rigid body motion since the rigid surfaces account for TY, and the symmetry surfaces and friction model account for all the other degrees of freedom.

The composite laminate formulation in Marc was used to specify the material properties (as for the simplified material model in Section 3.4.3) for C-flute board. The material was orientated such that the CD corresponds to the global  $y$ -direction for the vertical panels. As a simplification of the top and bottom flap layup, the material was orientated uniformly on the top and bottom panels such that the MD corresponds to the global  $x$ -direction and the thickness direction corresponds to the global  $y$ -direction.

Mathematically, contact occurs as a constrained optimisation problem. Contact analysis is complex because it involves accurate tracking of the motion of multiple contact bodies, before and after contact occurs, applying constraints to avoid penetration when contact occurs, and applying the correct boundary condition to simulate friction or heat transfer where necessary (MSC Software Corporation, 2019). In the structural models, the node-to-segment contact algorithm was used. This contact algorithm uses a master-slave relation where the nodes of the touching bodies are the slaves, and the nodes of the touched



segments are the masters (MSC Software Corporation, 2019). The slave nodes cannot penetrate the element faces of the body to which the master nodes are connected. A contact table was used to specify the contact interactions between the meshed, rigid and symmetry bodies. The stress-free projection option in Marc was used for initial contact detection. This option prevents undesired stress changes when a contacting node is forced onto a contacted segment as a result of a small gap or overlap at the start of the analysis (MSC Software Corporation, 2019).

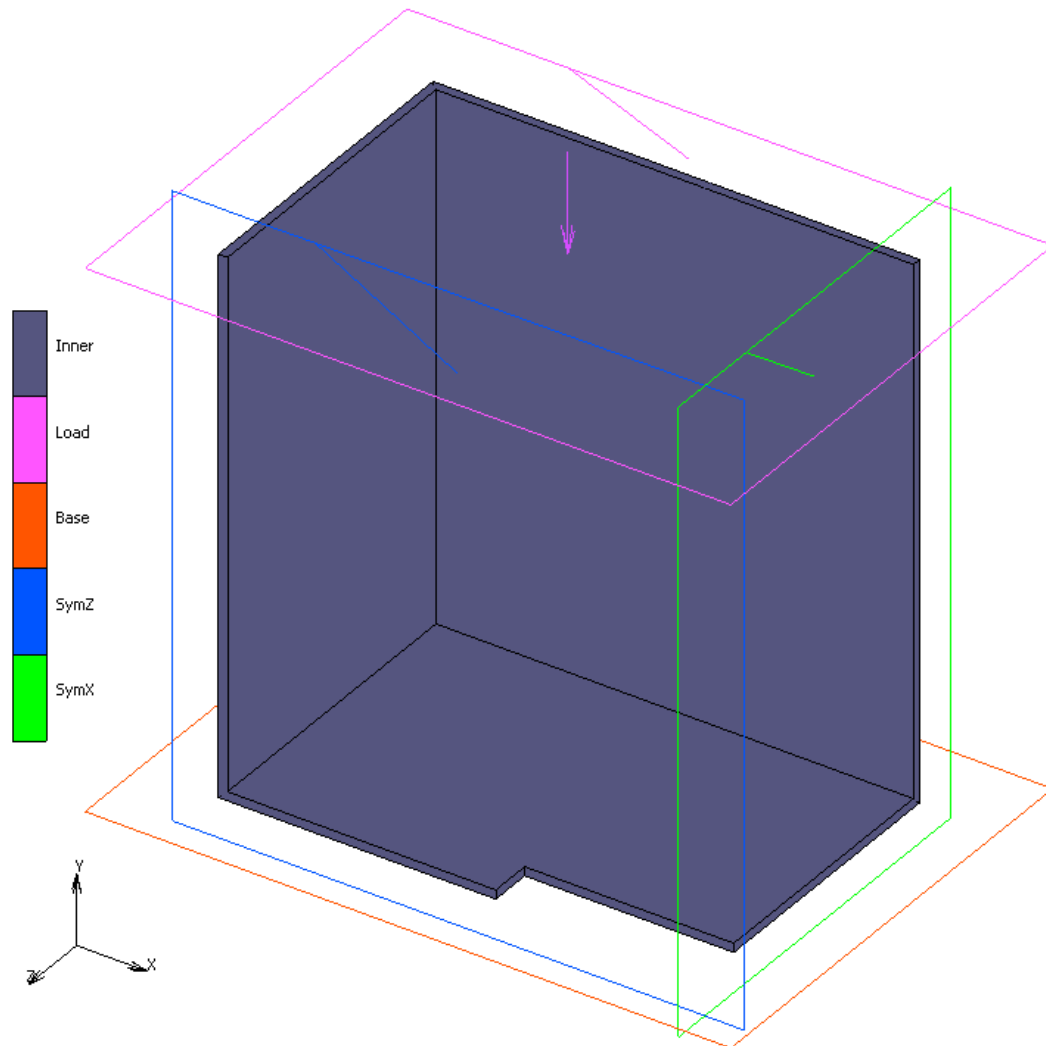


Figure 5.2: FE model of the Mk 4 inner with quarter-symmetry conditions

### 5.1.2 Mesh convergence study, analyses and results

Nonlinear static and buckling analyses were performed using the Large Strain formulation to extract the buckling mode shape and the collapse load of the

structure. The Full Newton-Raphson solution procedure and the default convergence criterion in Marc, residual force checking, were used in the static load case. In residual force checking, the maximum residual load (a measure of the out-of-equilibrium force) is compared to the maximum reaction force (MSC Software Corporation, 2019). The Newton-Raphson iterative procedure minimises the residual.

The mesh size was selected based on the convergence of the collapse load from an eigenvalue buckling analysis. The convergence study was repeated for both models of the Mk 4 inner (i.e. the thick-shell model and the solid-shell model), and the results are illustrated in Figure 5.3 and Figure 5.4, respectively. The magnitude of the collapse load changes with less than 0.2% between the mesh sizes in Figure 5.3, which indicates that the starting mesh (5 mm) of the shell model is already acceptable. The collapse load of the solid-shell model was significantly more sensitive to changes in the mesh size (see Figure 5.4). However, between a 1.5 mm mesh and a 3 mm mesh, the collapse load increased by only 3%. And, between the 3 mm mesh and the 4 mm mesh, the collapse load increased by 2.5%. For this reason, a 3 mm square mesh was chosen for the solid-shell model. The same mesh size was used for the shell model since, as illustrated in Figure 5.3, its collapse load is also convergent for a 3 mm mesh.

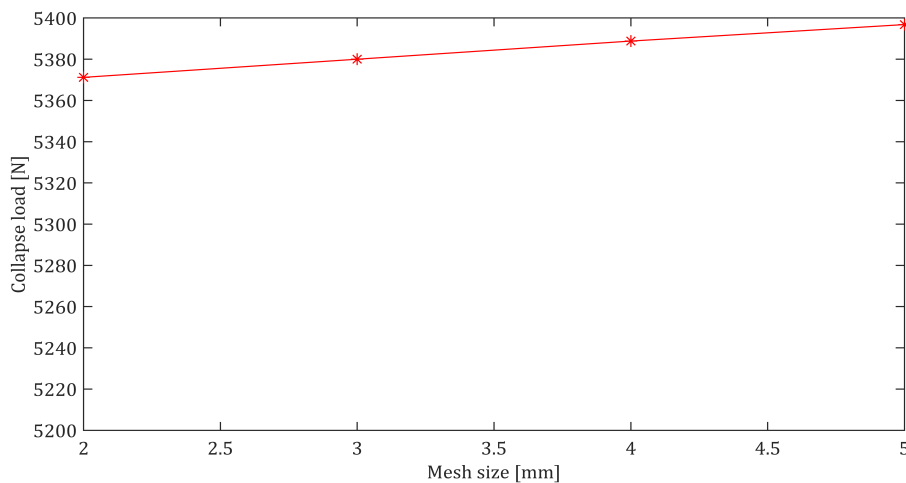


Figure 5.3: Mesh convergence study for the thick-shell Mk 4 inner

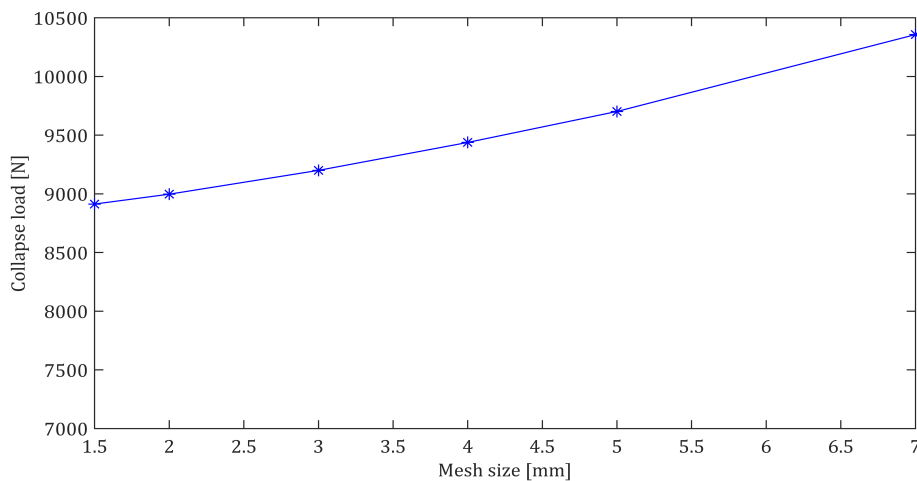


Figure 5.4: Mesh convergence study for the solid-shell Mk 4 inner

In the first static load case, load-control of the top platen was used to apply a compressive load of 4000 N (1000 N for the symmetry model) to the carton. The load was applied incrementally using the multi-criteria adaptive stepping procedure in Marc. The nonlinear buckling analysis followed, which determines the collapse load of the structure and the corresponding buckling mode shape.

The results are given in Table 5.1. The compression strength of the Mk 4 inner, from the BCT results in Table B.1, is 4506 N. The solid-shell model overestimated the collapse load by 104%, while the thick-shell model predicted the collapse load within 3% of the experimental value. The buckling mode shape of each of the two models is given in Figure 5.5. Both buckling mode shapes predict the largest out-of-plane deformations at the centre of the long side of the package, which corresponds to experimental observations and the measured DIC displacement fields (Figure B.3).

The overestimation of the solid-shell model's collapse load is interesting. It was shown in Section 3.4 that the simplified material model is valid for thick-shell and solid-shell elements. The material model is, therefore, not the reason for the discrepancy in the collapse load prediction of the solid-shell model. A plausible reason for the overestimation of the solid-shell model's collapse load is that the rotation of its top edges is constrained. The top edges of the shell model, on the other hand, are free to rotate about the element edges.

Table 5.1: Buckling results of the Mk 4 inner FE models

	Collapse load (N)
Experiments	4506
Thick-shell model	4620
Solid-shell model	9200

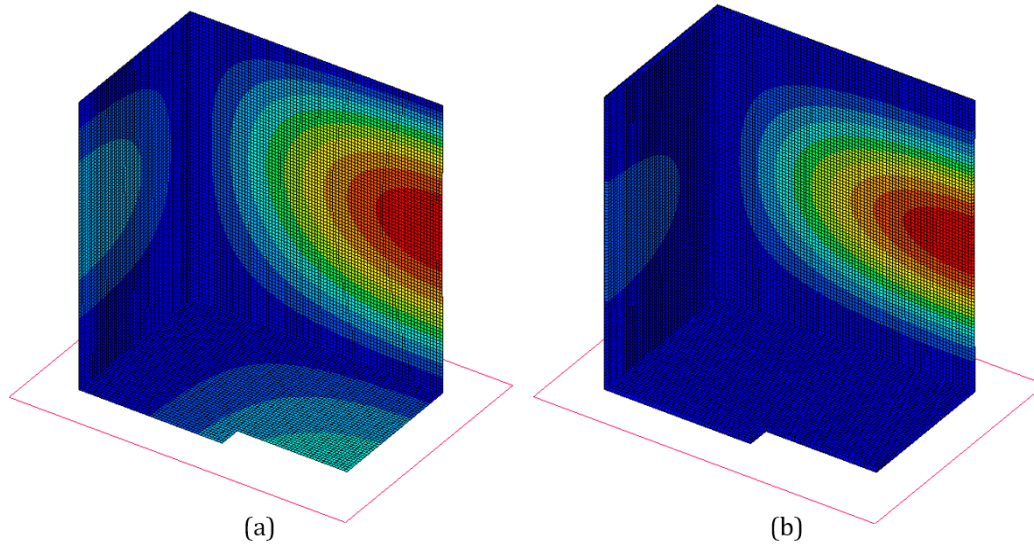


Figure 5.5: First buckling mode shape of the Mk 4 inner (a) thick-shell model and (b) solid-shell model

A second analysis was performed, in which a BCT was simulated through the displacement-control of the top rigid surface. The resulting load-displacement path of the thick-shell model is given in Figure 5.6. A bifurcation point (indicated by a sudden change in the displacement path) occurred at 0.36 mm crosshead displacement and 5992 N load, after which further compressive loads were sustained until failure at 1.72 mm and at 8488 N. A possible reason for the discrepancies in the model's load-displacement response (compared to the experimental load-displacement response in Figure 4.6 and the predicted collapse load) is that the curvature of the vertical panels increases as the load increases and, as a result, the overall panel stiffness increases (Kueh *et al.*, 2012). Imposing a small initial geometric imperfection or a material imperfection could improve the load-displacement response. The solid-shell model showed a different load-displacement response altogether (see Figure 5.7). A limit-point was reached at 0.9 mm crosshead displacement and 11 068 N, after which a sudden instability sets in and the load sustained by the carton decreases. This behaviour resembles nonlinear limit-point buckling (Sun *et al.*, 1995).

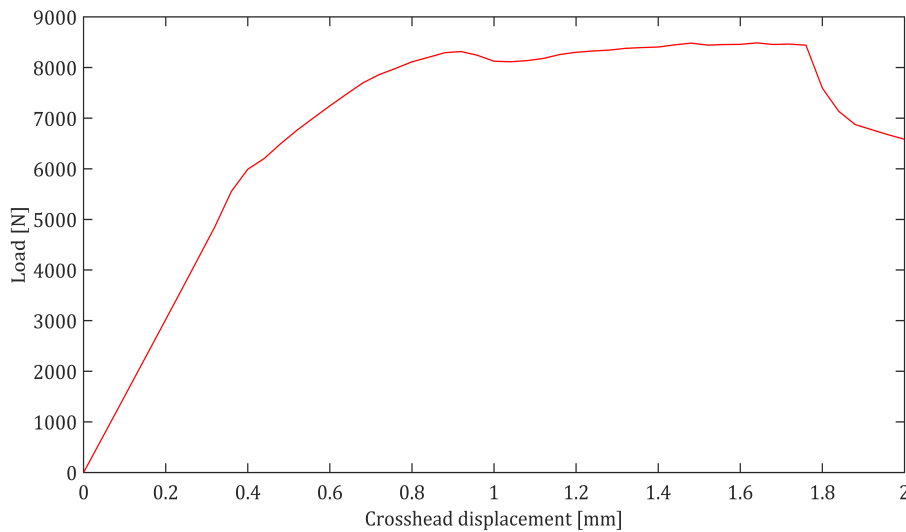


Figure 5.6: Load-displacement response of the Mk 4 inner thick-shell model

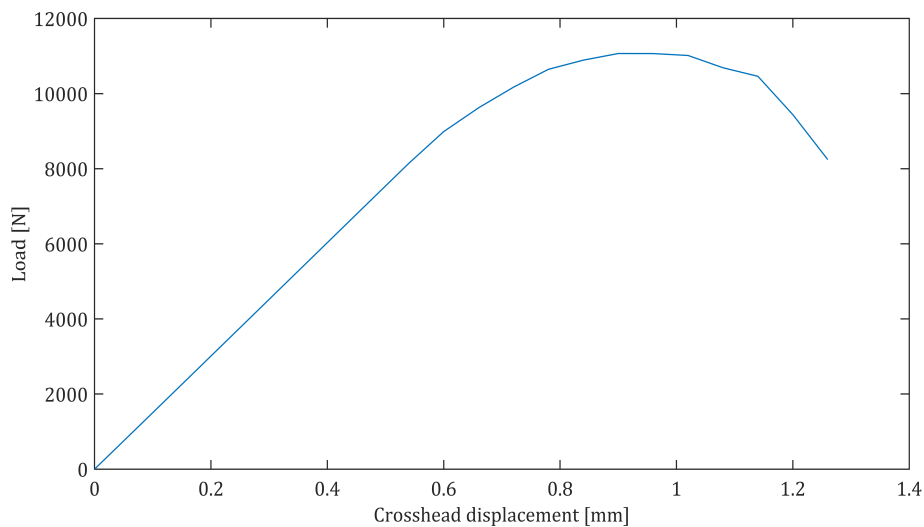


Figure 5.7: Load-displacement response of the Mk 4 inner solid-shell model

The X- and Z displacement fields at the collapse load of the shell model are given in Figure 5.8. The side panel buckled inward with a maximum out-of-plane displacement of 13.5 mm, while the front panel buckled outward with a maximum out-of-plane displacement of 14.8 mm. A similar response is illustrated in the DIC displacement field of the Mk 4 inner in Figure B.3, where the front panel buckled outward with a maximum displacement of 18 mm. The difference between the simulated and the measured out-of-plane displacement response is

18%. Both displacement fields (simulated and measured) indicate that the maximum out-of-plane displacement originates in the centre region of the front (or back) panel.

The solid-shell model's X- and Z displacement fields at its collapse load are given in Figure 5.9. The side panel buckled inward with a maximum displacement of 4.9 mm at the centre of the panel, while the front panel buckled outward with 7.2 mm at the panel centre. The magnitude of the out-of-plane displacements is significantly smaller than that of the thick-shell model. Both the predicted buckling response and the displacement response in the static load case suggest that the solid-shell model overestimates the stiffness of the carton when the load is applied to its edges through a rigid surface.

Figure 5.10 illustrates the propagation of the highest Tsai-Wu failure index (bright red on the colour map) of the outer liner. The highest failure index originates at the centre of the side panel (in the maximum out-of-plane displacement region). As the load increases, the highest failure index propagates towards the corners of the vertical panels until failure (in the final image). Figure 5.11 illustrates the shear strain distribution at the same increments as in Figure 5.10. The highest shear strain region (blue on the colour map) moves from the sides of the vertical edge to the top corner, where material failure occurred. Similar observations were recorded during the BCT experiments, as illustrated in Figure 5.12. The crease lines in the top corners of the side panel correspond to the location where material failure was predicted by the model.

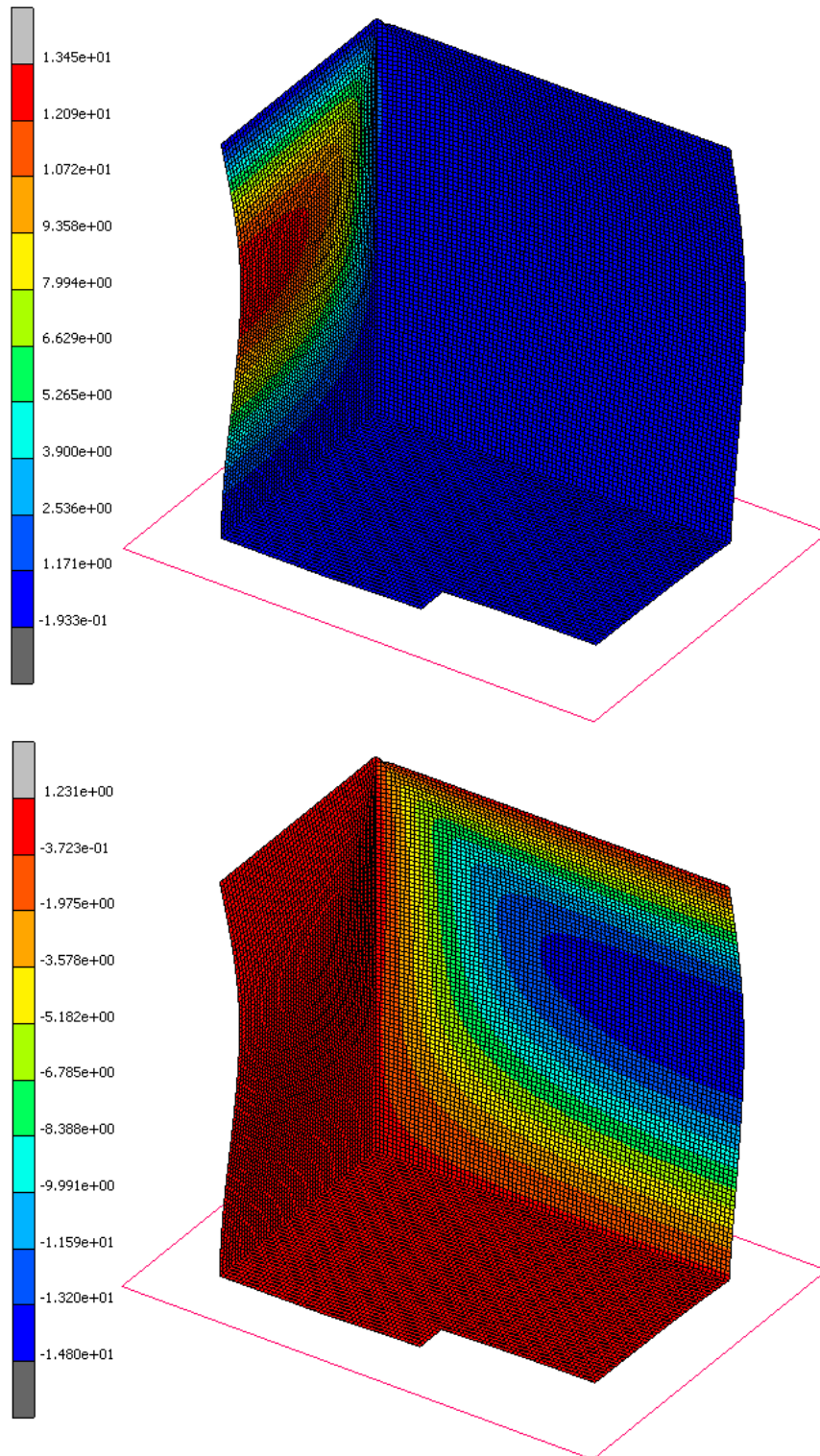


Figure 5.8: X- and Z-displacement plots (top and bottom) of the thick-shell model (Mk 4 inner) for a simulated BCT

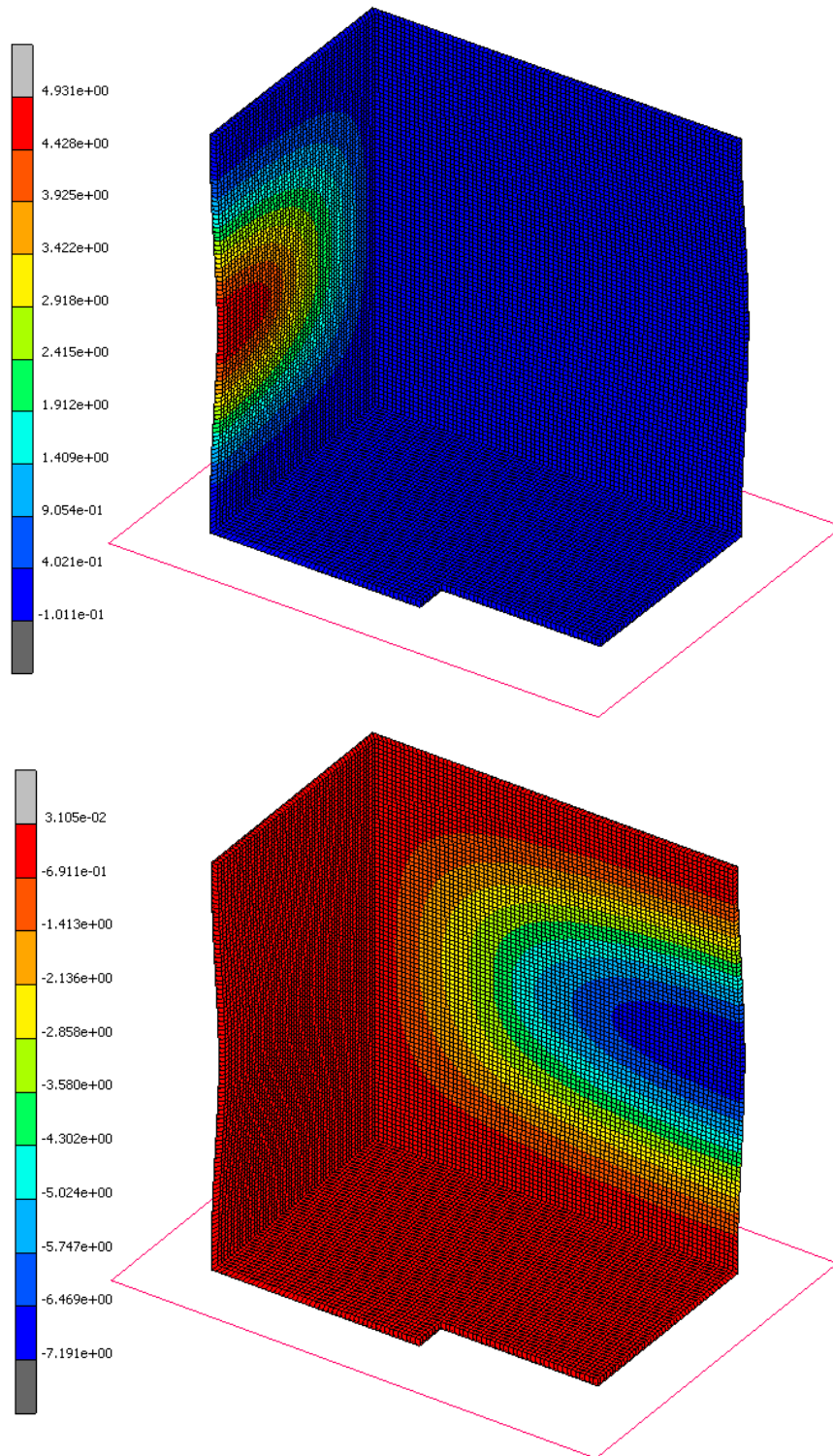


Figure 5.9: X- and Z-displacement plots (top and bottom) of the solid-shell model (Mk 4 inner) for a simulated BCT



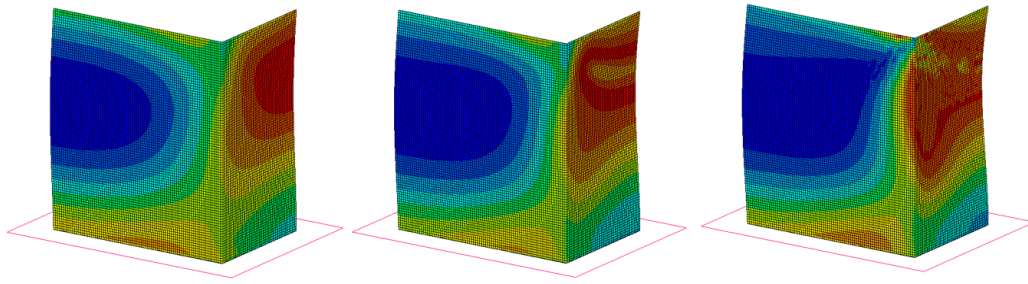


Figure 5.10: Tsai-Wu failure index propagation (left to right) of the outer liner (Mk 4 inner thick-shell model) during the simulated BCT

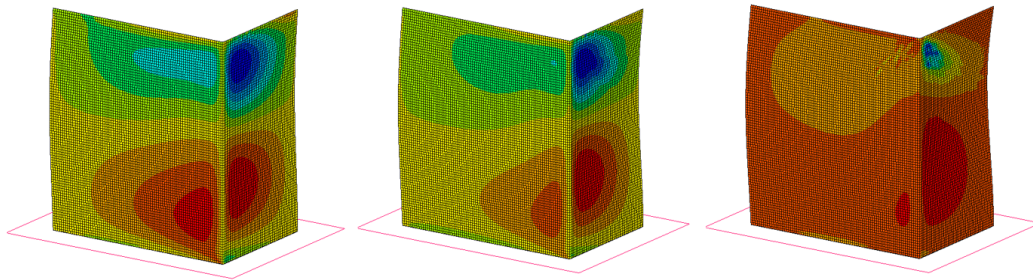


Figure 5.11: Shear strain distribution of the Mk 4 inner (thick-shell model) during the simulated BCT



Figure 5.12: Crease lines in the corners of the Mk 4 inner after compression

### 5.1.3 Summary

In this section, the Mk 4 inner was modelled with quarter-symmetry conditions and four-node thick-shell elements. The model's prediction of the collapse load, out-of-plane displacement response, and material failure location were validated with experimental results. The numerical collapse load is 3% larger than the measured BCT value. The model's out-of-plane displacement response agrees with experimental observations in that the maximum out-of-plane displacement occurs at the centre region of the longer (front/back) panel. The model predicted a maximum out-of-plane displacement 18% smaller than the measured value. The Tsai-Wu failure criterion was used for the failure prediction of the liners. The model predicted that material failure would initiate at the corner regions of the side panels, which agrees with experimental observations.

A second, identical, model was created using solid-shell elements. The solid-shell model overestimates the collapse load by 104% and underestimates the maximum out-of-plane displacement by 60%. But, the buckled shape of the model agrees with experimental observations. The numerical response of the solid-shell model suggests that the stiffness of the carton is overestimated when the load is applied perpendicular to its top edges through a rigid surface. Both models underestimated the vertical displacement of the carton, which is likely due to the absence of geometric or material imperfections. With no geometric imperfections present, the vertical panels can sustain a large amount of membrane strain energy before deforming.

## 5.2 Mk 4 telescopic

This section presents the FEM procedures that were used to model the Mk 4 telescopic carton. The results from a simulated BCT are discussed and compared to experimental BCT data.

### 5.2.1 Pre-processing

The telescopic carton has two components, a C-flute inner and a B-flute outer. The telescopic model setup is identical to the setup in Section 5.1.1, with the addition of the outer carton. The geometric simplifications in Section 5.1.1 (i.e. omission of the glue lap and the overlapping flaps and the simplification of the fold lines) were applied to both components of the telescopic carton. Quarter-symmetry conditions were imposed using the symmetry surfaces in Marc. The top and bottom platens were modelled as rigid surfaces, with the bottom platen stationary and the top platen load- or displacement-controlled to compress the carton. The model setup is illustrated in Figure 5.13. A contact table was used to specify the following contact interactions:

- Touching contact between the inner carton and the outer carton

- Touching contact with friction between the inner carton and the bottom platen and between the outer carton and the top platen
- Touching contact between the outer carton (bottom edges) and the bottom platen
- Symmetry conditions where the inner- and outer carton are in contact with the XY symmetry surface
- Symmetry conditions where the inner- and outer carton are in contact with the ZY symmetry surface

The composite laminate formulation was used to specify the material properties of the C-flute board of the inner (250KL/C-150SC/250KL) and the B-flute board of the outer (175KL/B-150SC/175KL), with the homogeneous core properties in Table 3.4. The materials were orientated according to the local coordinate system of the elements, as in Section 5.1.1.

A mesh convergence study was performed to determine the mesh size for which the collapse load from an eigenvalue buckling analysis converges. The results in Figure 5.14 illustrate that the model is quite sensitive to changes in the mesh size, as observed for the solid-shell model in Section 5.1. The slope of the collapse load versus mesh size curve is, however, significantly smaller between the 1.5 mm mesh and the 3 mm mesh. For this reason, the 3 mm solid-shell mesh was used in the analyses.

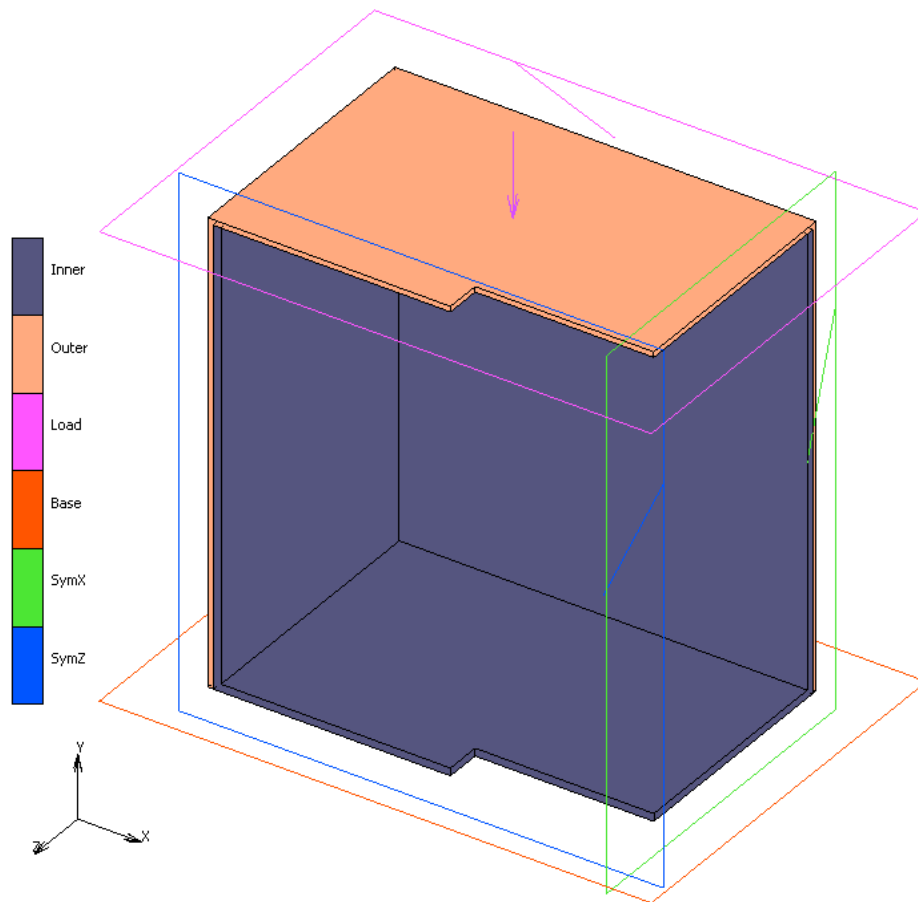


Figure 5.13: FE model of the Mk 4 telescopic carton with quarter-symmetry conditions

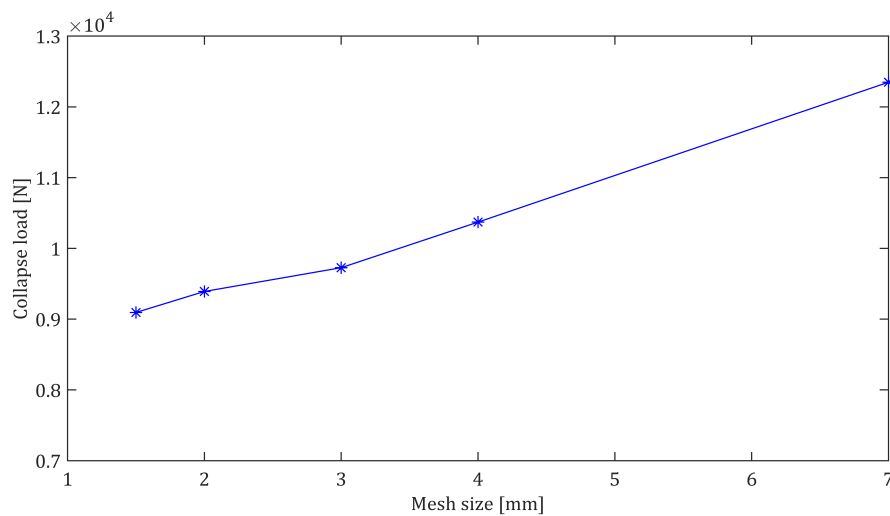


Figure 5.14: Mesh convergence study for the Mk 4 telescopic carton FE model

## 5.2.2 Analyses and results

Nonlinear static and buckling analyses were performed using the Large Strain formulation and the Updated Lagrange framework. The Full Newton-Raphson solution procedure and the default convergence criterion in Marc were used in the static load cases. In the first static load case, a compressive load of 7000 N (1750 N for the symmetry model) was applied to the carton using a multi-criteria adaptive stepping procedure. The buckling analysis followed, from which the collapse load and the buckling mode shape were extracted. The predicted collapse load is 9345 N, which is 3% larger than the measured BCT value of 9034 N. The buckling mode shape is illustrated in Figure 5.15 for both components (outer and inner) of the telescopic carton. The largest out-of-plane displacements are predicted at the centre of the longer vertical panel, which agrees with experimental observations and the DIC results in Section 4.4. The solid-shell telescopic model did not overestimate the collapse load as in the case of the solid-shell inner in Section 5.1. The load is applied to the top (horizontal) panel of the outer carton in the telescopic model, instead of perpendicular to the solid-shell edges (as in the model of the inner).

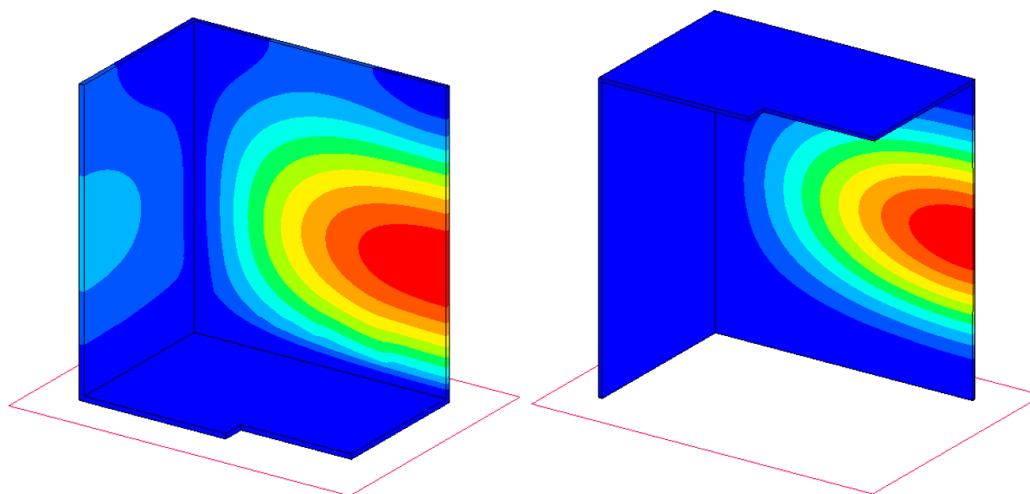


Figure 5.15: First buckling mode shape of the Mk 4 telescopic carton FE model

A second static load case with displacement-control of the top-platen was performed to simulate a BCT. The simulated load-displacement response is given in Figure 5.16. The load-displacement response suggests limit-point buckling, as in the solid-shell model of the Mk 4 inner. The peak load on the load-displacement curve is 16 464 N, which is significantly larger than the predicted collapse load of 9345 N. The same explanation for the overestimated collapse load as in Section 5.1 is plausible: the curvature of the vertical panels increases with the applied load, which, in turn, increases the overall panel stiffness. The peak load

occurs at a crosshead displacement smaller than 1 mm, as opposed to the experimental vertical displacement of 12.7 mm at the peak load. A possible explanation is that the inner and outer cartons were modelled as geometrically perfect and fully in contact at the start of the analysis. Physical samples are not geometrically perfect, and small gaps exist between the inner- and outer cartons.

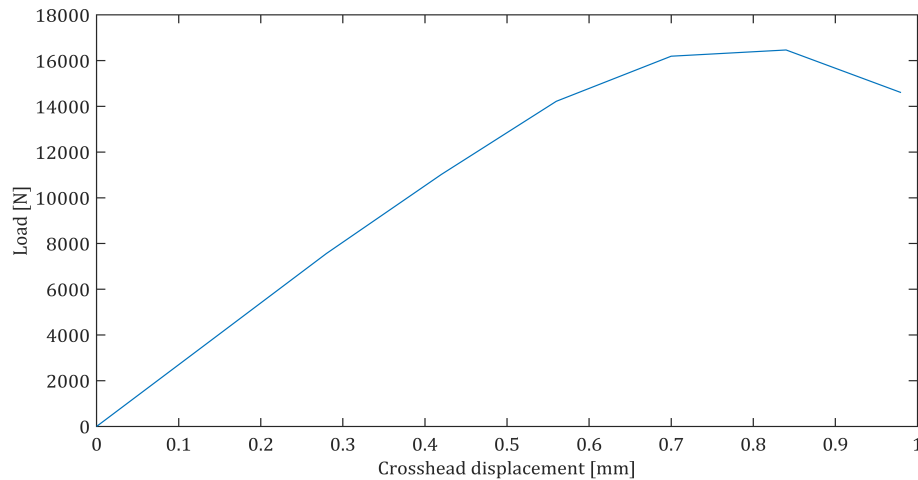


Figure 5.16: Mk 4 telescopic FE model load-displacement response

The X- and Z-displacement plots at the collapse load of the inner- and outer cartons are given in Figure 5.17 and Figure 5.18, respectively. The side panel buckles inward with a maximum displacement of 6.7 mm at the panel centre. The longer vertical panel buckled outward with 9.8 mm. The out-of-plane displacement response agrees with the predicted buckling mode shape in that the largest out-of-plane displacement occurs near the centre of the front/back panels. The experimental out-of-plane displacement of the front panel, measured using DIC, is 15–16 mm. The geometrically perfect FE model's prediction is 35% smaller.

The propagation of the region with the highest Tsai-Wu failure index (bright red on the colour map) is illustrated in Figure 5.19. The highest failure index originates near the centre of the longer vertical panel and propagates towards the edge where the vertical panels connect. Material failure occurs in the final image. The shear strain distributions of the inner- and outer cartons (at the increments that correspond to the first and last images in Figure 5.19) are given in Figure 5.20. The highest shear strain regions originate near the corners of the vertical panels. As the load increases, the highest shear strain regions move towards the edge where the two vertical panels connect, where material failure occurred in Figure 5.19.

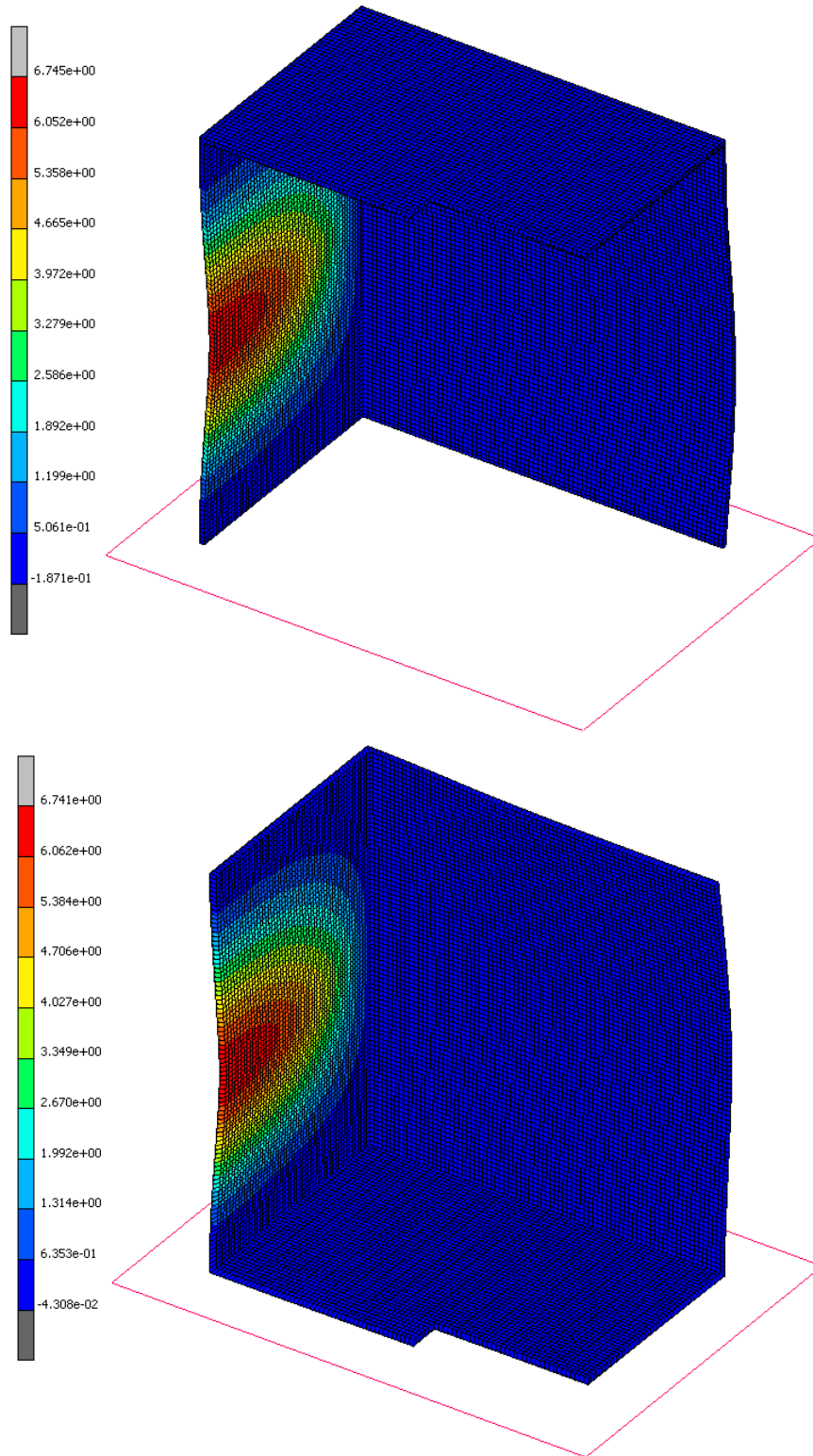


Figure 5.17: X-displacement plots of the telescopic FE model components (outer and inner) at the collapse load of a simulated BCT

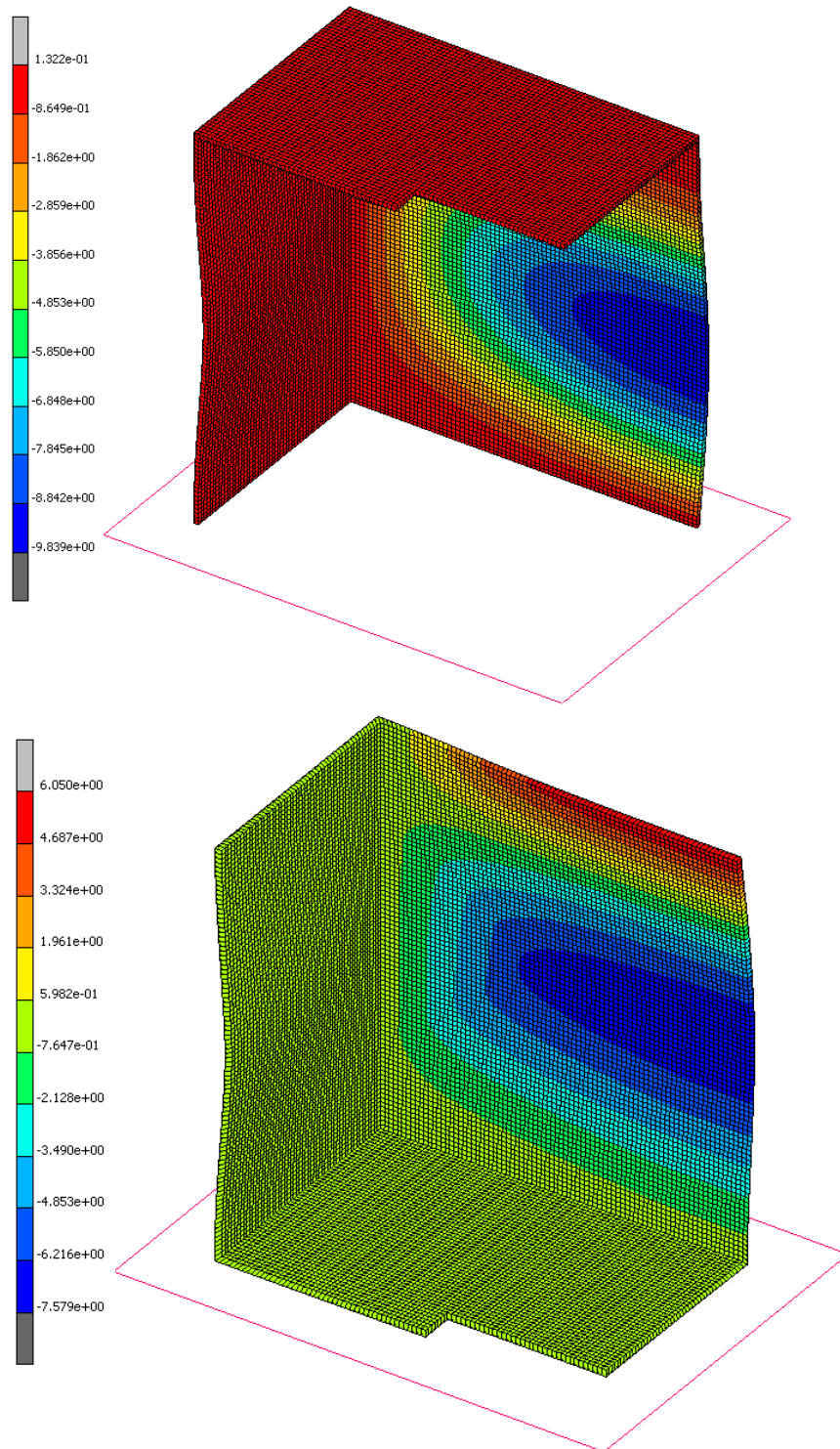


Figure 5.18: Z-displacement plots of the telescopic FE model components (outer and inner) at the collapse load of a simulated BCT



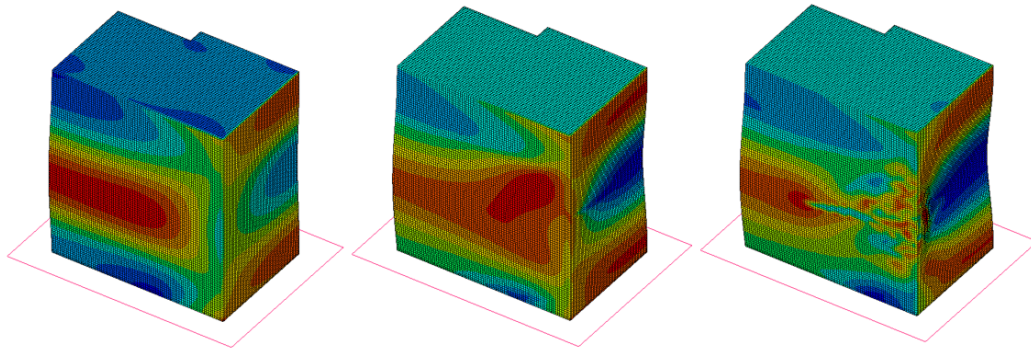


Figure 5.19: Tsai-Wu failure index propagation (left to right) of the outer liner (Mk 4 telescopic model, outer carton) during the simulated BCT

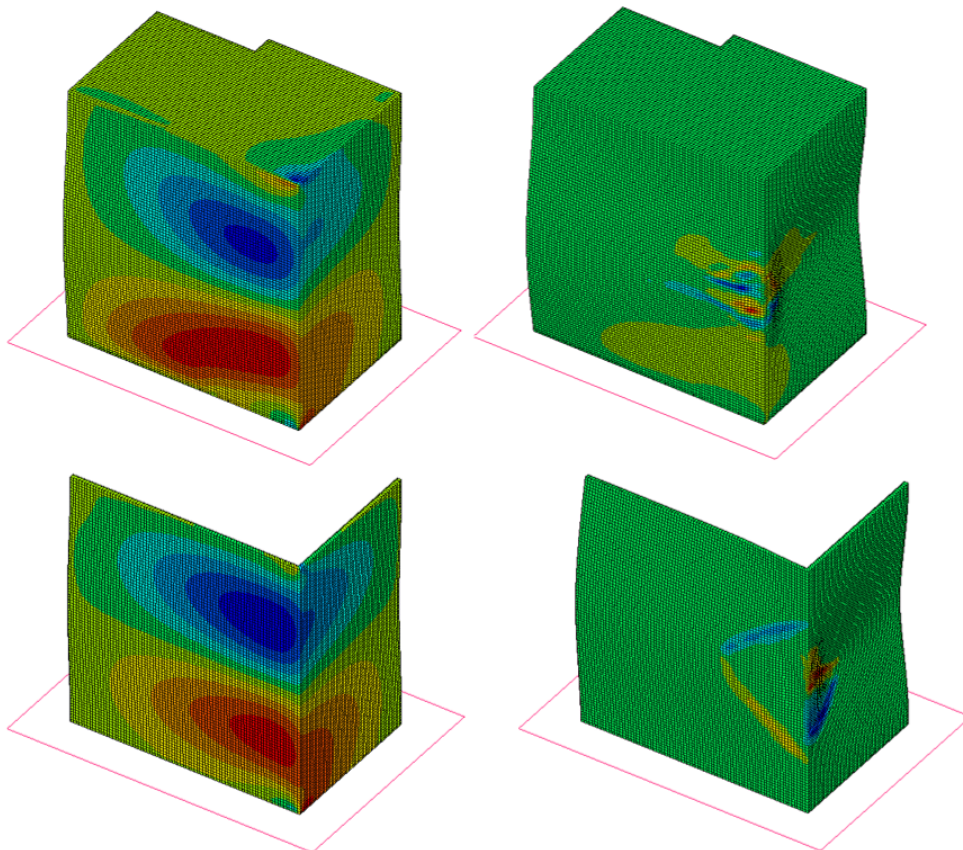


Figure 5.20: Evolution of the highest shear strain regions (left to right) during the simulated BCT of the Mk 4 telescopic model

The contact response of the Mk 4 carton during the simulated BCT is illustrated in Figures 5.21 and 5.22. In Figure 5.21, the centre region of the inner's base lifts from the bottom platen, while the edge nodes remain in contact with

the platen throughout the BCT. Most of the compressive load is, therefore, carried by the vertical panels. This response correlates closely to the pressure mapping results in Section 4.3. At the start of the BCT, the vertical panels were in perfect contact. As the telescopic carton is compressed and deforms into a buckled shape, separation occurs between the vertical panels of the inner and the outer (see Figure 5.22). The top edge of the inner's (longer) vertical panel loses contact with the outer, which suggests that the load is no longer applied parallel to the inner's top edges. As a result, the edges may be subject to a type of eccentric loading, which could also explain why the solid-shell model of the telescopic carton does not overestimate the collapse load to the same extent as the solid-shell model of the inner carton. Nordstrand (1995) investigated the effect of eccentric loading on a corrugated paperboard panel and reported a 15% reduction in the load-carrying capacity of the panel for an eccentricity of one-quarter of the panel thickness.

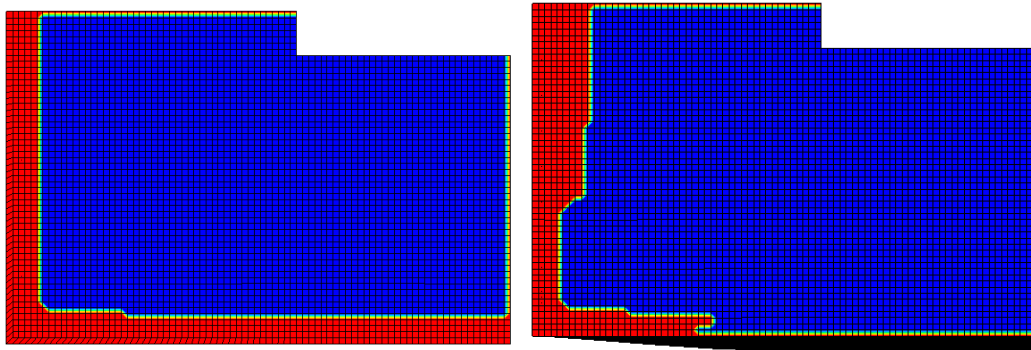


Figure 5.21: Touching contact (red on the colour map) between the base of the carton and the bottom platen just after the start of the BCT simulation (left) and at the collapse load (right)

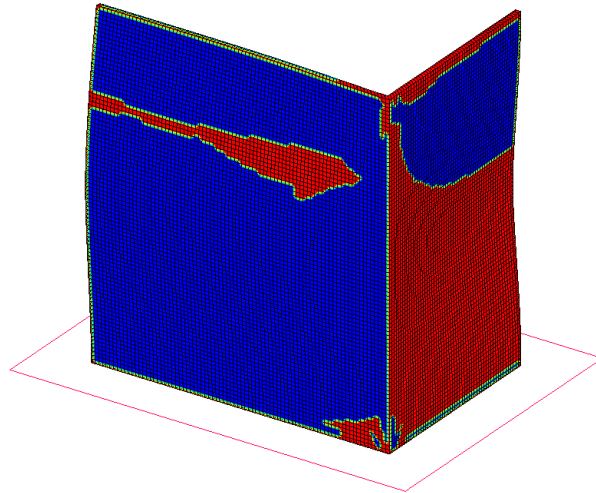


Figure 5.22: Touching contact (red on the colour map) between the inner and outer of the Mk 4 telescopic carton at the collapse load of the BCT simulation

The effect of two boundary condition cases on the collapse load of the telescopic carton was investigated:

- Case 1: Glued contact is specified for the contact interaction between the inner- and outer cartons instead of touching contact.
- Case 2: The bottom of the inner carton is glued to the bottom rigid surface instead of touching contact with friction.

The results are summarized in Table 5.2 and compared to the collapse load of the telescopic carton for the standard boundary conditions in Section 5.2.1. In the first boundary condition case, the collapse load increased by 189%, while the boundary condition experiment showed a 7% increase in the collapse load when the inner and outer cartons were glued together (Figure 4.6). The glued contact in the FE model is perfect, and separation is not allowed. The glued contact of the physical samples, however, was imperfect and some separation occurred during the BCT, which could explain the discrepancies between the numerical and experimental results. In the second case, the collapse load decreased by an insignificant amount (0.4%), where the boundary condition experiment showed a 16% decrease in the collapse load (Figure 4.7).

Table 5.2: Collapse load of the Mk 4 telescopic FE model for two boundary condition cases

Collapse load (N)	
Standard	9 345
Case 1	26 992
Case 2	9 303

### 5.3 Summary

In this section, the development of an FE model of the Mk 4 telescopic carton was discussed. The model's buckling response and the response from a simulated BCT were compared to experimental results. The model predicted a collapse load within 3% of the measured BCT value and its buckled shape correlated well with experimental observations. The model predicted the location of the maximum out-of-plane displacement with good accuracy but predicted a 35% smaller magnitude than what was measured using DIC.

The model overestimated the peak load from the simulated load-displacement response and underestimated the vertical displacement at the peak load to a large extent. The model's load-displacement response suggests that with the increasing curvature of the vertical panels (as the load increases), the overall panel stiffness is overestimated.

The highest failure index regions were related to the highest shear strain regions, at the vertical edges of the carton. The model predicted material failure at the edge where the vertical panels connect, which correlates with the location where crease lines formed during BCT experiments. The model's contact response was discussed, and correlations were made to the pressure mapping experiments in Section 4.3.

## Chapter 6

# Concluding remarks and recommendations

The finite element method (FEM) was used for further investigation into the non-linear structural modelling of corrugated paperboard packaging for fresh produce. A simplified material model of the corrugated sandwich structure, in which the corrugated core is reduced to an equivalent homogeneous core, was first developed. The material properties of the corrugated board constituents were experimentally obtained using industry-standard test methods, and digital image correlation was used to determine the in-plane Poisson's ratio of the paper. A challenge in the DIC analysis was that the paper specimens curled inward at the start of the test and flattened out as the tensile stress increased. The DIC strain calculation was adversely affected by the flattening of the specimens because it gives the impression that the specimens expand in the axial- and transverse directions. An explanation for the curling effect is that the paint that was used to apply the DIC speckle pattern shrinks when it dries. An alternative method for the speckle pattern application on thin and moisture-sensitive paper specimens should be investigated or a stereo (3D) camera set up should be used in the future.

The measured material properties of the paperboard constituents were used to model an edge compression test specimen, and the model was validated using experimental ECT results. An analytical homogenisation approach based on classical laminated plate theory was used to determine the equivalent elastic properties of the homogeneous core. A simplified material model was developed using the homogeneous core, and its response was compared to that of a detailed FE model of a corrugated paperboard sandwich panel. The collapse load and buckling mode shape of the simplified model and the detailed model showed good agreement, with a 3.5% difference between the predicted collapse loads when 4-node thick-shell elements were used in the simplified model, and a 2.2% difference between the predicted collapse loads when 8-node solid-shell elements were used. The effect of an initial geometric imperfection was also investigated. A small geometric imperfection was found to improve the out-of-plane

displacement response of the simplified model without affecting its collapse load prediction.

The second part of the study involved characterising the mechanical response of the Mk 4 telescopic carton during box compression tests. The out-of-plane displacement response was captured using 3D DIC, which showed that the maximum out-of-plane displacement occurs at the centre of the front/back vertical panels of the carton. The pressure distribution between the carton and the base of the compression tester was measured using a Tekscan pressure mapping sensor. The results showed that the applied load is concentrated around the edges of the carton, which suggests that the vertical panels carry most of the compressive load.

The final part of the project was the development of a structural FE model of the Mk 4 telescopic carton, and the validation thereof using the BCT experimental results. Solid-shell (brick) elements were considered for the telescopic model for their accuracy and efficiency when modelling double-sided contact. The Mk 4's inner carton was first modelled using two different element types: 4-node thick-shell elements and 8-node solid-shell elements. The thick-shell model predicted the collapse load and the maximum out-of-plane displacement within 3% and 18% of the measured values, while the solid-shell model largely overestimated the collapse load and underestimated the magnitude of the out-of-plane displacements. The Mk 4 telescopic carton was modelled using solid-shell elements and the contact between the inner- and the outer carton was considered in the analysis. The telescopic model did not overestimate the collapse load as in the case of the solid-shell model of the inner. The predicted collapse load is within 3% of the measured BCT value, and the maximum out-of-plane displacement is 35% smaller than the measured value. The discrepancy between the collapse load predictions of the solid-shell models could be related to an eccentric load on the edges of the telescopic model's inner carton that occurs when the edges buckle inward. The finite element models in this thesis show good correlations to experimental results and demonstrate the potential of nonlinear FEM to model the BCT response of telescopic cartons. The final FE model of the Mk 4 carton can be used as a design tool if the objective is to design based on compression strength and material requirement.

# **Appendices**

## Appendix A

# MATLAB script: Corrugated core homogenisation

```
% Measured and known properties
E1 = 4.709e9;    % Young's modulus MD [Pa]
E2 = 2.918e9;    % Young's modulus CD [Pa]
t = 251e-6;     % Paper thickness [m]
f = 3.61e-3;    % Flute height [m]
P = 7.7e-3;     % Flute wavelength [m]
h = f + t;      % Core height [m]

% Calculated properties
G12 = 0.387*sqrt(E1*E2);    % (Baum, 1981)
nu12 = 0.293*sqrt(E1/E2);

E3 = E1/190;                % (Mann et al., 1979)
G13 = E1/55;                % (Baum et al., 1981)
G23 = E2/35;                % (Baum et al., 1981)
nu13 = 0.001;               % (Nordstrand, 1995)
nu23 = 0.001;

% Flute geometry
syms x
a = 2*pi/P;
b = pi*f/P;
H = (f/2)*sin(a*x);        % Flute profile
theta = atan(b*cos(a*x));  % Rotation angle at x
```



```

% Material compliance matrix
C123 = [1/E1    -nu12/E1  -nu13/E1    0    0    0;
        -nu12/E1  1/E2    -nu23/E2    0    0    0;
        -nu13/E1  -nu23/E2    1/E3    0    0    0;
         0         0         0    1/G12  0    0;
         0         0         0     0  1/G13  0;
         0         0         0     0    0  1/G23];

% Transformation matrices for rotation about y-axis
c = cos(theta);
s = sin(theta);

Te = [c^2    0    s^2    0    -s*c    0;      % Strain transformation
      0     1     0     0     0     0;
      s^2    0    c^2    0     s*c    0;
      0     0     0     c     0    -s;
      2*s*c  0   -2*s*c  0  (c^2-s^2)  0;
      0     0     0    -s     0     c];

Ts = [c^2    0    s^2    0    2*s*c    0;      % Stress transformation
      0     1     0     0     0     0;
      s^2    0    c^2    0   -2*s*c    0;
      0     0     0     c     0    -s;
      -s*c  0     s*c    0  (c^2-s^2)  0;
      0     0     0    -s     0     c];

% Rotated compliance matrix
Cxyz = simplify(Te*C123*Ts);

% Reduced rotated stiffness matrices
Q = inv(Cxyz([1:2,4],[1:2,4]));
G = inv(Cxyz(5:6,5:6));

% Vertical thickness of fluting (Talbi et al., 2009)
tv = t/cos(theta);
% From D(x) = integral(Q(x)*z^2)dz
z = H;
d = (H^2)*tv + (tv^3)/12;

% Homogenization through the thickness (z-direction)
A11 = matlabFunction(tv*Q(1,1)); D11 = matlabFunction(d*Q(1,1));
A12 = matlabFunction(tv*Q(1,2)); D12 = matlabFunction(d*Q(1,2));
A21 = matlabFunction(tv*Q(2,1)); D21 = matlabFunction(d*Q(2,1));
A22 = matlabFunction(tv*Q(2,2)); D22 = matlabFunction(d*Q(2,2));
A33 = matlabFunction(tv*Q(3,3)); D33 = matlabFunction(d*Q(3,3));
F11 = matlabFunction(tv*G(1,1)); F22 = matlabFunction(tv*G(2,2));

```

```

% Homogenization along the MD (x-direction)
A = zeros(3); D = zeros(3);
B = zeros(3); F = zeros(2);

A(1,1) = (1/P)*integral(A11, 0, P);
A(1,2) = (1/P)*integral(A12, 0, P);
A(2,1) = (1/P)*integral(A21, 0, P);
A(2,2) = (1/P)*integral(A22, 0, P);
A(3,3) = (1/P)*integral(A33, 0, P);

D(1,1) = (1/P)*integral(D11, 0, P);
D(1,2) = (1/P)*integral(D12, 0, P);
D(2,1) = (1/P)*integral(D21, 0, P);
D(2,2) = (1/P)*integral(D22, 0, P);
D(3,3) = (1/P)*integral(D33, 0, P);

F(1,1) = (1/P)*integral(F11, 0, P);
F(2,2) = (1/P)*integral(F22, 0, P);

% Partially inverted components of ABD (Gibson, 2012)
As = inv(A);
Bs = -A\B;
Ds = D - (B/A)*B;

% Fully inverted components of ABD (Gibson, 2012)
Ai = As - (Bs/D)*Bs;
Bi = Bs/Ds;
Di = inv(Ds);
Fi = inv(F);

% Effective thickness (Marek & Garbowski, 2015)
th = sqrt(12*(D(1,1)+D(2,2)+D(3,3))/(A(1,1)+A(2,2)+A(3,3)));

% Equivalent elastic constants
Ex = 1/(th*Ai(1,1));
Ey = 1/(th*Ai(2,2));
Gxy = 1/(th*Ai(3,3));
Gxz = 1/(th*Fi(1,1));
Gyz = 1/(th*Fi(2,2));
nuxy = -Ai(1,2)/Ai(1,1);

```

## Appendix B

# Experiments: Additional information and results

The results from the BCT boundary conditions experiment are given in Table B.1, and the box compression tester is illustrated in Figure B.1. Additional results from the 3D DIC are given in Figures B.2 and B.3, and the 2D DIC experimental setup is illustrated in Figure B.4.

Table B.1: BCT boundary condition experiment results

Description	Sample size	Peak load (N)	Displacement at peak load (mm)
Outer	5	$3964 \pm 138$	$6.2 \pm 0.4$
Inner	6	$4506 \pm 79$	$7.5 \pm 0.3$
Telescopic	10	$9034 \pm 257$	$12.7 \pm 0.6$
Glued assembly	3	$9386 \pm 534$	$17.2 \pm 0.0$
Telescopic, case (1)	3	$8485 \pm 543$	$14.7 \pm 0.2$
Telescopic, case (2)	3	$8150 \pm 296$	$16.3 \pm 1.2$
Telescopic, case (3)	3	$8332 \pm 77$	$15.8 \pm 0.8$
Inner, case (1)	3	$4500 \pm 164$	$6.9 \pm 0.2$
Inner, case (2)	4	$5388 \pm 89$	$6.4 \pm 0.4$

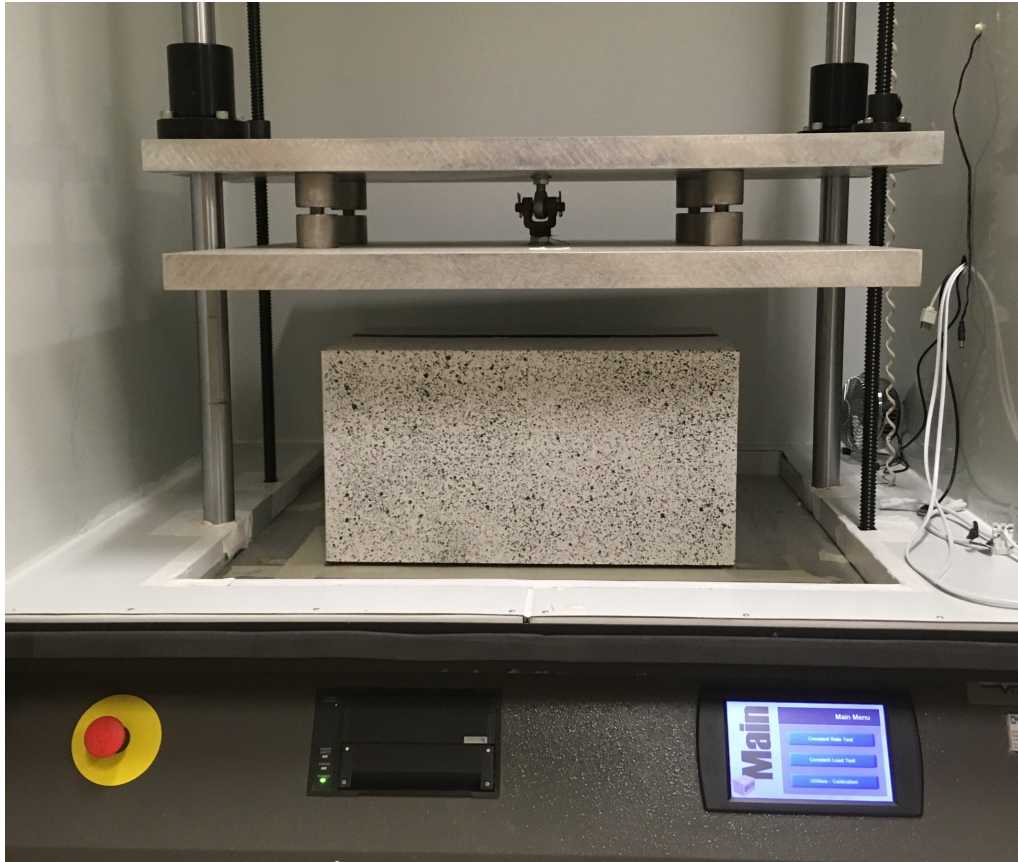


Figure B.1: BCT setup

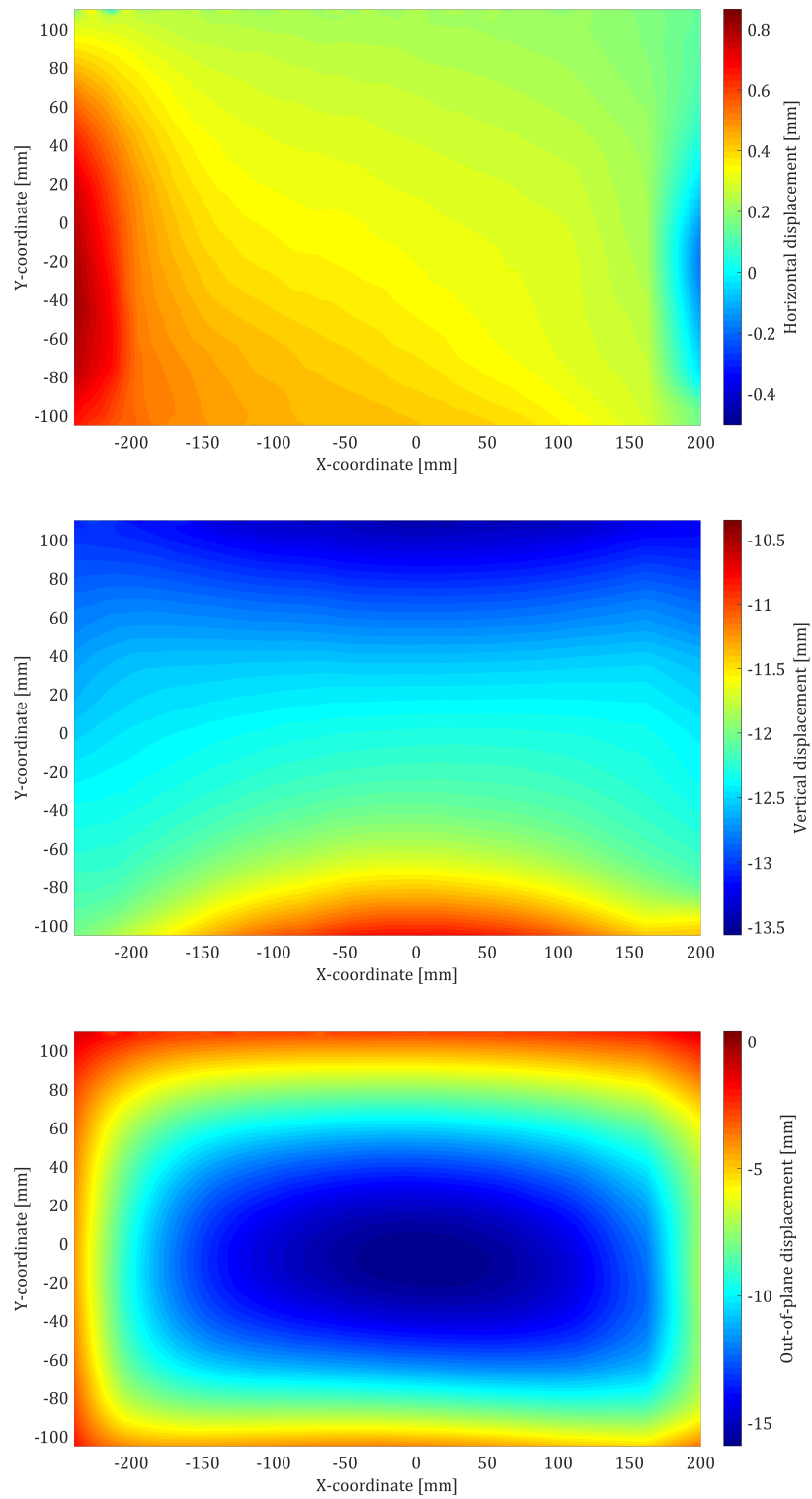


Figure B.2: DIC X, Y and Z (top to bottom) displacement fields of the Mk 4 telescopic carton

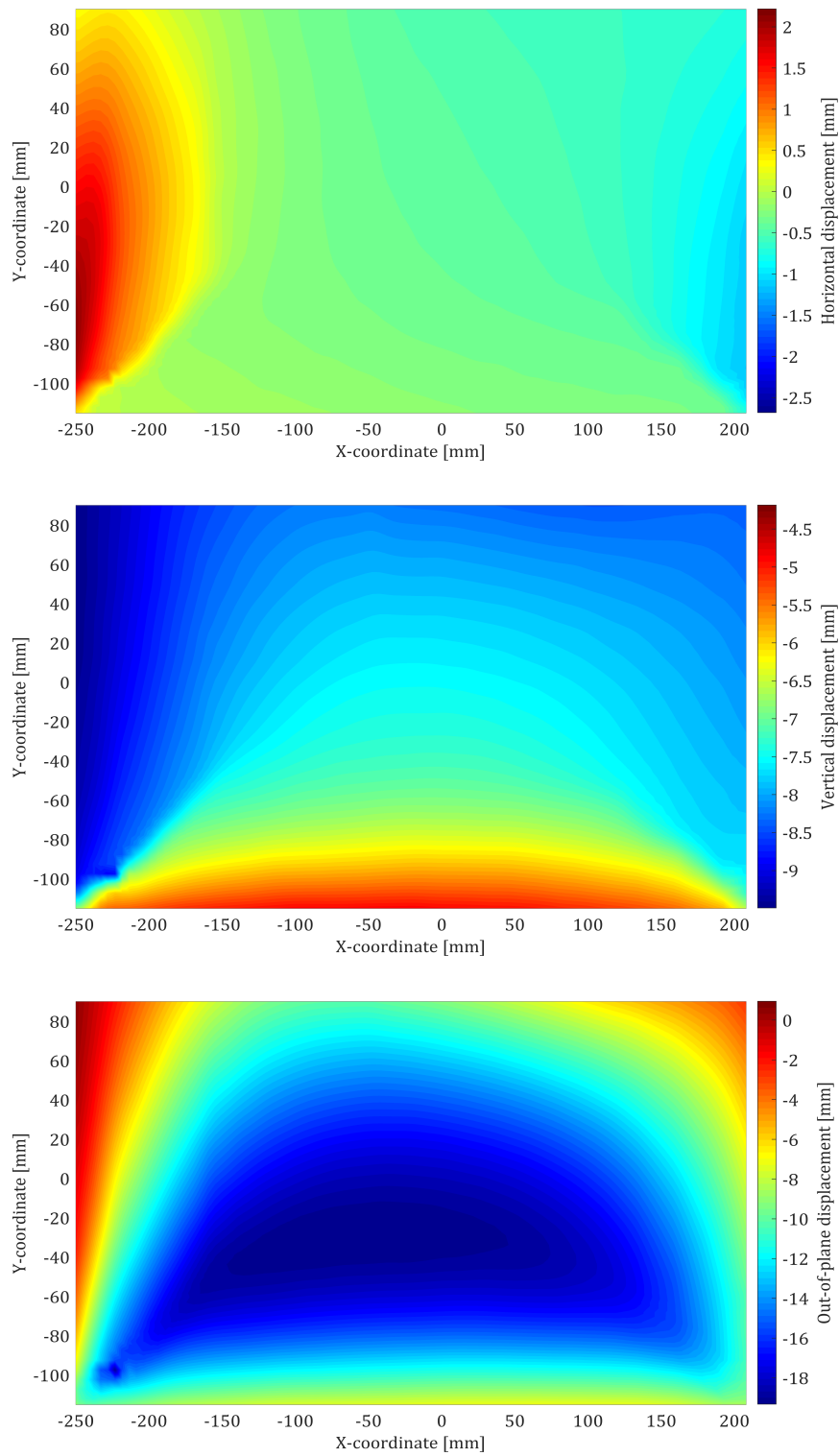


Figure B.3: DIC X, Y and Z (top to bottom) displacement fields of the Mk 4 inner



Figure B.4: Tensile test and DIC setup

## **Appendix C**

### **Mk 4 carton flat pattern**

The flat pattern of the Mk 4 outer carton is given in Figure C.1 as a reference for the dimensions of the FE models.



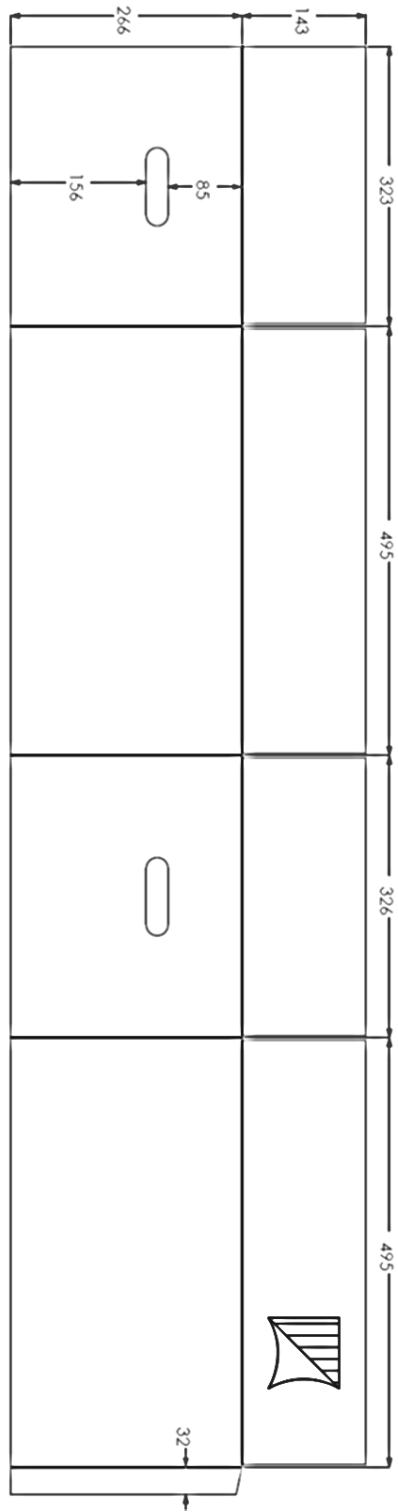


Figure C.1: Flat pattern of the Mk 4 outer carton

## References

- Allansson, A. and Svärd, B. (2001). *Stability and collapse of corrugated board: Numerical and experimental analysis*. Master's Thesis, Lund University.
- Alves de Sousa, R.J., Yoon, J.W., Cardoso, R.P., Fontes Valente, R.A. and Grácio, J.J. (2007). On the use of a reduced enhanced solid-shell (RESS) element for sheet forming simulations. *International Journal of Plasticity*, vol. 23, pp. 490–515. ISSN 07496419.
- Arvidsson, J. and Grönvall, J. (2004). *Analysis of creep in paperboard packages with plastic tops*. Master's thesis, Lund University.
- ASTM International (2009). D7030-04: Standard test method for short term creep performance of corrugated fiberboard containers under constant load using a compression test machine.
- ASTM International (2010). D642: Standard test method for determining compressive resistance of shipping containers, components, and unit loads.
- Baum, G.A. (1981). Procedures for measuring the in-plane orthotropic elastic constants of paper using ultrasonic techniques. *IPC Technical Paper Series*, , no. 119.
- Baum, G.A., Brennan, D.C. and Habeger, C.C. (1981). Orthotropic elastic constants of paper. *Tappi Journal*, vol. 64, pp. 97–101.
- Beldie, L., Sandberg, G. and Sandberg, L. (2001). Paperboard packages exposed to static loads-finite element modelling and experiments. *Packaging Technology and Science*, vol. 14, pp. 171–178. ISSN 08943214.
- Berry, T.M. (2017). *Optimisation of multi-scale ventilated package design for next-generation cold chain strategies of horticultural produce*. Doctoral Dissertation, Stellenbosch University.
- Berry, T.M., Fadiji, T.S., Defraeye, T. and Opara, U.L. (2017). The role of horticultural carton vent hole design on cooling efficiency and compression strength: A multi-parameter approach. *Postharvest Biology and Technology*, vol. 124, pp. 62–74. ISSN 09255214.
- Biancolini, M.E. (2005). Evaluation of equivalent stiffness properties of corrugated board. *Composite Structures*, vol. 69, pp. 322–328. ISSN 02638223.

- Biancolini, M.E. and Brutti, C. (2003). Numerical and experimental investigation of the strength of corrugated board packages. *Packaging Technology and Science*, vol. 16, pp. 47–60. ISSN 08943214.
- Biancolini, M.E., Brutti, C., Mottola, E. and Porziani, S. (2005). Numerical evaluation of buckling and post-buckling behaviour of corrugated board containers. In: *Proceedings of the 34th AIAS Congress*.
- Biancolini, M.E., Brutti, C. and Porziani, S. (2010). Corrugated board containers design methods. *Int. J. Computational Materials Science and Surface Engineering*, vol. 3, no. 2, pp. 143–163. ISSN 1753-3465.
- Biermann, C.J. (1996). *Handbook of pulping and papermaking*. 2nd edn. Elsevier. ISBN 978-0-08-053368-1.
- Briassoulis, D. (1986). Equivalent orthotropic properties of corrugated sheets. *Computers and Structures*, vol. 23, no. 2, pp. 129–138. ISSN 00457949.
- British Standard (2008a). ISO 1924-2: Paper and board, determination of tensile properties.
- British Standard (2008b). ISO 9895: Paper and board, compressive strength (short-span test).
- Callister, W.D.J. and Rethwisch, D.G. (2015). *Materials Science and Engineering*. 9th edn. John Wiley & Sons, Hoboken, NJ.
- Cao, X., Bi, Z., Wei, X. and Xie, Y. (2012). Determination of Poisson's ratio of Kraft paper using digital image correlation. *Mechanical Engineering and Technology*, vol. 125.
- Carlsson, L.A., Nordstrand, T. and Westerlind, B. (2001). On the elastic stiffnesses of corrugated core sandwich. *Journal of Sandwich Structures & Materials*, vol. 3, no. 4, pp. 253–267. ISSN 10996362.
- Cook, R., Malkus, D., Plesha, M. and Witt, R. (2002). *Concepts and Applications of Finite Element Analysis*. 4th edn. John Wiley & Sons, Inc., Hoboken, NJ.
- Cox, H.L. (1952). The elasticity and strength of paper and other fibrous materials. *British Journal of Applied Physics*, vol. 3, pp. 72–79. ISSN 05083443.
- Ellis, D.R. (2017). *Mechanical characterisation for simplified response modelling of woven polypropylene*. Master's Thesis, Stellenbosch University.
- Emblem, A. and Emblem, H. (2012). *Packaging technology: Fundamentals, materials and processes*. ISBN 9781845696658.
- Fadiji, T., Berry, T.M., Coetzee, C.J. and Opara, U.L. (2018a). Mechanical design and performance testing of corrugated paperboard packaging for the postharvest handling of horticultural produce. *Biosystems Engineering*, vol. 171, pp. 220–244. ISSN 15375110.

- Fadiji, T., Coetzee, C. and Opara, U.L. (2016). Compression strength of ventilated corrugated paperboard packages: Numerical modelling, experimental validation and effects of vent geometric design. *Biosystems Engineering*, vol. 151, pp. 231–247. ISSN 15375110.
- Fadiji, T., Coetzee, C.J., Berry, T.M., Ambaw, A. and Opara, U.L. (2018b). The efficacy of finite element analysis (FEA) as a design tool for food packaging: A review. *Biosystems Engineering*, vol. 174, pp. 20–40. ISSN 15375110.
- Fadiji, T.S. (2015). *Mechanical design and performance evaluation of ventilated packages*. Master's Thesis, Stellenbosch University.
- Fadiji, T.S. (2019). *Numerical and experimental performance evaluation of ventilated packages*. Doctoral Dissertation, Stellenbosch University.
- FAO (2019). The State of Food and Agriculture 2019: Moving forward on food loss and waste reduction. Tech. Rep., Rome.
- Gibson, R.F. (2007). *Principles of Composite Material Mechanics*. 2nd edn. CRC Press, Boca Raton, FL. ISBN 0824753895.
- Gilchrist, A.C., Suhling, J.C. and Urbanik, T.J. (1999). Nonlinear finite element modeling of corrugated board. *Mechanics of Cellulosic Materials*, pp. 101–106. ISSN 01608835.
- Haslach, H.W.J. (1994). The mechanics of moisture accelerated tensile creep in paper. *Tappi Journal*, vol. 77, no. 10, pp. 179–186. ISSN 07341415.
- Jones, A.R. (1967). *An experimental investigation of the in-plane elastic moduli of paper*. Ph.D. thesis, Lawrence University.
- Jones, R.M. (1999). *Mechanics of Composite Materials*. 2nd edn. Taylor & Francis, Philadelphia. ISBN 156032712X.
- Kim, N.-H. (2015). *An Introduction to Nonlinear Finite Element Analysis*. Springer Science+Business Media, New York. ISBN 978-1-4419-1746-1.
- Kueh, C., Navaranjan, N. and Duke, M. (2012). The effect of in-plane boundary conditions on the post-buckling behaviour of rectangular corrugated paperboard panels. *Computers and Structures*, vol. 104-105, pp. 55–62. ISSN 00457949.
- Kueh, C.S.L., Dahm, K., Emms, G., Wade, K. and Bronlund, J.E. (2019). Digital image correlation analysis of vertical strain for corrugated fiberboard box panel in compression. *Packaging Technology and Science*, pp. 1–9.
- Malo, B.A. (1967). Semicemical hardwood pulping and effluent treatment. *J. Water Pollut. Control Fed.*, vol. 39, no. 11, pp. 1875–1891.
- Mann, R.W., Baum, G.A. and Habeger, C.C. (1979). Determination of all nine orthotropic elastic constants for machine-made paper. *Tappi*, vol. 63, no. 2, pp. 163–166.
- Marek, A. and Garbowski, T. (2015). Homogenization of sandwich panels. *Computer Assisted Methods in Engineering and Science*, vol. 22, pp. 39–50. ISSN 22993649.

- McKee, R., Gander, J. and Wachuta, J. (1963). Compression strength formula for corrugated boxes.
- Meng, G., Trost, T. and Östlund, S. (2007). Stacking misalignment of corrugated boxes - a preliminary study. *Proceedings of the 23rd IAPRI Symposium on Packaging*, pp. 1–18.
- Miller, T.C. (2013). Poisson's ratio extrapolation from digital image correlation experiments. Tech. Rep., Air Force Research Laboratory, California.
- MSC Software Corporation (2019). Marc/Mentat.
- Nordstrand, T. (2003). *Basic testing and strength design of corrugated board and containers*. Doctoral Dissertation, Lund University.
- Nordstrand, T. (2004). Analysis and testing of corrugated board panels into the post-buckling regime. *Composite Structures*, vol. 63, no. 2, pp. 189–199. ISSN 02638223.
- Nordstrand, T.M. (1995). Parametric study of the post-buckling strength of structural core sandwich panels. *Composite Structures*, vol. 30, no. 4, pp. 441–451. ISSN 02638223.
- Oelofse, S.H. and Nahman, A. (2013). Estimating the magnitude of food waste generated in South Africa. *Waste Management and Research*, vol. 31, no. 1, pp. 80–86. ISSN 0734242X.
- Opara, U.L. and Mditshwa, A. (2013). A review on the role of packaging in securing food system: Adding value to food products and reducing losses and waste. *African Journal of Agricultural Research*, vol. 8, no. 22, pp. 2621–2630.
- Opara, U.L. and Pathare, P.B. (2014 may). Bruise damage measurement and analysis of fresh horticultural produce—A review. *Postharvest Biology and Technology*, vol. 91, pp. 9–24. ISSN 0925-5214.
- Pathare, P.B. and Opara, U.L. (2014 sep). Structural design of corrugated boxes for horticultural produce: A review. *Biosystems Engineering*, vol. 125, pp. 128–140. ISSN 1537-5110.
- Phongphinitana, E. and Jearanaisilawong, P. (2012). A microstructurally-based orthotropic elasto-plastic model for paper and paperboard. *AIJSTPME*, vol. 5, no. 1, pp. 19–25.
- Popil, R.E., Coffin, D.W. and Kaewmanee, P. (2004). The role of buckling in the edge compression test of corrugated board. In: *Progress in Paper Physics*.
- PPECB (2018). Annual Report 2017/2018. Tech. Rep., South Africa.
- PPECB (2019). Annual Report 2018/2019.
- Pritchard, R.H., Lava, P., Debruyne, D. and Terentjev, E.M. (2013). Precise determination of the Poisson ratio in soft materials with 2D digital image correlation. *Soft Matter*, vol. 9, no. 26, pp. 6037–6045. ISSN 1744683X.

- Schulgasser, K. (1981). On the in-plane elastic constants of paper. *Fibre Science and Technology*, vol. 15, no. 4, pp. 257–270. ISSN 00150568.
- Schulgasser, K. (1983). The in-plane Poisson ratio of paper. *Fibre Science and Technology*, vol. 19, no. 4, pp. 297–309. ISSN 00150568.
- Sorvari, J. (2009). *Modelling methods for viscoelastic constitutive modelling of paper*. Doctoral dissertation, University of Kuopio.
- Sun, B.H., Yeh, K.Y. and Rimrott, F.P.J. (1995). On the buckling of structures. *Technische Mechanik*, vol. 15, no. 2, pp. 129–140.
- Sutton, M.A., Orteu, J.-J. and Schreier, H.W. (2010). *Image Correlation for Shape, Motion and Deformation Measurements: Basic Concepts, Theory and Applications*. Springer, New York. ISBN 9780387787466.
- Talbi, N., Batti, A., Ayad, R. and Guo, Y.Q. (2009). An analytical homogenization model for finite element modelling of corrugated cardboard. *Composite Structures*, vol. 88, no. 2, pp. 280–289. ISSN 02638223.
- TAPPI (2012). T804: Compression test of fiberboard shipping containers.
- Tekscan Inc. (2009). I-Scan & High Speed I-Scan User Manual. Tech. Rep. 6, Tekscan, Inc., South Boston, MA.
- Twede, D. and Selke, S.E.M. (2005). *Cartons, Crates and Corrugated Board: Handbook of Paper and Wood Packaging Technology*. DEStech Publications, Lancaster, PA. ISBN 1932078428.
- Urbanik, T.J. (1997). Linear and nonlinear material effects on postbuckling strength of corrugated containers. *Mechanics of Cellulosic Materials*, vol. 221, pp. 93–99.
- WWF (2017). Food Loss and Waste: Facts and Futures. *WWF South Africa*.
- Zhang, Y.L., Chen, J., Wu, Y. and Sun, J. (2011). Analysis on hazard factors of the use of corrugated carton in packaging low-temperature yogurt during logistics. *Procedia Environmental Sciences*, vol. 10, pp. 968–973. ISSN 18780296.